INTERFACE FRACTURE IN MASONRY COMPOSITES: A LATTICE APPROACH

A Dissertation

Presented to

the Faculty of the Department of Civil and Environmental Engineering

University of Houston

In Partial Fulfillment

of the Requirements for the Degree

Doctor of Philosophy

in Civil Engineering

by

Amir H. Mohammadipour

August 2015

INTERFACE FRACTURE IN MASONRY COMPOSITES: A LATTICE APPROACH

Amir H. Mohammadipour

Approved:

Chair of the Committee
Kaspar J. Willam, Professor,
Civil and Environmental Engineering

Committee Members:

Mina Dawood, Associate Professor,
Civil and Environmental Engineering

Kalyana Nakshatrala, Assistant Professor,
Civil and Environmental Engineering

Kenneth White, Professor,
Mechanical Engineering

Ashraf Ayoub, Professor,
Civil Engineering,
City University London

Suresh K. Khator, Associate Dean,
Cullen College of Engineering

Roberto Ballarini, Professor and Chair,
Civil and Environmental Engineering

ACKNOWLEDGEMENTS

I would like to express my deepest gratitude to my advisor, Professor Kaspar Willam, for his excellent guidance, understanding, patience, and very kind attitude in providing a friendly atmosphere in accomplishing this dissertation. His wisdom, expert knowledge, and paramount mentorship as well as the stimulating ideas and discussions with him have contributed to a great extent in the completion of this dissertation. Prof. Ashraf Ayoub, Prof. Kenneth White, Dr. Kalyana Nakshatrala, and Dr. Mina Dawood, as members of my dissertation committee, are greatly acknowledged for their generous time and valuable comments. I would like to gratefully thank Prof. Roberto Ballarini, the chair of the Civil and Environmental Engineering Department, for his interest and care. I am also grateful to all my friends and colleagues during my study at the University of Houston. Moreover, the support of this research effort by the U.S. National Science Foundation is sincerely appreciated.

Finally, and most importantly, I would like to gratefully thank the support and love of my family-my brother, Alireza; my sister, Neda; my father, Morad, who always believed in me; and especially my mother, Zari, who is my advisor in my life with her priceless love, support, inspiration, and wisdom.

INTERFACE FRACTURE IN MASONRY COMPOSITES: A LATTICE APPROACH

An Abstract

of a

A Dissertation

Presented to

the Faculty of the Department of Civil and Environmental Engineering

University of Houston

In Partial Fulfillment

of the Requirements for the Degree

Doctor of Philosophy

in Civil Engineering

by

Amir H. Mohammadipour

August 2015

ABSTRACT

The brick-mortar bond or interface is often the weakest link in the masonry composites. The localization of fracture processes at this bi-material interface plays an important role in the failure of this assemblage. These micro-level fracture processes control the nonlinear behavior of the brick-mortar interface which significantly affects the global behavior of the masonry structure at the continuum macro level. 2D Lattice-based micro-level fracture simulations which are based on Voronoi tessellation to discretize the continuum brick and mortar domains are applied to study progressive debonding of brick-mortar interfaces in unreinforced masonry composites. An energy method is subsequently employed to obtain the energy release rate of the lattice mesh as the crack propagates which is determined by considering the variation in the global stiffness matrix of the mesh with respect to crack length change. This energy release rate is inserted into the Irwin type fracture relationship for plane strain to calculate the modulus of complex stress intensity factor and its mode 1 and mode 2 values which are independent of the distance from the crack tip in the lattice. The lattice results for the energy release rate and stress intensity factors are then validated by comparing with three classic fracture mechanics problems analytical solutions of which are available in the literature. Afterwards, the 2-D plane strain lattice formulation is applied to simulate interfacial fracture properties of conventional test configurations in masonry. The computational lattice model is capable of evaluating the fracture toughness of brick-mortar interface along with other fracture properties from basic strength properties of lattice struts, which are removed by erosion upon failure. This information is employed to upscale the lattice fracture arguments onto the meso-level to quantify the fracture energy formulation of traction-separation cohesive zone models in the context of continuum finite element simulations of heterogeneous media such as masonry. The fracture energy from the lattice is also used in homogenizing a heterogeneous anisotropic masonry unit cell under direct tension using energy equivalence concept to obtain a scalar damage parameter which could be utilized to model the nonlinear behavior of a homogenized isotropic continuum finite element.

TABLE OF CONTENTS

LIST OF FIGURES

LIST OF TABLES

NOMENCLATURE

A	*Cross sectional area for a lattice element*
A_x, A_y	Cell size of the lattice mesh grid along x and y axes
a	Crack length
b	Width of the four-point bending beam
$\boldsymbol{B}$	Matrix relating the displacement vector in the lattice local $t-n$ coordinates to that in the global $x-y$ coordinates
$d(\boldsymbol{X_i}, \boldsymbol{X})$	Euclidean distance between $\boldsymbol{X_i}$ and $\mathbf{X}$
D_{INC}	Scalar isotropic damage parameter at increment INC
$\boldsymbol{D}$	Diagonal constitutive matrix in the lattice model
E_j	Young's modulus of material j
E', E''	Equivalent Young's muduli in the normal and tangential direction for a lattice element
$E_*, \bar{E}_j$	Equivalent Young's moduli for plane stress and plane strain
E_b, E_m	Young's moduli for brick and mortar
E_T	Total energy
$f_s = \tau_0$	Interface cohesion in pure shear
f_t, f_c	Tensile and compressive strengths of material
$\boldsymbol{f_e}$	Force vector in the lattice global $x-y$ coordinates for the frame element e
$\{f\}$	Vector of prescribed nodal loads in the lattice mesh
G_1, G_2	Energy release rate for mode 1 and mode 2

G	Energy release rate
h_0	Lattice element length
h_1, h_2	Thicknesses of the top and bottom layers in the four-point bending simulation
h_b, h_m	Thickness of brick and mortar
h	Total thickness of the specimen in the four-point bending simulation
I	Moment of inertia
i	The imaginary number, $i = \sqrt{-1}$
$\widehat{K}_1, \widehat{K}_2$	Rotated stress intensity factor for modes 1 and 2, respectively
$[K]_{a+\Delta a}$	Global stiffness matrix of the whole lattice mesh after a crack growth of Δa
$\lvert K \rvert$	Modulus of complex stress intensity factor
K_1, K_2	Stress intensity factor for modes 1 and 2, respectively
K_n, K_t	Homogenized stiffnesses per unit thickness of interface element in the normal and tangential directions in the lattice model
k_n, k_t, k_ϕ	Normal, tangential, and rotational stiffnesses connecting two particles in the lattice model
$\boldsymbol{k_e}$	Global stiffness matrix of the lattice element
$[K]$	Global stiffness matrix of the whole lattice mesh
$\hat{L}$	Specimen’s characteristic length
L	Split length in the splitting tension, or Brazilian, test
l_{43}	Lattice element width
l	Inner to outer loading points’ distance in the four-point bending simulation
M_i, M_j	Bending moments of the lattice frame element at the nodes i and j
N	Internal normal force of the lattice frame element
P	Concentrated applied load

Q	Internal shear force of the lattice frame element
q_n, q_t, q_ϕ	Components of $\boldsymbol{q}$ in the normal, tangential, and rotational directions
q	Coefficient defined in obtaining $\lvert K \rvert$
$\boldsymbol{q}$	Internal force vector between two particles in the lattice model
r	Radial distance from the crack tip
S_{ij}	Boundary segment common to the two contiguous particles i and j
S	Section modulus
$\boldsymbol{S}$	Stiffness matrix of a 2D lattice with frame elements
s_x, s_y	Grid size of the lattice mesh along x and y axes
T	Splitting tensile strength in the splitting tension, or Brazilian, test
$\boldsymbol{T}$	Transformation matrix
$t_r - \delta$	Traction-separation relationship
t	Lattice element thickness
$U(x, y)$	Airy stress function. Also called bi-harmonic function
$\{u\}$	Displacement vector of the lattice mesh
u_j, v_j	Components of displacement along x and y axes for material j, respectively
u_m, v_m, θ_m	Components of displacements and rotation of particle m in the lattice model in the global $x - y$ coordinates ($m = 1, 2$)
$\boldsymbol{u_e}$	Displacement vector in the lattice global $x - y$ coordinates for frame element e
V_i	Voronoi region or particle assigned to nucleus i
W_s	Work required to create new crack surfaces
$\boldsymbol{X_i}$	Coordinate vector for nucleus i
x, y	Global coordinates

z	Complex variable in the $x - y$ plane, $z = x + iy$
α	Dundur's elastic mismatch parameter
α'	Scalar factor to limit the contribution of bending in the lattice frame's fracture criterion
α^*	Bi-elastic coefficient in the Hilbert equation
α_0	Complex constant which is a measure of complex stress intensity factor
β	Dundur's elastic mismatch parameter
$\Gamma(\hat{\psi})$	Interface toughness as a function of phase angle $\hat{\psi}$
δ_n, δ_t, ϕ	Local displacements in the normal, tangential, and rotational directions
$\Delta u, \Delta v$	Relative crack flank displacements along x and y axes, respectively
$\varepsilon_1, \varepsilon_2, \varepsilon_3$	Principal strains
ε_M	von Mises strain
ε_{xy}	Shear Strain
$\varepsilon_x, \varepsilon_y$	Normal strain
ε	Bi-material elastic mismatch constant
θ	Argument of the complex number z
κ_j	Kolosov's constant: material parameter in terms of Poisson's ratio for material j
μ_b, μ_m	Shear moduli for brick and mortar
μ_j	Shear modulus of material j
μ_0	Friction coefficient
ν_j	Poisson's ratio of material j
Π	Total potential energy
σ_{eff}	Effective stress defined in the lattice frame's fracture criterion

$\sigma, \sigma_x, \sigma_y$	Normal stress
σ_{xy}	Shear stress
τ	Engineering shear stress
$\Phi_j(z), \Psi_j(z)$	Integrand of Complex Goursat functions for material j
$\phi(z), \chi(z)$	Complex Goursat functions
φ	Argument of the complex number $\Delta v + i\Delta u$
$\hat{\psi}$	Rotated loading phase angle
ψ	Loading phase angle
ω, γ	Angles defined in obtaining phase angle ψ

Chapter 1 INTRODUCTION

Masonry is the oldest building material which is still used in building constructions around the world for its low cost material and broad availability, its sound insulation properties, energy efficiency, and so on. Other influencing factors include cultural aspects, long time tradition, local knowledge of materials and tools, architectural reasons, etc. Construction simplicity is probably the most important characteristic of masonry structures among others like the aesthetics, solidity, durability and low maintenance, sound absorption and fire protection.

In addition to the above characteristics, masonry is a sustainable construction material. As a general definition, sustainability is concerned with promoting the most efficient use of resources, the protection of the environment and ecosystems, and the development of a more equitable world society, meeting the need of the present generation without compromising the ability of future generations to meet their own needs [1], [2]. Buildings and structures made of stone or brick masonry usually last for centuries with minimal maintenance. These durability and longevity features introduce masonries as environmentally and economically sustainable structures. For instance, there are approximately 40,000 masonry arch bridges in the UK which have been in daily use on highways, railways and canals for more than 100 years, with some of them over 500 years [1], [3]. Furthermore, around 25% of the 23 million residential properties in the UK, which are built out of brick or stone or some combination of these materials, have lasted for more than 160 years with satisfactory performance [1]. These characteristics are sufficient enough to motivate researchers and engineers to develop state of the art design rules for masonry structures, competitive to those of concrete and steel.

There have been important new developments in analyzing masonry structures in the form of composite material in the last decades. However, due to the lack of in-depth insight and models for the complex behavior of masonry composite consisting of brick, mortar, and their bond, its development of design rules has not kept pace with those of concrete and steel. This might be one main reason to prevent the innovative applications of structural masonry. Among other reasons are the lack of educational programs for most graduations of structural engineering and also the ability to transfer the academic knowledge into field practice.

1.1 Literature and Background

Unreinforced masonry, which is considered in this study, is a heterogeneous, inelastic, and anisotropic material made of two major components, brick units and mortar joints exhibiting very different stiffness, strength and ductility properties. The brick-mortar interface which is the weakest part in the masonry composite plays an important role in the failure of this assemblage. A number of investigations have been conducted on different aspects of masonry and the interface behavior between brick and mortar joints, where an interface element was usually considered with a continuum-based damage or plasticity formulation to account for the brick-mortar interface degradation ([4], [5], [6], [7], [8], [9], [10], [11], [12], [13]). Goodman et al. [4] were one of the first researchers who introduced the interface concept for joints in rock mechanics. Their joint element was designed to feature failure in tension and/or shear, rotation of blocks, development of arches. Page [5] of his seminal paper analyzed the behavior of clay masonry walls subjected to in-plane loading using an early version of finite element. The model considered masonry as a continuum of isotropic elastic bricks acting in concert with mortar layers as joint linkage elements. However, the ultimate load capacity of the masonry could not be predicted at that early stage. McNary and Abrams [14] studied biaxial tension-compression of bricks and triaxial compression of mortar to establish constitutive relations for each material. They simulated the force-displacement relationship for a stack-bond prism using a numerical model and a proposed strength theory. They concluded that mechanics of clay-unit masonry in compression could be represented by a single failure model and the most significant parameter to consider was the dilatant behavior of the mortar. Citto et al. [15] employed an innovative approach using digital image correlation (DIC) techniques to evaluate in-situ properties of the shear strength of mortar joints in existing masonry. They determined the properties of cohesion and friction angles in an existing masonry wall, and they used finite elements and the DIC system to investigate the significant lack of uniformity along the bed joints failing in shear. Lourenco [7], in his PhD dissertation, studied computational strategies for masonry structures. He considered micro- and macro-modeling strategies to analyze masonry composites. For the micro-modeling strategy, all inelastic phenomena were lumped in the relatively weak joints via a composite interface model, i.e., a zero-thickness interface element. Carol et al. [9] implemented an elasto-plastic fracture-based interface model to simulate the mechanical behavior of concrete and bone specimens as quasi-brittle materials. One of their main conclusions was that zero-thickness interface elements provide a convenient form of representing fracture as a mixed-mode generalization of the FCM, Fictitious Crack Model. They observed that, at the same time, the zero-thickness interface elements avoid some of the problems normally associated with this type of calculations using continuum elements with softening, such as mesh objectivity or deformation modes of the elements. Willam et al. [10] examined the degradation of interface transition zones in heterogeneous materials due to thermal and mechanical damage. Their study addressed model issues of zero-thickness cohesive–frictional interfaces which are subjected to thermal and mechanical damage. A combination of both thermal and mechanical degradation mechanisms was studied. Caballero, Willam, and Carol [12] developed a constitutive model for fracture simulations in quasi-brittle media within the framework of zero-thickness interface elements. An elasto-plastic interface model was presented by extending and improving the constitutive relations of an earlier 2D formulation to 3D with a consistent tangent formulation. Sacco, Alfano, and Toti ([11], [13]) evaluated masonry composites as heterogeneous systems made of brick and mortar joined by means of interfaces, responsible for the mortar-brick decohesion mechanisms. In their micromechanical computational strategy, a special interface model combining damage and friction was adopted. Their results obtained by a numerical model were put in comparison with the experimental ones, having shown the ability of the proposed model to simulate the behavior of the unreinforced and reinforced masonry arches in terms of ultimate load, nonlinear behavior and collapse mechanism. There have been many other studies on interface elements, cohesive elements, and their behavior in quasi-brittle materials like concrete and masonry, where efforts were made to better understand the behavior of masonry composites in material and ultimately in structural level employing experimental results and numerical simulations using continuum-based damage or plasticity formulation ([16], [17], [6], [18], [8], [19], [20]).

In the methods based on the theory of plasticity and damage mechanics, the displacement field is continuous over the domain and special techniques need to be accounted for embedding discontinuities and cracks on the domain. However, in the approaches based on fracture mechanics, the displacement field is discontinuous which accounts for the cracks and strong discontinuities. There have been rare investigations regarding the interfacial fracture properties and toughness of masonry interfaces. In many bi-material systems like composites and microelectronic devices, the fracture of interfaces is a critical phenomenon, which in many circumstances governs the failure behavior of those systems. The fracture of bi-material interfaces has been studied by many researchers. Muskhelishvili [21], in his pioneering work, employed the concept of complex variables and complex functions to represent the displacement and stress fields of plane problems using complex variables. He used complex functions since the properties of a complex variable are generally well-known. Williams [22] investigated the plane problem of dissimilar materials with a semi-infinite crack. He observed for the first time that stresses at the crack tip have an oscillatory character of type $r^{-1/2}\sin(\varepsilon \ln r)$, where r is the radial distance from the crack tip and ε is a function of bi-material elastic mismatch. Rice and Sih [23] developed a method for determining Goursat functions for dissimilar materials bonded along straight-line interfaces. They combined an Eigen-function expansion method with the complex equations of Muskhelishvili to solve the problems of isolated forces on surface of a semi-infinite crack and an infinite plate with a crack subjected to stresses at infinity. England [24], Erdogan

[25], and Rice [26] also investigated the singular near-tip field of the interface crack problems. Parks [27] developed the “virtual crack extension” method which is a Finite Element technique for determining elastic crack tip stress intensity factors. In this method, the single crack is “advanced” by moving nodal points rather than by removing nodal tractions at the crack tip and performing a second analysis. Charalambides and his colleagues [28] devised an interesting test specimen which is capable of measuring the fracture resistance of bi-material interfaces. The test specimen is a four-point bending beam made of two dissimilar materials with a notch at the middle of the beam, as shown in Figure 1-1. In their numerical Finite Element solutions, they obtained graphs for the energy release rate, stress intensity factor, and loading phase angle considering a pre-cracked notched symmetric composite beam model. Matos et al. [29] presented a numerical method for calculating stress intensity factors in bi-material interfaces. Their method is based on the J-integral using the “virtual crack extension” method, or the energy method developed by Parks [27][30]. They compared the stress intensities obtained by the energy method and the “crack surface displacement” method. Charalambides et al. and Matos et al., in their simulations, considered a pre-cracked Finite Element mesh with length a and applied the virtual crack extension method by virtually increasing the crack length and changing the stiffness of a ring of elements around the crack tip [27]. Their simulation was not based on a progressive crack propagation along the interface where the crack length a increases during a single simulation. Evans et al. studied the fracture energy of bi-material interfaces and relative toughness of some bi-material interfaces with respect to the phase angle of loading [31].

Hutchinson and Suo [32], in their comprehensive paper, reviewed the investigations on fracture of layered materials including bi-material interfacial fracture mechanics.

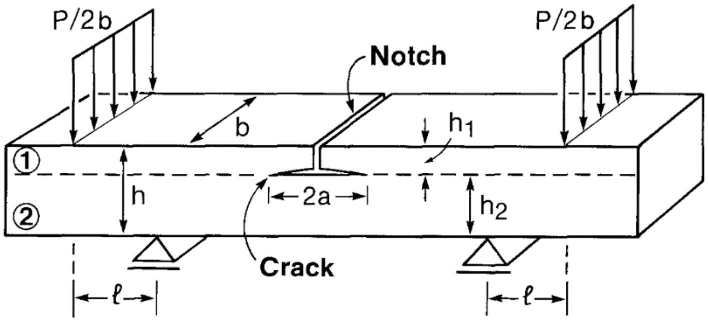

Figure 1-1 The pre-notched bi-material four-point bending beam with two symmetrical interfacial cracks [28]

1.2 Objectives and Scope

The ultimate outcomes of most research on masonry structures in Civil Engineering might be used to enhance and review current design rules. To do so, the importance of sophisticated numerical tools, capable of predicting the behavior of the structure from the linear stage, through cracking and degradation until complete loss of strength is clear. It is then possible to control the serviceability limit states, fully understand failure mechanisms, and reliably assess the structural safety. This objective can be achieved not only by implementing accurate and robust constitutive models, but also by measuring material parameters of masonry constituents in the linear and especially post-peak stages through precise and laborious experimental programs. Depending on the numerical modeling strategy, these constituents include brick units, mortar joints, and/or cohesive zones between brick and mortar, which are the weakest part in a masonry structure. If a micro- or meso-level modeling strategy is considered, then the interface elements may be added to other two constituents, i.e., brick and mortar, in the numerical model. At this level of modeling, material properties of the constituents and the interface are needed, which can be measured by small-scale experimental programs. Nonetheless, the brick-mortar interface data is generally neglected in large-scale and practice-oriented analyses, where a macro-level modeling strategy is taken into account. In this case, the masonry structure is regarded as an anisotropic homogenized material having a constitutive relationship between average masonry strains and average masonry stresses.

This study focuses on the nonlinear analysis of brick-mortar interface in unreinforced masonry composites under static monotonic loads at the micro level of observation. A numerical approach based on the fracture mechanics concepts, where the displacement field is discontinuous, accounting for the cracks and strong discontinuities, is employed. The primary aim of this research is the implementation, development, and evaluation of a numerical tool at the micro-level which is fairly capable of evaluating and predicting the behavior of any bi-material interface, like brick-mortar bond, in a fracture mechanics context. The objectives of this study are as follows:

- Conducting some material level tests to measure the required material properties of brick, mortar, and their interface.
- Simulating the failure modes of the brick-mortar interface to answer the question whether it is a mode 1 or mode 2 or a mixed mode failure which could help extract ‘true’ material properties of the interface from small scale material level test.

- Implementing and developing a numerical tool which simulates progressive crack propagation through the interface or brick and mortar to capture debonding in tension and delamination in shear while localization of fracture processes introduces snap-back instabilities.
- Obtaining brick-mortar interface fracture properties like energy release rate and stress intensity factors for mode 1 and 2 from the numerical tool.
- Determining the toughness relation of bi-material interfaces by the micro-level simulation.
- Obtaining the required fracture energy values of continuum-based cohesive zone models in the form of zero-thickness traction-separation law in the meso-level from the micro-level modeling outputs.

It is important, however, to note that masonry experimental results typically show wide scatter numbers, not only in large scale tests but also in small scale specimens, as observed many times in this study. Thus, a sharp reproduction of the experimental results in the form of a load-displacement curve, for example, is not the main concern. It should be mentioned that the developed model and the discussion in this study probably have a much broader applicability than just masonry structures. It is expected that the micro-model can also be evaluated in other areas like adhesives, joints in rock and stone works, contact problems between bodies, microelectronic devices, and, in general, all types of interface behavior where bonding, cohesion, and friction between constituents form the basic mechanical actions.

Chapter 2 explains about the material level tests of the masonry composite carried out in the form of brick, mortar, and brick-mortar interface tests. It mainly focuses on the failure mode and strength of each test. To this end, a Digital Image Correlation, DIC, system was used to examine the failure mode, strain concentrations and crack propagation paths on the surface of specimens and the effect of bond on the overall behavior of the masonry composite.

Chapter 3 deals with the theoretical framework and the numerical modeling method used to simulate the behavior of interfaces. The 2D lattice model geometry and Voronoi diagram to discretize the continuum domain is first explained. The material structure overlay technique is then discussed which assigns various material properties to the lattice elements depending on their specific coordinates in the mesh. An existing constitutive relation capable of modeling the zero-thickness interface elements is adopted in the lattice model. The chapter ends with the explanation of the fracture criteria for the brick, mortar, and interface struts followed by a section about a few masonry test configurations simulated by the lattice.

Chapter 4 explains about the essentials of the interfacial fracture mechanics and the way it was developed into the existing formulations for the bi-material interface cracks. It first describes the Dundur’s parameters which characterize mismatches in the in-plane tensile and bulk moduli across the bi-material interface, introduced by different elastic properties of abutting dissimilar materials. Muskhelishvili’s equations based on complex variable function which are used in solving crack problems in homogeneous and heterogeneous bi-material systems are then elaborated.

In Chapter 5, an energy method is used in the lattice model to obtain the energy release rate of an interface crack propagating along the bond. This method is then employed to validate the lattice's energy release rate and stress intensity factors by comparing the lattice results with three classic problems in fracture mechanics for which analytical solutions are available. Validation of the model was performed by using a regular square mesh.

Chapter 6 presents the results of the validated lattice model obtained from three numerical simulations in masonry composites in pure bending, tension, and double-lap shearing . The energy release rate, the loading phase angle, and stress intensity factors for mode 1 and mode 2 are the main quantities obtained by the lattice approach. Mesh sensitivity analyses were also conducted to compare the interfacial fracture results of a fine mesh with those of a coarse one. The critical energy release rate values by the lattice are then devoted in obtaining the masonry interface toughness relation and also the critical fracture energy of a traction-separation zero-thickness interface element in meso-level continuum finite element formulation. These energy values are also used in homogenizing a heterogeneous anisotropic masonry unit cell in direct tension to a homogeneous isotropic continuum finite element using the energy equivalence concept.

Chapter 7 presents the summary and final conclusions which can be derived from this study.

Chapter 2 MATERIAL LEVEL LABORATORY EXPERIMENTS

This chapter briefly focuses on experimental observations of fired clay bricks and mortar specimens along with their interface at the constituent levels, in addition to their composite behavior when brick and mortar are stacked as a prism and are tested in direct compression. The experimental observations include Digital Image Correlation, D.I.C., data from a 3D system to ascertain the effect of bond on the overall behavior of the masonry composite. In the following, this D.I.C. system is shortly explained; then the small scale material level tests are discussed. At the end, the behavior of a masonry prism in direct compression is evaluated.

2.1 Digital Image Correlation System

For image analysis, the Digital Image Correlation system, and its software named ARAMIS [33] was used in all experiments. In the DIC technique, the software processes the images taken during the test to determine the full-field motion of the speckle geometry, and obtains surface deformations in terms of strain measurements. The DIC setup used for this study, is a non-contact optical 3D metrology system in which the ARAMIS software analyzes, calculates and documents deformations at prescribed load steps. The setup consists of four pairs of 12 Megapixel Gigabit Ethernet cameras connected to a sensor controller for power supply of the cameras and to record speckle images in pixel format. The PC-based ARAMIS software assigns square or rectangular image details in the form of so-called facets, e.g., 15 x 15 pixels, for tracking their motion over the deformation history of the test article [33].

There are steps to accomplish a typical measuring procedure, some of which are related to specimen preparation, calibration of the measuring volume, creating a new project and defining its parameters like facet size, facet steps, computation size, gauge length, and so forth [33]. In order to measure a specimen's deformation using ARAMIS system, its surface facing towards the cameras must meet some requirements like being smooth, having a stochastic pattern with good contrast to clearly allocate the pixels in the camera images called facets, being non-glossy and dull, being free of grease and oil, etc. In this study, a plain spray paint was used to create stochastic patterns on the specimen surface. Satin or gloss paints were avoided because of their reflections under lighting. First, a white and dull base coat was applied on the specimen's surface followed by spraying black dots to generate a random speckle pattern. Smaller measuring volumes require a finer pattern than larger measuring ones. Figure 2-1 shows a standard masonry prism prepared with a random dot pattern.

Figure 2-1 Stochastic patterns sprayed on a masonry prism surface.

2.2 Material Level Tests

Accurate mirco-modeling of masonry structures requires a thorough experimental description of the material. In the present study, three types of material tests were considered for the numerical analyses, viz. sintered clay brick units without holes, mortar joints, and brick-mortar interface. When the masonry prism is under axial compression, the mortar joints generally experience triaxial compression while the brick units are subjected to axial compression and lateral biaxial tension due to the Poisson's mismatch properties of mortar and brick units. Softer mortar joints generate lateral tension in the bricks through their interface bond leading to tensile cracking in the form of axial splitting of the brick units. This failure initiates in the brick units and propagates through mortar joints. Since the brick is in biaxial lateral tension and axial compression, its tensile and compressive strengths and its failure mode are of particular interest. The compressive strength of the mortar prism was also investigated under axial compression. Moreover, to investigate mode 1 and mode 2 failure behavior of the cohesive zone between brick and mortar, direct tensile and triplet tests were conducted to elaborate the behavior of the bond in tension and shear. However, a fundamental question is whether the failure mode in the triplet test is due to tensile debonding (mode 1) or shear delamination (mode 2) or combination of them (mixed mode). This question will be addressed later on. A Tinius-Olsen axial tension-compression material testing machine with maximum capacity of $400\ (kips)$ was used for most tests in this experimental investigation. Also, the DIC system was used for all tests to capture the full-field deformation of test specimens at different load stages of axial displacement control.

2.2.1 Fired clay brick units

The solid brick units of nominal size of $2 \times 4 \times 8\ (in)$ were acquired from a well-known local company in Houston, Texas. Three randomly selected bricks were used for compression and three for splitting tension tests, also known as the Brazilian test. The splitting tension test complies with the specifications of ASTM C 1006-84 [34]. Figure 2-2 shows a typical brick specimen painted and prepared for a compression test [35].

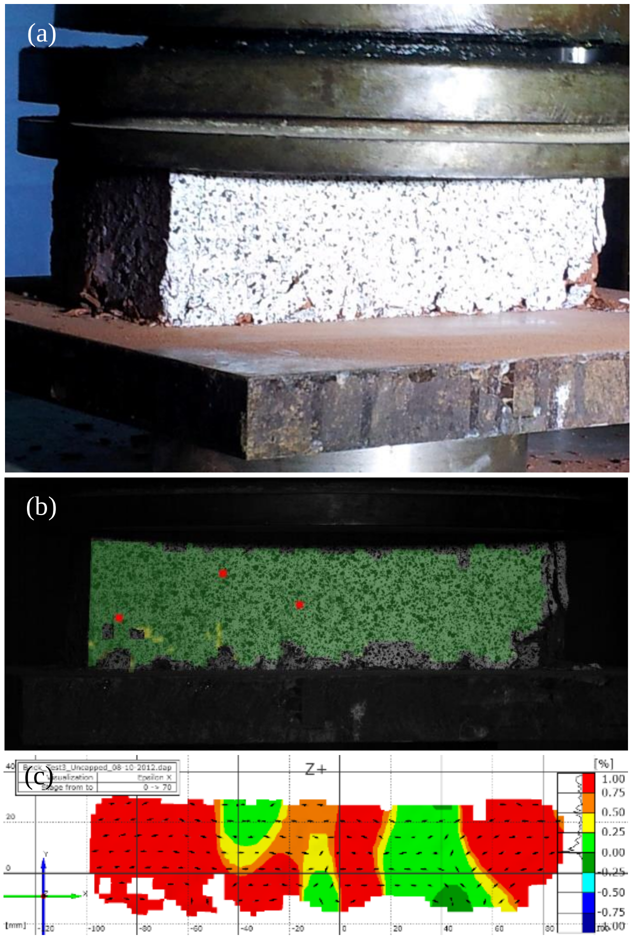

Figure 2-2 Brick specimen under direct compression at the load level of 180 kips $(0.87P_{max})$*. (a) The brick with speckles; (b) The snapshot taken by the DIC software; (c)* ε_x *contours on the surface of the brick.*

Figure 2-2(a) and Figure 2-2(b) illustrate the speckles on the surface of a tested brick taken by a regular camera and DIC software, respectively. Figure 2-2(c) represents the distribution of ε_x contours on the brick's surface shown in Figure 2-2(a). The dark green contours correspond to lateral contraction, i.e., negative ε_x strain values contradicting the Poisson effect. However, this may be explained by the boundary effects at the two brick surfaces. Other colors are related to different levels of lateral tensile strain. An average compressive strength of $6000\ (psi)$ was measured for these three bricks with a standard deviation of 143 (psi).

Moreover, splitting tension tests were conducted on three brick units. In the test, two line loads along the bed surfaces of the brick were applied. The compressive load, imposed by $0.25\ (in)$ in diameter bearing rods, results in a tensile stress distributed over the height of the brick over the split length of the unit. The splitting tensile strength of the bricks is calculated according to the traditional expression for split tensile testing as

$$T = \frac{2P}{\pi L h_b}\ , \qquad (2\text{-}1)$$

where T is splitting tensile strength (psi), P is maximum applied load indicated by the testing machine (lbf), L is split length (width) of the brick (in), and h_b is height of the brick (in). The average splitting tensile strength for the three bricks was $400\ (psi)$ with a standard deviation of 75 (psi), which is close to a typical value of concrete. Figure 2-3 illustrates the splitting tension test performed on one brick. Figure 2-3(a) shows the painted brick after the test with a vertical mode 1 crack through its height. Figure 2-3(b) exhibits the photo taken by the DIC system right after the failure, while Figure 2-3(c) depicts the distribution of ε_x and major principal strains' directions on the surface of the brick right before the failure. As it can be seen, there are strain concentrations (red colors) right below and above the bearing rods on the middle top and bottom of the brick. This coincides with what is expected in the Brazilian test setup. Other parts of the brick surface are almost free of deformations showing green color.

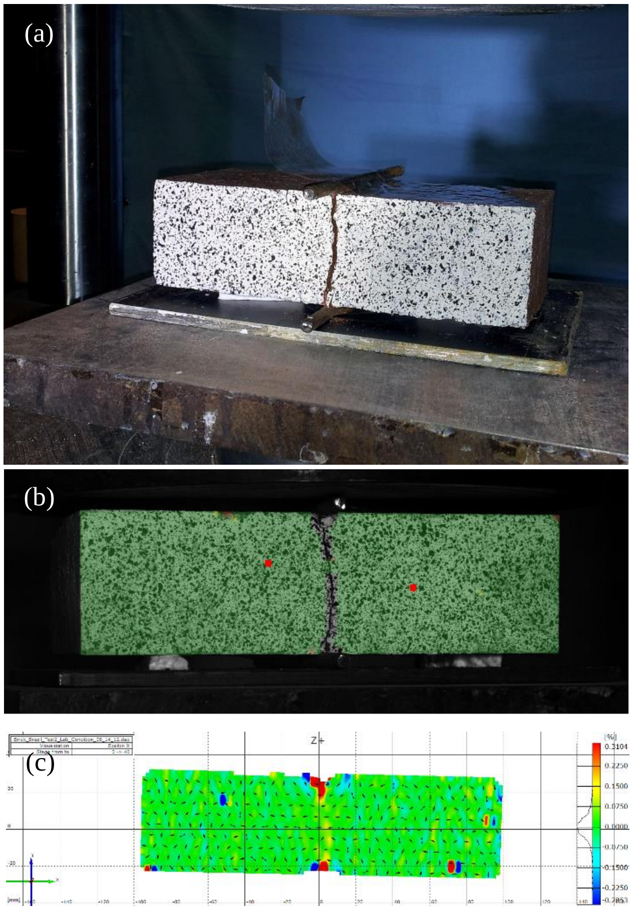

Figure 2-3 Brick specimen in splitting tension test failed at the load level of 6.1 kips. (a) The brick with speckles after the test, (b) The snapshot taken by the DIC software right after the failure, (c) ε_x contours on the surface of the brick right before the tensile splitting.

2.2.2 Mortar prisms

Mortar mixture for these tests was prepared with a 4:1 sand to cement ratio and a W/C ratio of 0.56 for this experimental test program [36]. The mixture was formed as a prism surrounded by brick surfaces the dimensions of which were $4 \times 4 \times 2\ (in)$. The mortar prisms were cured for 14 and 28 days inside a moisture-tight bag. They were tested in axial compression under displacement control at the same displacement rate as the brick units. Figure 2-4 illustrates a mortar prism tested in this study under axial compression.

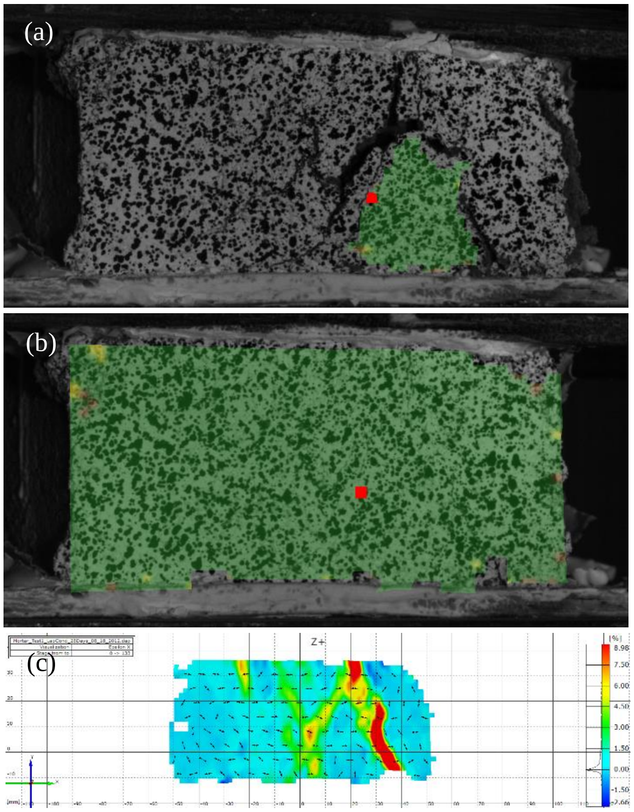

Figure 2-4 Mortar prism specimen cured for 28 days under direct compression at the load level of 40.9 kips ($0.97P_{max}$). (a) The mortar after failure, (b) The snapshot taken by the DIC software at $0.97P_{max}$, (c) ε_x contours on the surface of the mortar at $0.97P_{max}$.

Figure 2-4(b) and (c) show the mortar very close to its failure. As can be seen, the DIC software can capture the strain concentrations on the surface of the specimen. If Figure 2-4(a) is compared with Figure 2-4(c), it is evident that the fracture trajectory closely matches with the one for ε_x concentration. Figure 2-5 illustrates the major strain distribution and its directions along the surface of the same mortar shown in Figure 2-4.

Viewing Figure 2-4(a) and Figure 2-5, we may conclude that the ARAMIS system can locate the crack path 'before failure' by measuring the increasing rate of localized deformations. Attention should also be paid to the principal strains. Figure 2-5 depicts the direction of the major principal strains which are oriented perpendicularly to the trajectory of the strain concentrations. To explore also whether the failure mode is 1 or 2 type, one might look at the von Mises strain contours as depicted in Figure 2-6. It is observed that there are also high von Mises strains at the location of cracks. This means that the fracture mechanisms are a combination of mode 1 and mode 2, or a mixed mode failure condition. The average compressive strength measured for these mortar specimens was $2000\ (psi)$ with a standard deviation of $751\ (psi)$.

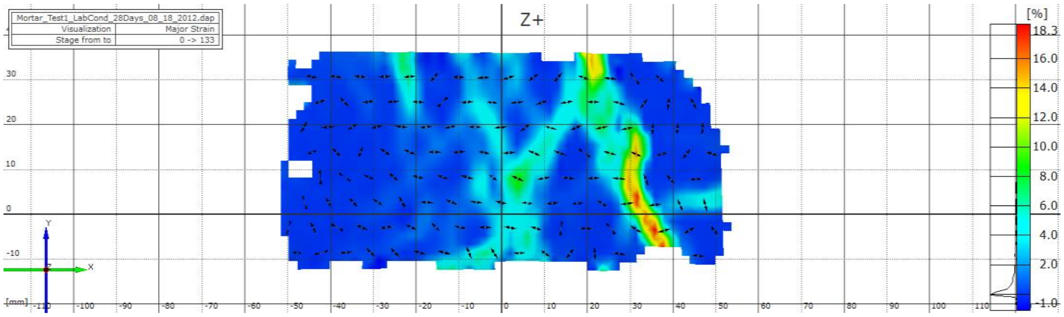

Figure 2-5 Major strain distribution and its direction on the surface of the mortar prism at $0.97P_{max}$ captured by the DIC system.

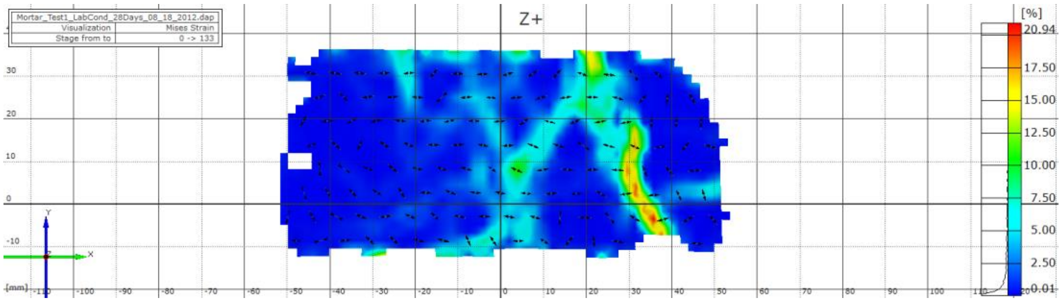

Figure 2-6 Mises strain distribution on the surface of the mortar prism at $0.97P_{max}$ captured by the DIC system.

2.2.3 Brick-mortar interface

The bond between the brick unit and mortar joint is often the weakest link in the masonry assemblage. Exploring the mechanical behavior of this link is the key in the failure analysis of masonry structures. Since two different phenomena occur in the brick-mortar interface, one associated with tensile failure, mode 1, and the other associated with shear failure, mode 2, two types of tests were conducted in this study, namely direct tensile tests of interface, and also triplet tests.

2.2.3.1 Interface direct tension test

The purpose of this test is to measure the tensile strength of the brick-mortar bond. It was attempted to avoid any eccentricity during the test to only measure the mode 1 behavior of the bond. Figure 2-7 shows the test setup and the specimen for measuring the mode 1 behavior of the interface.

Figure 2-7 Test setup and the two-brick masonry prism specimen for the direct tensile test.

Brick units were cut according to the maximum opening of grips. As can be seen in the figure, the DIC system and an extensometer were employed to measure the delicate deformation of the interface. Four specimens were tested by this $10-kip$ machine. Working with a gear box setup, the machine had not been equipped with a servo-controlled system to apply a displacement control test in a consistent manner. Moreover, the machine's grips were not properly concentric which imposed an unavoidable eccentricity to the specimen. However, a tensile strength of about $47\,(psi)$ were measured for the specimens.

2.2.3.2 Triplet test

In addition to tension experiments, 17 additional tests were performed in order to explore the shear response of the brick-mortar interface in the form of double-lap shearing tests. Uniaxial and biaxial loading configurations are needed to test the specimens under no confinement and confinement lateral loading. To this end, the Tinius Olsen machine equipped with servo-controlled system and a $10 - kip$ manual hydraulic jack were employed. Under no confinement conditions, where a uniaxial loading exists, the Tinus Olsen frame was only used in displacement control. Under confined loading cases, it is needed to keep the lateral load constant while shear load increases. Thus, the lateral constant load was applied by the Tinius machine in load control while applying shear load with the manual jack keeping the load rate constant. For the unconfined cases, the loading and support arrangement is similar to a standard conventional double lap shear test for the determination of the bond shear strength of masonry joints [37].

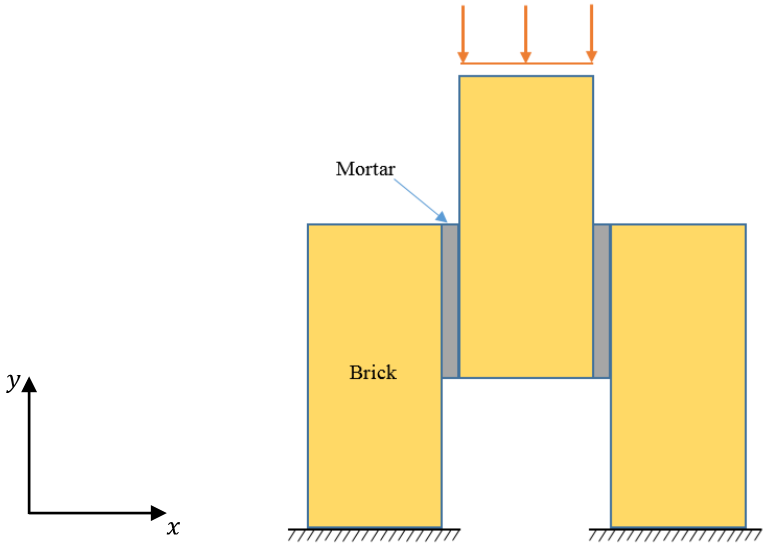

Figure 2-8 Unconfined conventional triplet test to evaluate the brick-mortar interface behavior in mode 2.

Figure 2-8 shows a conventional triplet configuration used in this research. The DIC system was also used to follow the crack propagation and mode 1/mode 2 deformation field. Figure 2-9 illustrates the deformation field of a triplet specimen captured by the DIC system. The vertical shear load was applied by the Tinius machine. Based on the values of ε_x and ε_{xy} on the inner interface, which are shown by red concentrated color, the failure mode is a combination of mode 1/mode 2, namely mixed mode. The values of shear strain for mode 2 is much larger than that of mode 1, Figure 2-9(a), (b). The value of ε_y is negligible compared with two other strains, Figure 2-9(c), implying that the interface stretch strain could be neglected on the failing interface. In other words, surface failure dominates volumetric fracture supporting the idea of using zero-thickness interfaces between brick and mortar in numerical modelings as opposed to the finite thickness interfaces.

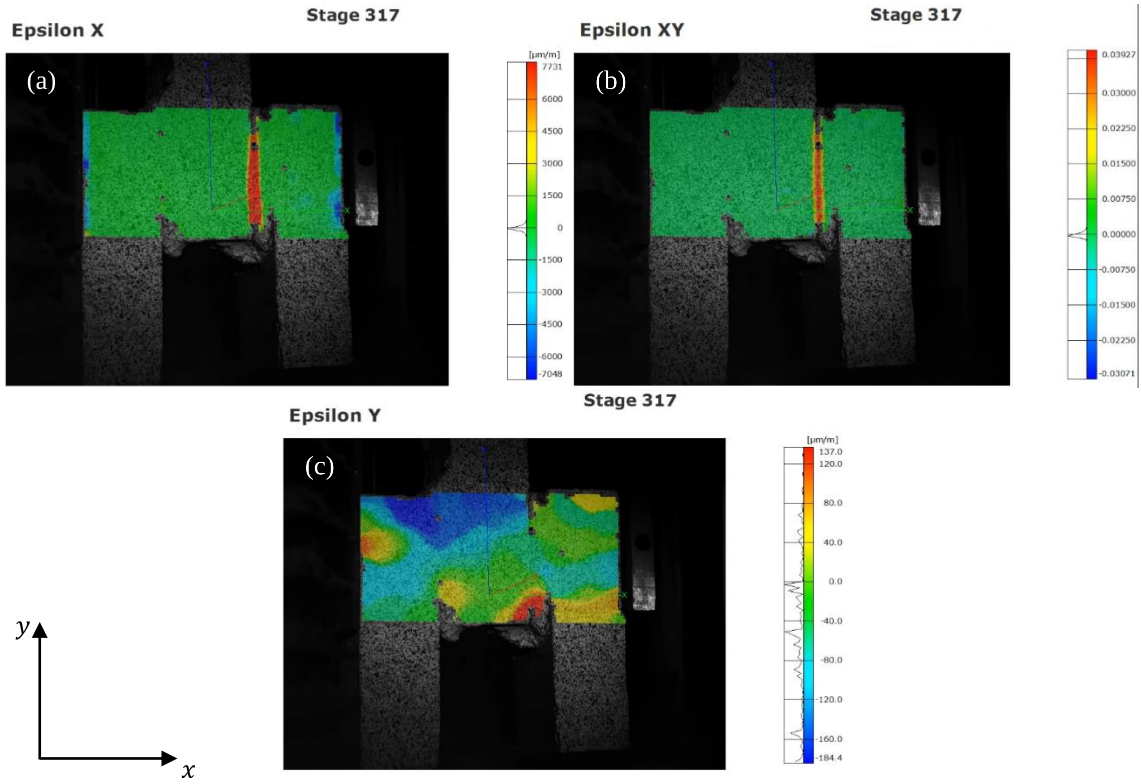

Figure 2-9 Strain field of an unconfined triplet test specimen captured by the DIC system right before the failure.

Figure 2-10 depicts the deformation of a confined triplet specimen right before the failure of the interface. Comparing Figure 2-10(a) and (b), it is seen that the value of shear strain, i.e., mode 2, is a bit smaller than that of mode 1 signifying a mixed mode failure. The magnitude of the interface stretch, ε_x, is again negligible in this case, compared to ε_y and ε_{xy} on the inner interface.

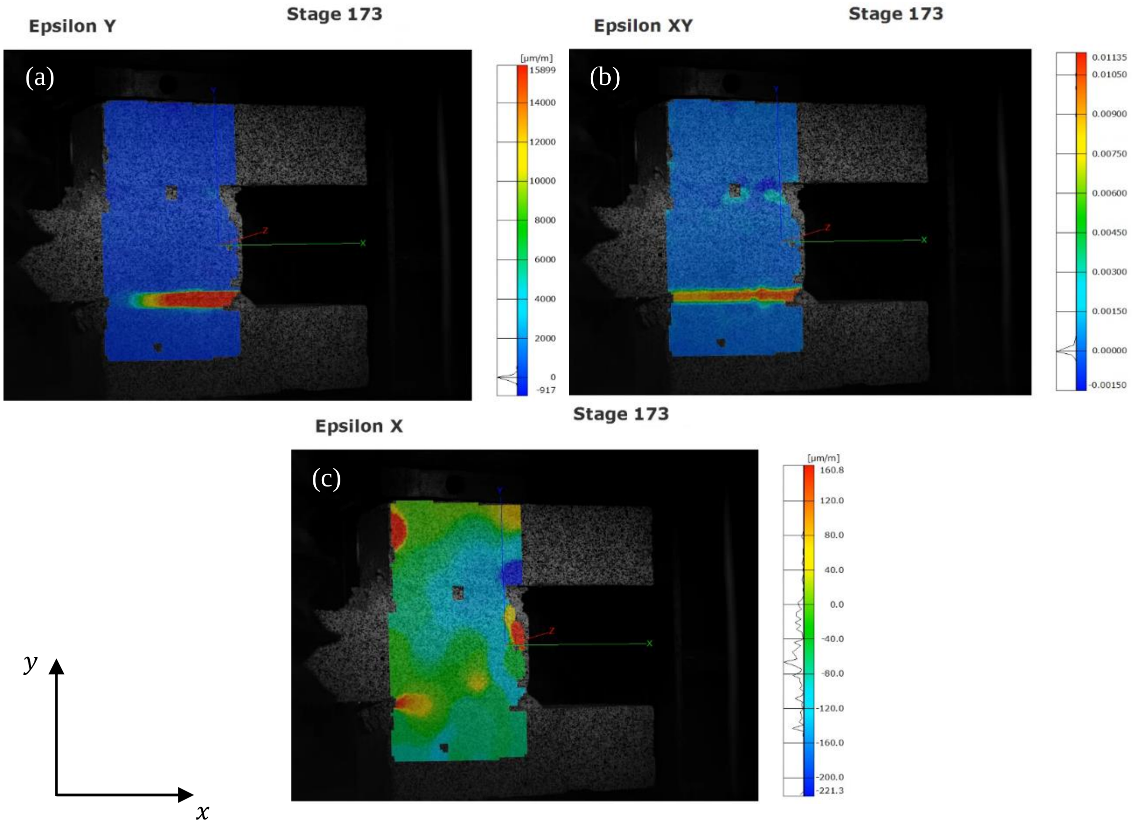

Figure 2-10 Strain field of a confined triplet test specimen captured by the DIC system right before the failure.

Specimens were tested under no confinement and different confining loads. It is known that the shear strength of masonry joints increases with increasing the applied confining load up to a maximum value which is related to the compressive strength of material. The relationship between the shear strength of brick-mortar interface, τ, and the confining stress, σ, can adequately be expressed by the classical Coulomb failure function of the form

$$\tau = \mu_0 \sigma + \tau_0 \,, \tag{2-2}$$

where τ_0 is the shear strength at zero confining stress, and μ_0 can be considered as the coefficient of internal friction. According to the triplet test results, the estimated values of

τ_0 and μ_0 may be approximated by 179.68 (psi) and 0.662, respectively. Figure 2-11 illustrates Coulomb failure envelope for the triplet specimens under different confinements.

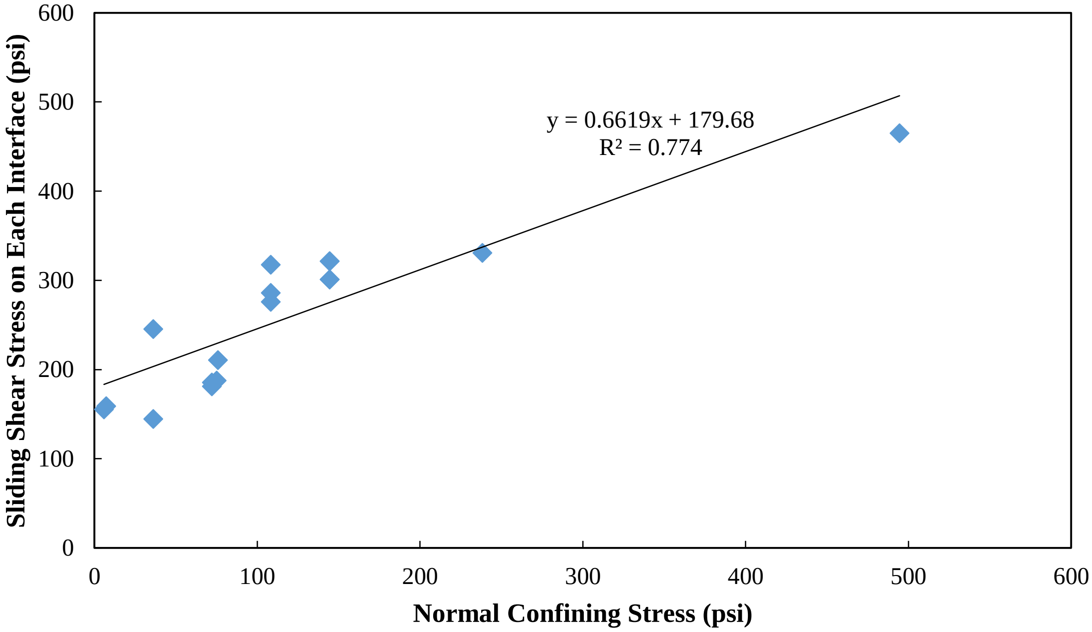

Figure 2-11 Coulomb failure envelope for the triplet specimens under different confinements.

2.3 Uniaxial Compressive Behavior of Masonry Prism

The masonry prisms were made of five brick units from the same mentioned source and four mortar layers from the same cement and aggregates and mix proportions. They were constructed according to the specifications of ASTM C 1314 – 03b [38]. Figure 2-1 shows a typical masonry prism prepared for this study the height of which is 12 (in). The prisms were tested under a direct compression in displacement control with the same displacement rate as the brick units' and mortar prisms' [35].

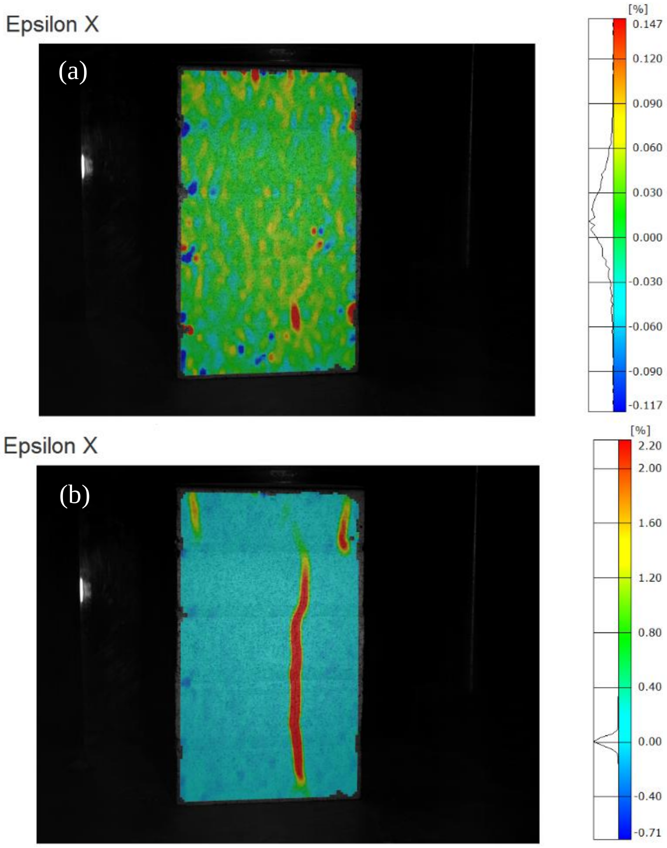

Figure 2-12 Distribution of ε_x on the surface of the masonry prism during the direct compression test. (a) ε_x contours at 0.5P_{max} , (b) ε_x contours at P_{max}.

Figure 2-12(a) and (b) illustrate the distribution of ε_x contours for one of the specimens at the load level of 88 and 171 $(kips)$, respectively. In Figure 2-12(a), most of the lateral strain field (see the strain bar) exhibits positive ε_x-values with some vertical strain concentrations having been developed, i.e., yellow color. Figure 2-12(b) shows the development of a vertical crack at failure. The DIC system captures the concentrations of lateral strain depicting the axial crack location and orientation. If the propagation history of the crack evolution is considered, it may be observed that the vertical crack propagates from the bottom to the top of the masonry prism in this case. The crack initiates at a load level of 35 $(kips)$ at the lowest mortar layer somewhere at the brick-mortar interface, about $2.4\,(in)$ from the bottom of the prism, and then propagates upward under increasing load until the prism splits into two parts.

Moreover, to observe the effect of shear of the mortar joints which is caused by the deformation mismatch effects explained earlier, the von Mises strain criterion was considered as

$$\varepsilon_M = \sqrt{\tfrac{1}{2}[(\varepsilon_1 - \varepsilon_2)^2 + (\varepsilon_2 - \varepsilon_3)^2 + (\varepsilon_3 - \varepsilon_1)^2]}\,, \tag{2-3}$$

where, ε_1, ε_2, and ε_3 are major principal strains and ε_M is the von Mises strain. Figure 2-13 illustrates the distribution of ε_M on the surface of the same masonry prism captured by the DIC system during the direct compression test. Figure 2-13(a) shows the prism after failure. A comparison can be made between Figure 2-13(a) and Figure 2-13(c) or Figure 2-12(b). It is seen that the DIC system measures the deformations in real-time during the test and at the end it captures the real crack pattern of axial splitting.

As expected, the softer mortar layers experience higher shear strains than the stiffer bricks. This is evident in Figure 2-13(b) and (c) where a lighter blue color is seen at the top mortar layer at $0.5P_{max}$. The fact that these Mises strain concentrations are not observed at the two bottom layers is probably because of the bottom to top order of construction of the prism where bottom ones experienced higher weight imposed by the upper bricks and mortar joints than the top layers during the construction of the prism. This probably induced more load on the bottom mortar layers due to the weight of top material layers mitigating the shear deformations caused by the mismatch effects. It is also observed that the brick-mortar interface behavior is not captured in this type of test.

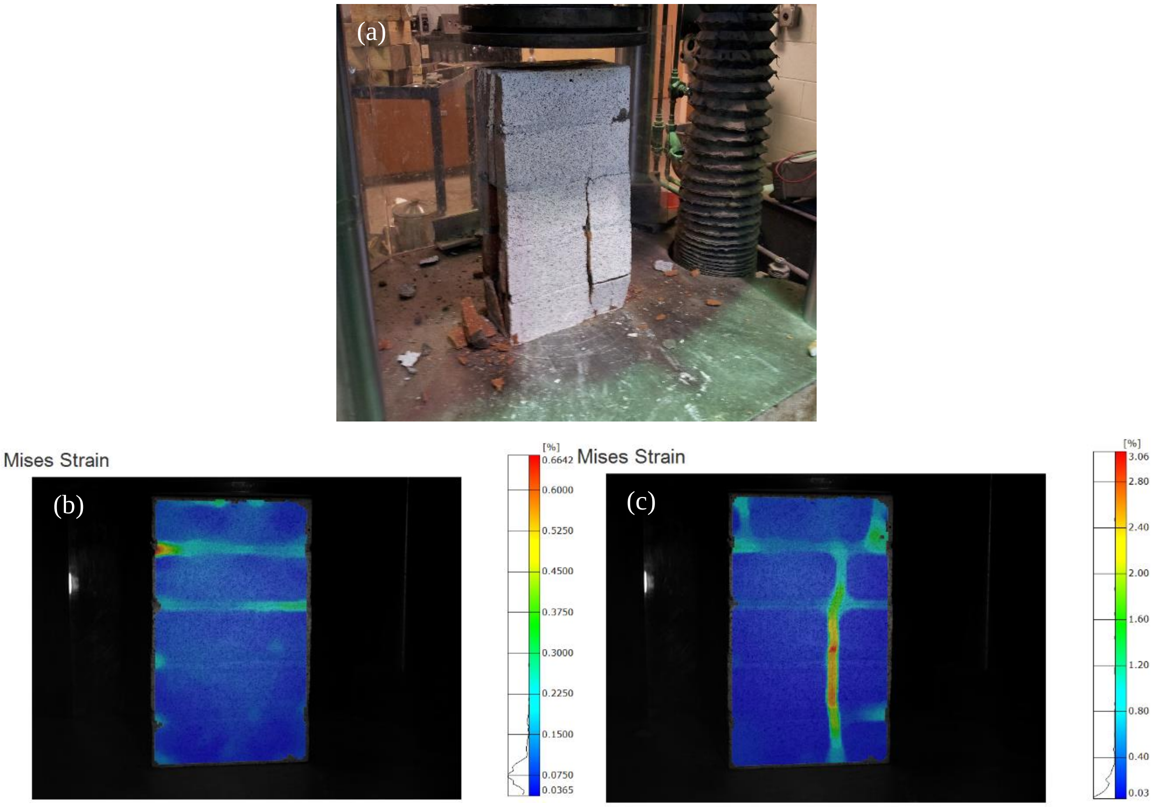

Figure 2-13 Distribution of ε_M*, Mises strain, on the surface of the masonry prism during the direct compression test. (a) The failed masonry prism after the direct compression test. (b)* ε_M *contours at 0.5*P_{max} *, (c)* ε_M *contours at* P_{max}*.*

2.4 Summary

The behavior of brick units, mortar prisms, and their interface was evaluated by conducting some material level tests. The DIC system was employed throughout the experiments to observe and measure the full-field deformations of the specimens. Compared to the traditional way of using strain gauges which only measure extensional deformations at a limited number of discrete locations, the photogrammetry method used by the DIC system provides field information by measuring a very large number of data points dependent on the computation size, facet size and facet steps. It also captures in-plane and out-of-plane deformations simultaneously. Moreover, one of the main advantages of using the DIC system is measuring large deformations and strain concentrations on the surface of a specimen, while strain gauges often debond under large deformations. Therefore, in some studies which deal with large deformations like in damage or fracture mechanics, the DIC system is very useful to track deformations up to failure. Furthermore, the DIC system measures real-time deformations during the test and provides at the end a crack pattern that closely matches that of the real specimen. This gives the DIC system an opportunity to provide feedback to the testing machine through measurement of the deformations in real-time. However, the DIC system shows some inconsistencies in measuring small deformations in brittle materials like brick and mortars. For instance, for the three 14-day mortar prisms tested, the average chord young's moduli were 4518, 1857, and 7267 (ksi) showing no consistencies. The issue is much worse for the Poisson's ratio where the lateral horizontal strain, ε_x, is much smaller than the vertical strain, ε_y, causing erratic results in the linear stage which is determined based on the load-deformation curve of each specimen. The problem also persists for the brick units. Therefore, the values of Young's modulus and Poisson's ratio for brick and mortar were adopted based on the all measured values by the DIC and those reported in the literature.

Unreinforced masonry is a heterogeneous, inelastic, and anisotropic material made of two major components, brick units and mortar joints exhibiting very different stiffness, strength and ductility properties. When these two constituents are assembled in the form of a masonry prism, axial splitting of the prism is observed under compressive loading due to the mismatch conditions of the masonry composite. This mismatch results from the different response behavior of the stiff brick units and the soft mortar layers generating triaxial stress and deformation conditions in the brick unit and the mortar joint. This means that under direct compression of the masonry prism test the softer mortar joints are restrained by the brick units from lateral expansion and hence experience triaxial confinement, while the stiffer brick units are subjected to lateral tension besides far-field axial compression.

Chapter 3 NUMERICAL LATTICE MODEL

Heterogeneous materials exhibit complicated fracture mechanisms due to their microstructure. Analytical descriptions of these mechanisms using linear elastic fracture mechanics is difficult, since the fracture pattern includes a main crack, itself consists of various branches, secondary cracks, and microcracks. Due to the limitations and inflexible nature of analytical methods in handling arbitrary complex geometries and boundary conditions and general crack propagations, fracture processes in heterogeneous materials are, therefore, often simulated with numerical models. One of the numerical tools which is well suited for fracture simulations is the lattice model. The following sections explain the concepts, definitions, assumptions, and methods used in this study to implement the lattice model in *MATLAB R2014a* [39] as a tool in computational fracture mechanics.

3.1 Lattice Geometry and Voronoi Diagram

The main concept of the lattice model was first introduced by Hrennikoff [40] in 1941, where a continuum domain can be discretized by a lattice of truss, beam, or frame elements. He replaced the continuous elastic panel by a framework of equivalent bar or strut members with elastic properties based on the properties of the continuum domain. Voronoi diagrams, based on a random or regular distribution of points, were used in this study to discretize the continuum domain into an assemblage of convex rigid particles interconnected along their boundaries through flexible common sides or interfaces [41] (See Figure 3-1). A planar Voronoi diagram is defined as [42] “Given a set of two or more but a finite number of distinct points in the Euclidean plane, all locations in that space are associated with the closest number(s) of the point set with respect to the Euclidean distance. The result is a tessellation of the plane into a set of regions associated with members of the point set. This tessellation is called the *planar Voronoi diagram* generated by the point set, and the regions constituting the Voronoi diagram is referred to as *Voronoi polygons*."

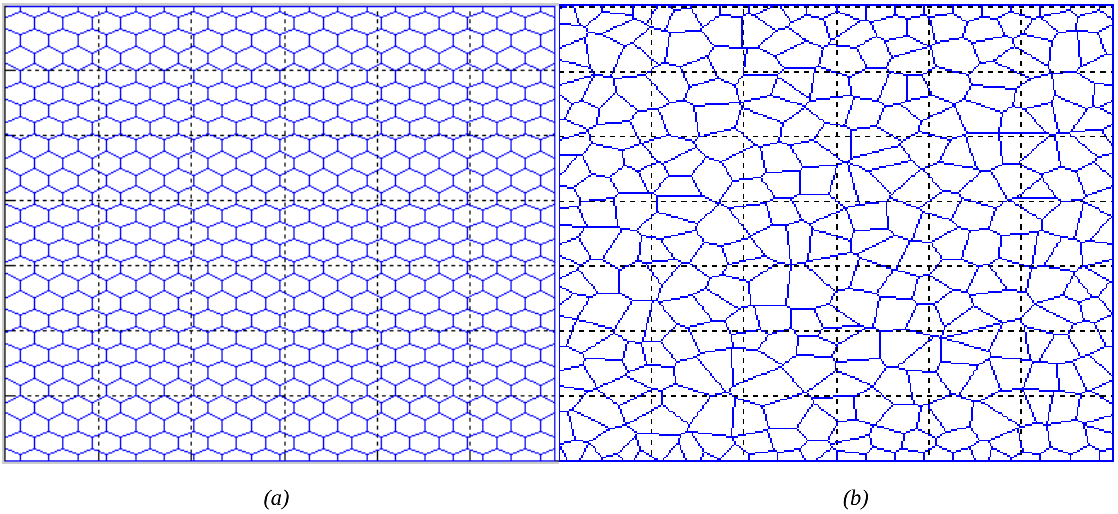

Figure 3-1 Discretization of a rectangular continuum domain into particles using Voronoi formulation. (a) a regular discretization, (b) a random discretization.

These Voronoi polygons or convex rigid particles are, for example, regular hexagons as shown in Figure 3-1(a). Each particle, in the Voronoi diagram, has a point inside called nucleus or centroid which has a specific geometric definition. A truss or beam or frame element connects these nuclei inside the particles constructing a discretized lattice mesh. Figure 3-2 illustrates the generated mesh for a regular and random nuclei distribution according to the Voronoi diagram. This diagram is uniquely defined by the nuclei distribution. The Voronoi region, or cell, assigned to nucleus i is [41]

$$V_i \overset{\text{def}}{=} V(\boldsymbol{X_i}) = \cap_{j \neq i} \left\{ \boldsymbol{X} \middle| d(\boldsymbol{X_i}, \boldsymbol{X}) \leq d(\boldsymbol{X_j}, \boldsymbol{X}) \right\}, \tag{3-1}$$

where $\boldsymbol{X_i}$ are the coordinates of nucleus i; $d(\boldsymbol{X_i}, \boldsymbol{X})$ is the Euclidean distance between $\boldsymbol{X_i}$ and $\boldsymbol{X}$; and j runs from 1 to n, excluding i. This means that each point $\boldsymbol{X}$ belonging to Voronoi region i is closer to nucleus i than all other nuclei, creating a set of convex polygons in the plane as illustrated in Figure 3-2. Similarly, the boundary, or interface, segment common to two contiguous particles i and j is [41] (See Figure 3-3)

$$S_{ij} \overset{\text{def}}{=} S(\boldsymbol{X_i}, \boldsymbol{X_j}) = \cap_{k \neq i,j} \left\{ \boldsymbol{X} \middle| d(\boldsymbol{X_i}, \boldsymbol{X}) = d(\boldsymbol{X_j}, \boldsymbol{X}) \leq d(\boldsymbol{X_k}, \boldsymbol{X}) \right\}. \tag{3-2}$$

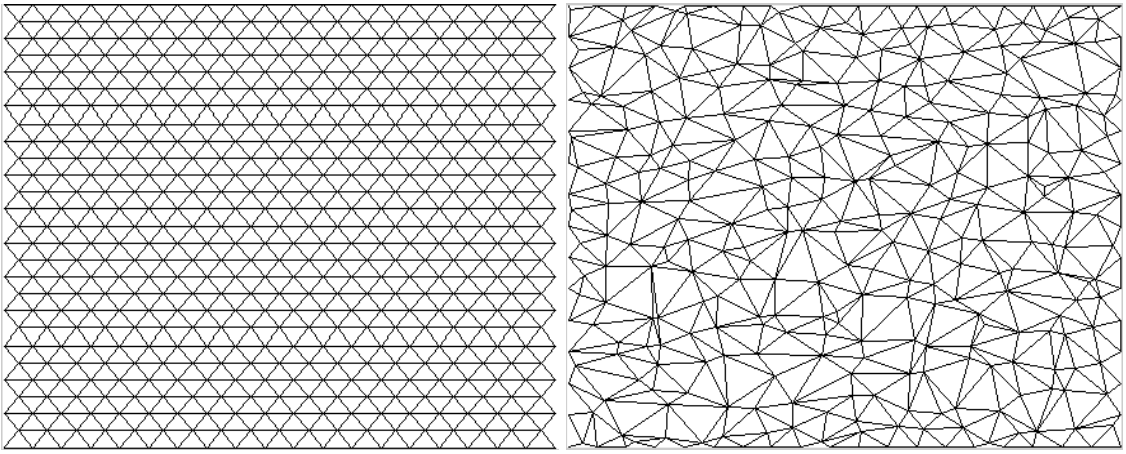

(a) *(b)*

Figure 3-2 Presentation of rectangular continuum domains in Figure 3-1 by strut bars using Voronoi diagram, a lattice model. (a) a regular mesh, (b) a random mesh.

Although Equations (3-1) and (3-2) are conceptually simple, the generation of Voronoi diagram is nontrivial due to computing demands and other issues such as the modeling of domain boundaries. Thus, special care was exercised to account for domain boundaries, both in regular and random meshes.

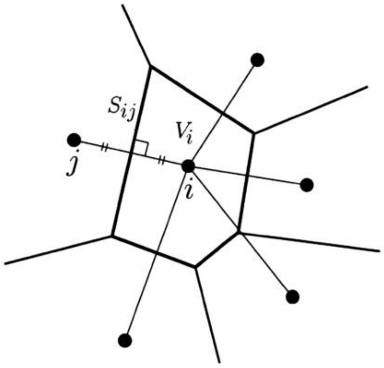

Figure 3-3 Voronoi particle associated with nucleus i. Line segment $i - j$ establishes a frame or truss element [41].

The random discretization and random mesh generation technique, Figure 3-1(b) and Figure 3-2(b), was adopted from the method firstly proposed by Mourkazel and Herrmann [43][44]. In the method, a rectangle domain, for instance, is divided to smaller rectangular grids of sizes s_x and s_y. Inside each grid cell, a point is randomly selected which itself lies inside a smaller rectangular cell of sizes A_x and A_y such that $A_x \leq s_x$ and $A_y \leq s_y$ (Figure 3-4). The ratios $0 \leq A_x/s_x \leq 1$ and $0 \leq A_y/s_y \leq 1$ determine the degree of randomness, D.O.R., of the mesh along $x - axis$ and $y - axis$, respectively, where $DOR = 1$ when there is full randomness and $DOR = 0$ when there is no randomness or the mesh is regular along the specified axis. After spreading the random points or centroids over the continuum domain, the Voronoi tessellation is used to discretize the domain according to the random point set and then to connect them. These connecting lines are the struts or frame elements of the lattice mesh as explained earlier.

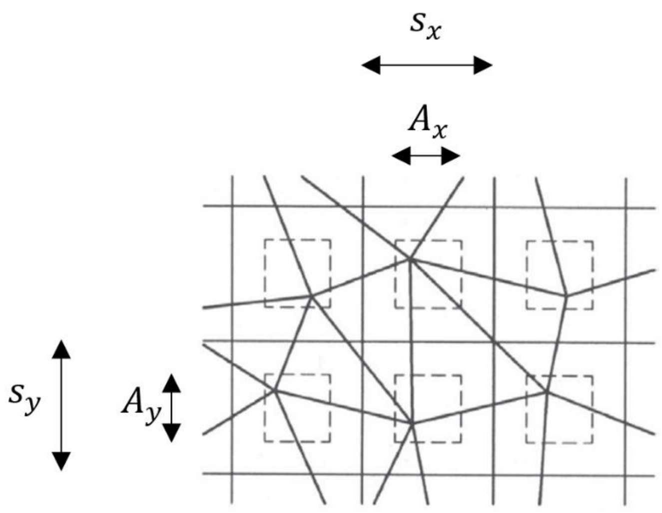

Figure 3-4 Random mesh generation technique based on a regular square grid [43], [44].

Figure 3-5 illustrates some lattice meshes generated by the above mentioned technique. Figure 3-5(a) to Figure 3-5(d) show meshes with $DOR = 0$, $DOR = 0.2$, $DOR = 0.6$, and $DOR = 1.0$ along both x and y axes, respectively. This degree of randomness may be different along the vertical and horizontal axes, which is suitable for generating random meshes for layered heterogeneous media like masonry composites.

3.2 Material Structure Overlay

One of the attractions of lattice models is the combination of the mechanics model and the material structure, called material structure overlay. The lattice is the mechanical model; the material structure is simply projected on top of the lattice and various properties are assigned to the lattice elements depending on their specific location in the projected material structure. In other words, the lattice and material structure are two independent features of the model. Figure 3-6 illustrates the material properties' assignment to the mechanical model. 'Black', 'blue', and 'pink' struts in Figure 3-6 represent elements on which the material properties of brick, mortar and interface are projected, respectively. The coordinates of each strut's nodes are firstly considered, having three phases of material properties. If both nodes of an element fall within a single phase, then that phase's material properties are assigned to that of the element. This is valid for the brick and mortar phases. However, if one node is located on one phase and the other node sits on another phase, then that element is considered as an interface receiving material properties of interface element.

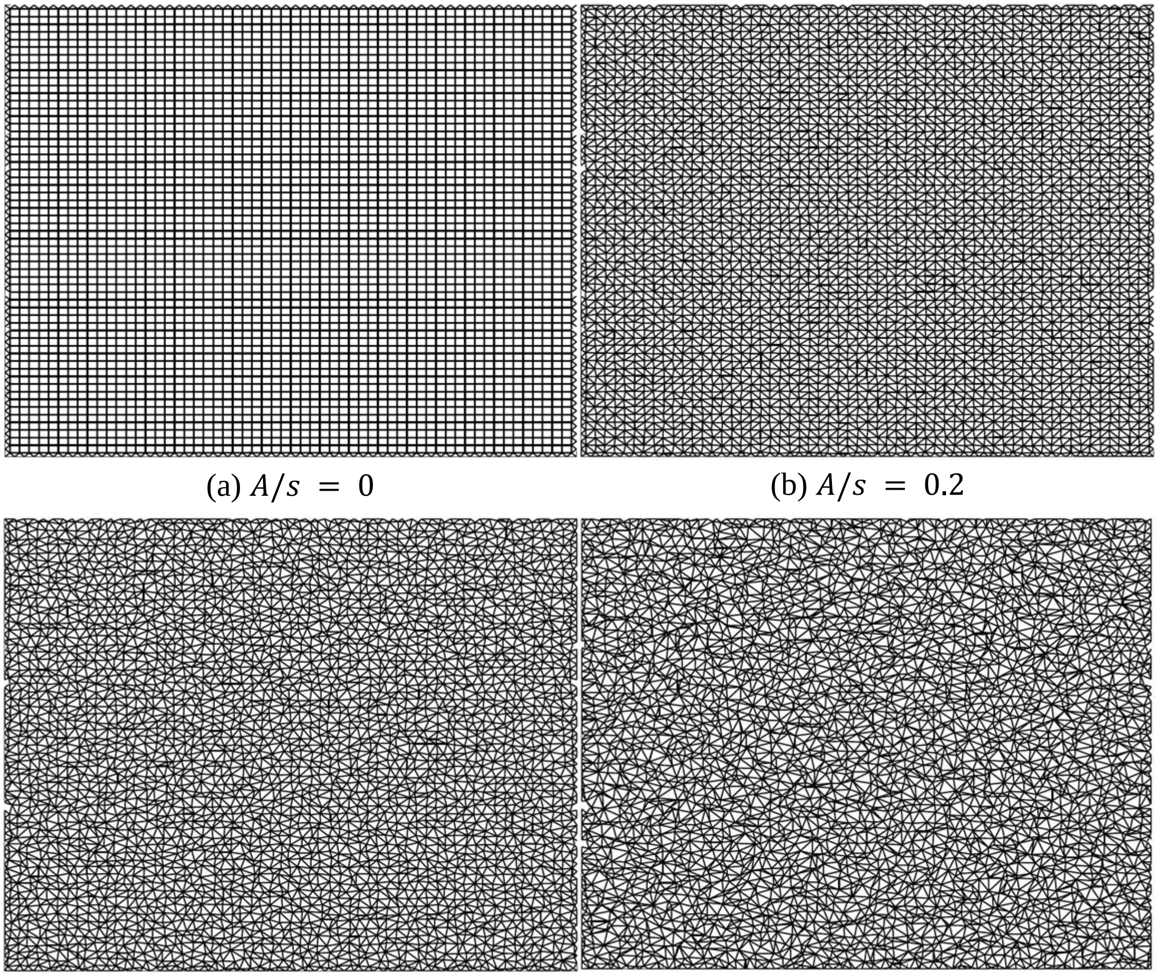

(a) $A/s = 0$ (b) $A/s = 0.2$

(c) $A/s = 0.6$ (d) $A/s = 1.0$

Figure 3-5 Different lattice meshes with four degrees of randomness.

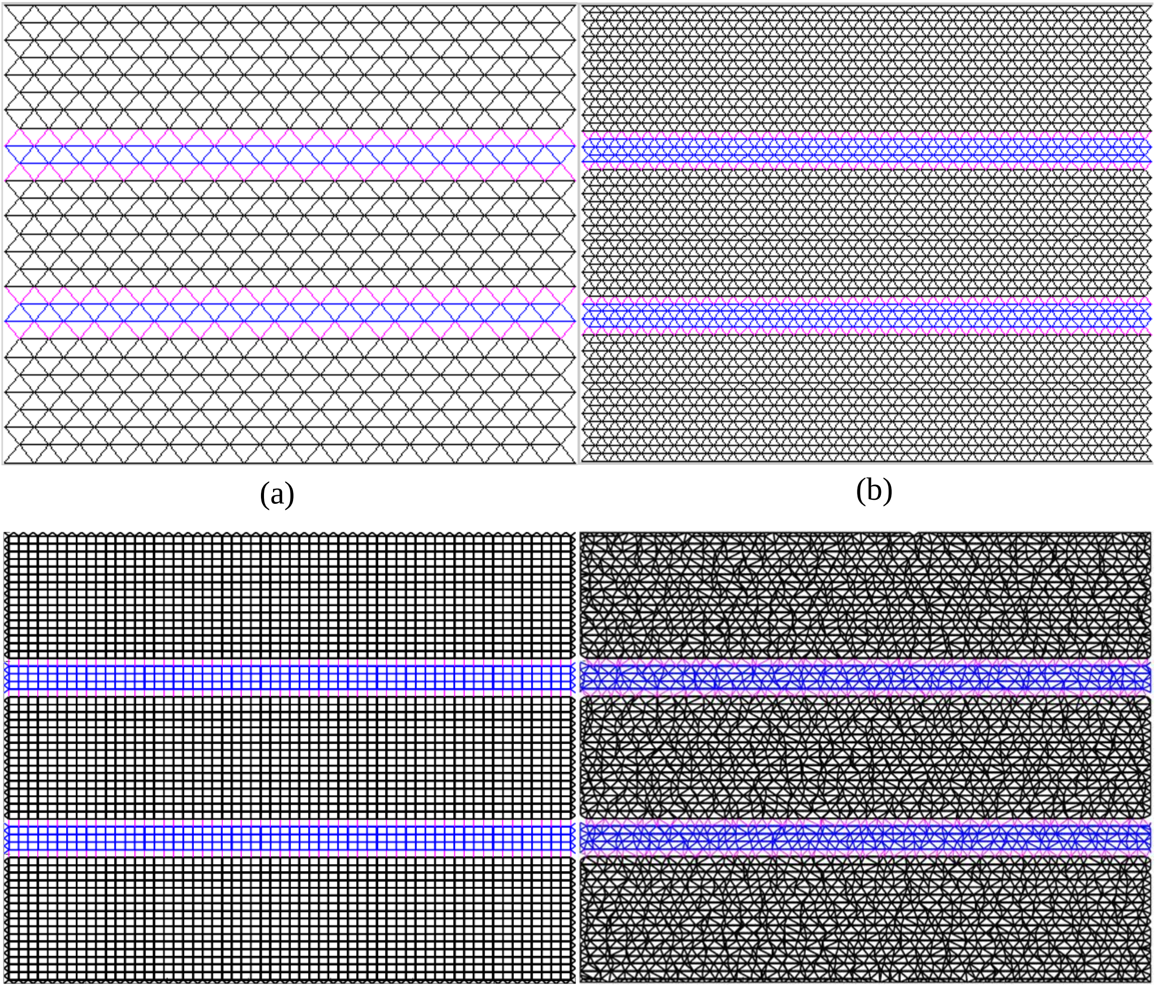

(a) (b)

(c) (d)

Figure 3-6 Overlaying material properties onto lattice structure. Black, blue and pink represent brick, mortar, and interface material properties, respectively.

Figure 3-6(a) and Figure 3-6(b) shows two coarser and finer regular triangular meshes with the overlaid material properties. In Figure 3-6(c), $DOR = 0$ in both directions, resulting in a regular square mesh; while $DOR_x = 1$ and $DOR_y = 0$ in Figure 3-6(d) to produce a layered random mesh having three material phases.

The connecting lines between the nodes in the lattice mesh represent the truss or frame elements which are the mechanical model of the numerical lattice simulation. Number of degrees of freedom at nodes or computational points determine the type of element in the simulation. In this study, 2-D ‘frame’ elements with three degrees of freedom at nodes were considered. In fact, the number of DOFs determines the type of continuum that the lattice represents. The lattice of frame elements is a discretization of a higher order continuum, i.e., a Cosserat (micro polar) elastic continuum [45]. Schlangen and Garboczi [45] evaluated three types of elements, i.e., trusses with 1, 2, and frames with 3 degrees of freedom at each node. They concluded that in the simulations with frame elements, the crack pattern on the mesh was much closer to the experimentally obtained cracks. de Borst and Muehlhaus [46] also showed that using a Cosserat continuum will in many cases result in more physically realistic crack patterns in continuum models. They concluded that the micro polar model is capable of properly describing discontinuities that arise at a micro level in the material. J. van Mier [44] also recommended frame elements as they can be fitted over a wider range to match the elastic constants of uncracked concrete. When using truss elements in fracture simulations, the lattice may become ‘unstable’ when too many struts are removed. This was confirmed for the lattice simulations of the triplet test of double lap shear in this study for regular triangular meshes when the stiffness matrix became singular after removing a set of diagonal struts at the interface layer.

3.3 Lattice Constitutive Relation

2-D frame elements with three degrees of freedom were considered for the numerical lattice simulations in this study. As shown in Figure 3-7, each frame strut can transfer, in general, normal force N, shear force Q, and bending moment M, due to their corresponding degrees of freedom.

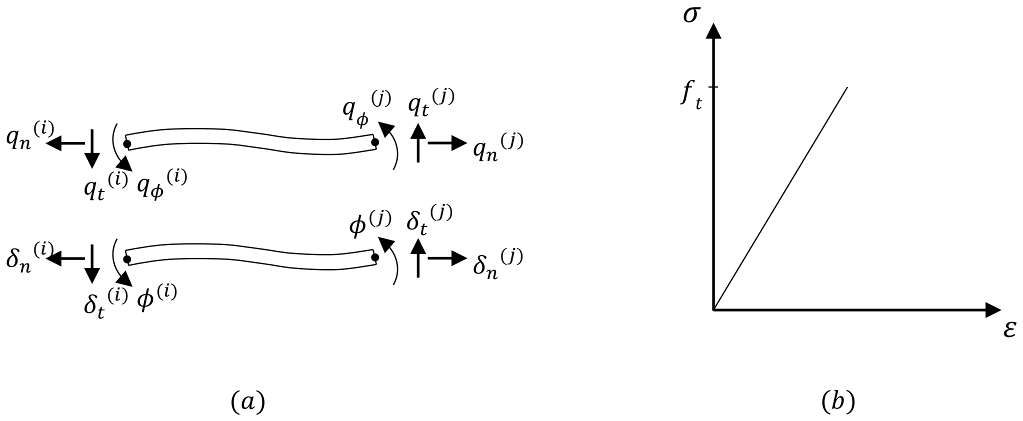

(a) (b)

Figure 3-7 (a) Degrees of freedom and external forces acting on a 2D frame element in local coordinates; (b) Constitutive relation for a single frame element

The relation between these forces and their corresponding displacements at the endpoints of the frame element, Figure 3-7(a), can be expressed by the well-known 2D relation [45]

$$\boldsymbol{q} = \boldsymbol{S}\boldsymbol{d} \tag{3-3}$$

or

$$\begin{Bmatrix} q_n{}^{(i)} \\ q_t{}^{(i)} \\ q_\phi{}^{(i)} \\ q_n{}^{(j)} \\ q_t{}^{(j)} \\ q_\phi{}^{(j)} \end{Bmatrix} = \begin{bmatrix} \frac{EA}{h_0} & 0 & 0 & -\frac{EA}{h_0} & 0 & 0 \\ 0 & \frac{12EI}{h_0{}^3} & -\frac{6EI}{h_0{}^2} & 0 & -\frac{12EI}{h_0{}^3} & -\frac{6EI}{h_0{}^2} \\ 0 & -\frac{6EI}{h_0{}^2} & \frac{4EI}{h_0} & 0 & \frac{6EI}{h_0{}^2} & \frac{2EI}{h_0} \\ -\frac{EA}{h_0} & 0 & 0 & \frac{EA}{h_0} & 0 & 0 \\ 0 & -\frac{12EI}{h_0{}^3} & \frac{6EI}{h_0{}^2} & 0 & \frac{12EI}{h_0{}^3} & \frac{6EI}{h_0{}^2} \\ 0 & -\frac{6EI}{h_0{}^2} & \frac{2EI}{h_0} & 0 & \frac{6EI}{h_0{}^2} & \frac{4EI}{h_0} \end{bmatrix} \begin{Bmatrix} \delta_n{}^{(i)} \\ \delta_t{}^{(i)} \\ \phi^{(i)} \\ \delta_n{}^{(j)} \\ \delta_t{}^{(j)} \\ \phi^{(j)} \end{Bmatrix}, \tag{3-4}$$

in which E is the Young's modulus, A is the cross-sectional area, h_0 is the length, I is the moment of inertia, δ_n and δ_t are the translational displacements, and ϕ is the rotational displacement of a frame element. The force vector $\boldsymbol{q}$ in Equation (3-3) is in local coordinate system. To establish the system of equations for the whole lattice mesh, the force vector $\boldsymbol{q}$ in Equations (3-3) and (3-4) must be multiplied by the appropriate transformation matrix as

$$\boldsymbol{f_e} = \boldsymbol{Tq}\,, \tag{3-5}$$

where $\boldsymbol{f_e}$ is force vector in the lattice global $x - y$ coordinates for the frame element e, $\boldsymbol{T}$ is the transformation matrix from the local to the global coordinate system defined by

$$\boldsymbol{T} = \begin{bmatrix} \cos(\theta) & -\sin(\theta) & 0 & 0 & 0 & 0 \\ \sin(\theta) & \cos(\theta) & 0 & 0 & 0 & 0 \\ 0 & 0 & 1 & 0 & 0 & 0 \\ 0 & 0 & 0 & \cos(\theta) & -\sin(\theta) & 0 \\ 0 & 0 & 0 & \sin(\theta) & \cos(\theta) & 0 \\ 0 & 0 & 0 & 0 & 0 & 1 \end{bmatrix}, \tag{3-6}$$

in which θ is the angle measured counterclockwise from the positive direction of the global x axis to the positive direction of the local x axis.

Equation (3-4) is a well-known force-displacement relationship for 2D frame elements in the lattice model. However, this equation may not be suitable if a zero-thickness interface element with a traction-separation constitutive relation needs to be projected onto the lattice mesh. In this study, an approach introduced by Bolander and Saito [41] was employed to establish the constitutive relation of brick, mortar, and interface in a 2D plane strain or plane stress lattice simulation.

Figure 3-8 shows the relationship of two Voronoi particles by putting a flexible interface between them. The interface or boundary defined in Equation (3-2) is shown in Figure 3-3. In Figure 3-8, two triangular particles are connected at their interfaces by translational and rotational stiffnesses, i.e., k_n, k_t, and k_φ, which approximate the elastic properties of the continuum. Points 1 and 2 in this figure are the nuclei or computational points lying at the beginning and end points of the strut or frame element. The relation between internal forces and local displacements is [41]

$$\boldsymbol{q} = \boldsymbol{D}\boldsymbol{d}, \tag{3-7}$$

where $\boldsymbol{q^t} = \{q_n, q_t, q_\phi\}$ is the internal force vector between two particles; $\boldsymbol{D}$ is a diagonal matrix containing the normal, tangential, and rotational spring stiffnesses depicted in Figure 3-8(a), i.e., $\boldsymbol{D} = diag[k_n,\ \ k_t,\ \ k_\phi]$; $\boldsymbol{d}^t = \{\delta_n, \delta_t, \phi\}$ is the local relative displacement vector of two particles in the normal, tangential, and rotational directions, Figure 3-8(b), and the superscript t denotes the transpose of a vector.

The spring stiffnesses are obtained in terms of elastic properties of the continuum domain and also the geometry of the connected particles. For brick and mortar frame elements, the stiffnesses are obtained as follows:

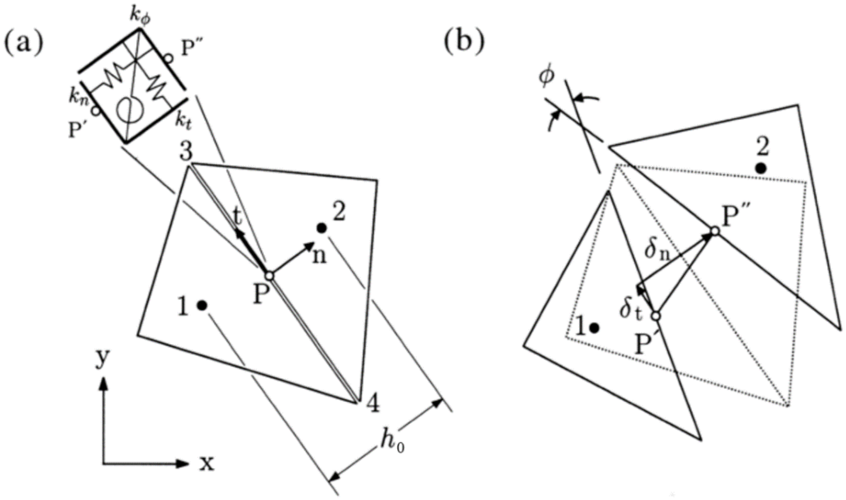

Figure 3-8 Mechanical relationship between two particles. (a) Embedding translational and rotational stiffness between two particles on the interface, (b) facet local displacement in t-n coordinates [41].

$$k_n = \frac{E'A}{h_0} = \frac{E' t l_{43}}{h_0}, \tag{3-8}$$

$$k_t = \frac{E''A}{h_0} = \frac{E'' t l_{43}}{h_0}, \text{ and} \tag{3-9}$$

$$k_\phi = \frac{E'I}{h_0} = \frac{E'}{h_0}\left(\frac{t {l_{43}}^3}{12}\right) = \frac{E'(t \times l_{43})}{h_0}\left(\frac{{l_{43}}^2}{12}\right) = \frac{E'(A)}{h_0}\left(\frac{{l_{43}}^2}{12}\right) = \frac{k_n {l_{43}}^2}{12}, \tag{3-10}$$

where, $E' = E/(1-\nu^2)$ and $E'' = \mu = E/[2(1+\nu)]$ for plane stress; $E' = E(1-\nu)/[(1+\nu)(1-2\nu)]$ and $E'' = \mu = E/[2(1+\nu)]$ for plane strain; E and ν are the Young's modulus and Poisson ratio of the continuum material, respectively; t is the specimen thickness; h_0 is the frame element length between points 1 and 2, as shown in Figure 3-8(a); l_{43} is the frame element width between points 3 and 4 in Figure 3-8(a); and $A = t l_{43}$ is the cross sectional area. For the interface elements, $k_n = K_n A$, $k_t = K_t A$, and $k_\phi = 0$, similar to truss elements with no rotational stiffnesses. K_n and K_t are obtained by homogenizing the composite material surrounding the interface, i.e., brick and mortar [13] as

$$K_n = \frac{E_b E_m}{h_b h_m \left({}^{E_b}/_{h_b} + {}^{E_m}/_{h_m}\right)} \text{ and} \tag{3-11}$$

$$K_t = \frac{\mu_b \mu_m}{h_b h_m \left({}^{\mu_b}/_{h_b} + {}^{\mu_m}/_{h_m}\right)}, \tag{3-12}$$

where E_b, μ_b and E_m, μ_m are the normal and shear moduli of the brick and mortar, respectively. Equations (3-11) and (3-12) can be obtained by considering a serial arrangement of brick-interface-mortar where the volume change is negligible.

The stiffness matrix in global $x - y$ coordinates associated with the two-particle assemblage follows from matrix analysis of structures as

$$\boldsymbol{k_e} = \boldsymbol{B^t D B}, \tag{3-13}$$

where matrix $\boldsymbol{B}$ relates the displacement vector in local $t - n$ coordinates, i.e., $\boldsymbol{d}$, to that in global $x - y$ coordinates, i.e., ${\boldsymbol{u_e}}^t = \{u_1, v_1, \theta_1, u_2, v_2, \theta_2\}$ as [41]

$$\boldsymbol{d} = \boldsymbol{B u_e} =$$

$$\frac{1}{l_{43}} \begin{bmatrix} y_{43} & -x_{43} & (-x_{43}x_{P1} - y_{43}y_{P1}) & -y_{43} & x_{43} & (x_{43}x_{P2} + y_{43}y_{P2}) \\ x_{43} & y_{43} & (y_{43}x_{P1} - x_{43}y_{P1}) & -x_{43} & -y_{43} & (-y_{43}x_{P2} + x_{43}y_{P2}) \\ 0 & 0 & -l_{43} & 0 & 0 & l_{43} \end{bmatrix} \begin{Bmatrix} u_1 \\ v_1 \\ \theta_1 \\ u_2 \\ v_2 \\ \theta_2 \end{Bmatrix}, \tag{3-14}$$

where point P is the facet midpoint in Figure 3-8 and $x_{ij} = x_i - x_j$, $y_{ij} = y_i - y_j$, i.e.,

$$\begin{cases} x_{Pi} = (x_{4i} + x_{3i})/2 \\ y_{Pi} = (y_{4i} + y_{3i})/2 \end{cases} \quad i = 1,2. \tag{3-15}$$

Moreover,

$$\boldsymbol{k_e u_e} = \boldsymbol{f_e}, \tag{3-16}$$

in which $\boldsymbol{f_e}$ contains the force components in global coordinates for the frame element associated with each respective entry in displacement vector $\boldsymbol{u_e}$. The frame element stiffness matrix $\boldsymbol{k_e}$ in Equation (3-13) is assembled in a conventional manner to form the global stiffness matrix of the whole lattice mesh. It should be noted that the particle's geometries are used as entries of $\boldsymbol{D}$ and $\boldsymbol{B}$, as indicated by Equations (3-8) to (3-15). Also, the constitutive relation and stiffness formulation do not have inter-particle contact modeling, like the one used in the distinct element method [47].

3.4 Lattice Fracture Criteria

The simulation of fracture, in this study, was performed with a 'linear elastic' analysis of the lattice under loading, Figure 3-7(b), and removing an element from the mesh which exceeds a certain fracture criterion, for instance a tensile or compressive stress based on the failure envelope. The 'gap' between the remaining elements is considered as a discontinuity or crack in the lattice mesh. After removing the element, the lattice mesh contains one less element. The simulation is continued by performing a linear elastic analysis of the new mesh, where the forces that were carried by the removed element are now redistributed over the neighboring elements. This procedure continues until the next element satisfies its 'fracture criterion', and so on [45], [44]. Thus at each step, the external load on the lattice is increased and the critical element at the fracture threshold is removed. The erosion strategy leads to an 'instantaneous relaxation' of the load, carried by that removed part of the lattice [44]. This was often observed during the lattice analyses of this study as a sudden drop in form of snap-backs in the load-displacement diagrams. Figure 3-9 illustrates a test simulation of a masonry prism in direct tension, the load-displacement curve of which involves snap-back instabilities which are due to the failure of the lowest interface struts. The saw-tooth pattern observed at the post-peak part of the curve is because of the failure of each strut in an unzipping manner, releasing fracture surface energy which exhibits itself in the form of displacement relaxations of the lattice mesh.

Fracture criterion for the failure of brick and mortar frame elements, i.e., "black" and "blue" struts in Figure 3-9, was defined as a function of normal force and bending moments at computational points of each frame member as

$$\sigma_{eff} = \frac{N}{A} \pm \alpha' \frac{(|M_i|,|M_j|)_{max}}{S} \geq f_t \; or \; f_c, \tag{3-17}$$

where N is the normal force of the lattice element; A is its cross sectional area; M_i and M_j are the bending moments at the nodes i and j, respectively; $S = l_{43}t^2/6$ is the section modulus; f_t and f_c are the tensile and compressive strengths of the material, respectively; and $0 \leq \alpha' \leq 1$ is added to limit the effect of bending in the fracture law. The value of α' may be determined by parametric studies and comparison with experimental measurements [48].

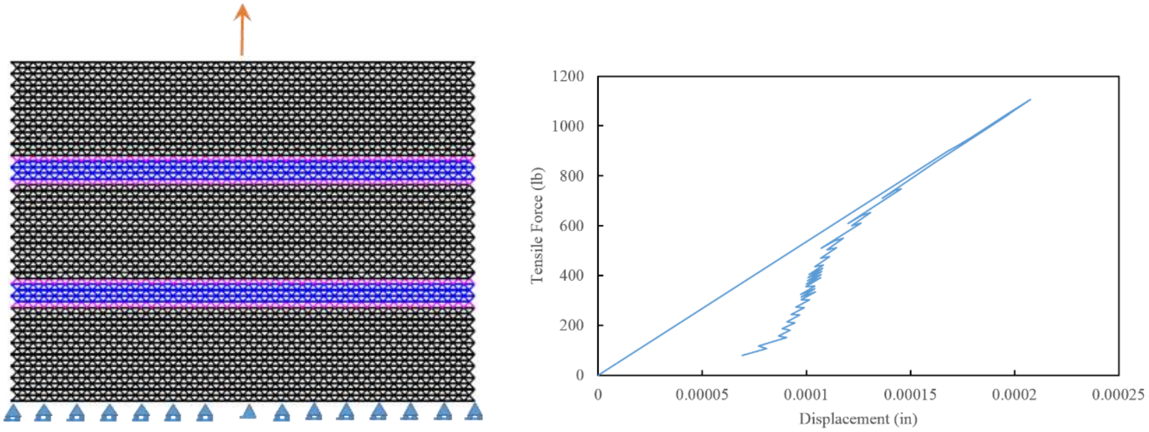

(a) (b)

Figure 3-9 (a) Direct tensile test on a regular triangular lattice with interfaces; (b) Tensile load versus vertical displacement of top nodes

The fracture criterion for the brick-mortar interface was determined based on a combination of experimental measurements and numerical parameter simulations. Figure 3-10 shows the fracture condition considered for the interface frame elements in the lattice model. This failure envelope has a compressive cap which was necessary for the simulation of triplet test under high normal confinements. It should be noted that the shear failure surfaces were neglected for brick and mortar elements since the main focus of this study was to evaluate the brick-mortar interface fracture properties, and with the simulations conducted, their shear failure envelopes were not activated.

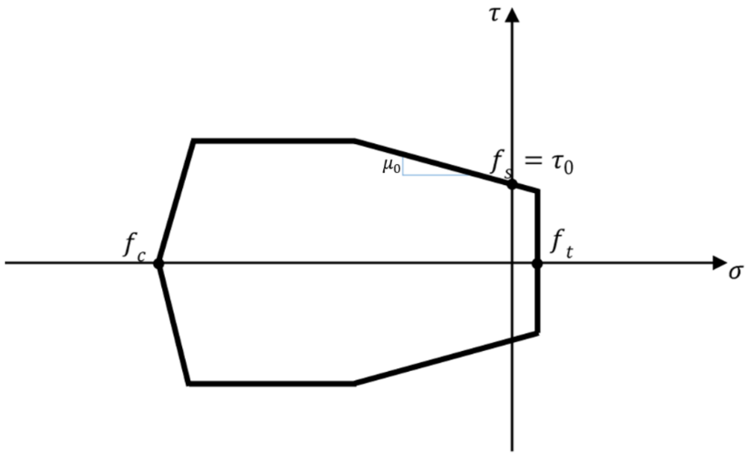

Figure 3-10 Failure surface for the brick-mortar interface employed in this study.

In this figure, the failure surface has three major parts, namely a tension cut-off, a Coulomb shear envelope, and a compressive cap. The tension cut-off part was determined based on the direct tension test of interface, Section 2.2.3.1, while the inclined shear envelope was obtained by the triplet experiments mentioned in Section 2.2.3.2. The horizontal part of the shear envelope in Figure 3-10 and also the compressive cap were determined by parametric studies of confined triplet simulations under different high confinements in the implemented lattice model. Strength parameters of brick, mortar and interface has been presented in Table 3-1.

Table 3-1 Mechanical characteristics of materials adopted for the computations

	E (lbf/in^2) [MPa]	ν	f_t (lbf/in^2) [MPa]	f_c (lbf/in^2) [MPa]		
Brick	4506000 [31067.78]	0.1	400 [2.76]	6000 [41.37]		
Mortar	3022000 [20835.96]	0.2	300 [2.07]	2000 [13.79]		
	K_n (lbf/in^3) [N/mm^3]	**K_t (lbf/in^3) [N/mm^3]**	**f_t (lbf/in^2) [MPa]**	**f_c (lbf/in^2) [MPa]**	**f_s (lbf/in^2) [MPa]**	**μ_0**
Interface	1504240 [408.32]	668618 [181.49]	47 [0.32]	600 [4.14]	180 [1.24]	0.662

3.5 Lattice Simulations of Brick-Mortar Interface Test Configurations

The numerical implementation of the 2-D lattice model was performed in *MATLAB R2014a* [39] in the form of various developed functions. The main purpose of this implementation was to simulate the fracture behavior of brick-mortar interface under different loading conditions, as presented in Section 2.2.3. These loading conditions involve tension, shear, and combined shear and compression. In this section, only the global behavior of these masonry test specimens in the form of deformed meshes and load-displacement curves is evaluated. The interface fracture properties like the energy release rate and stress intensity factors and their simulations will be discussed in the following chapters.

3.5.1 Interface behavior in direct tension simulation

A direct tension test was simulated using a regular lattice model on a prism made of three bricks, two mortar joints, and four interface layers as shown in Figure 3-11. We name the interfaces from bottom side of the specimen as interfaces 1, 2, 3, and 4, respectively. The height, and length of each brick are about 2 and 6 inches, respectively.

The height for the mortar joint is almost $0.5\ (in)$. The thickness of the specimen is $4\ (in)$. The height of each interface would decrease as the mesh is more refined. The failure should happen through the brick-mortar interface.

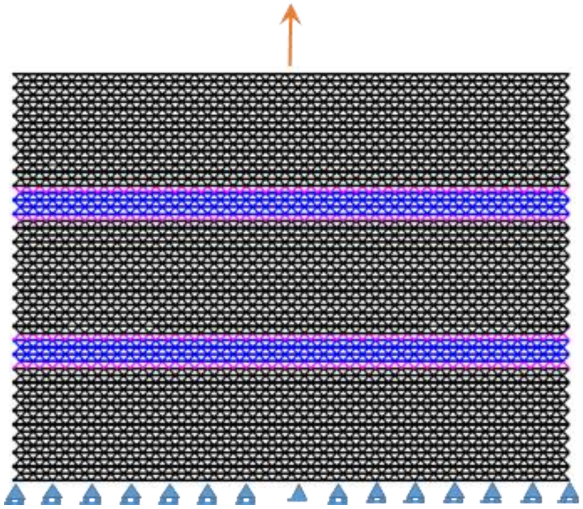

Figure 3-11 Direct tensile test on a regular lattice model with interfaces.

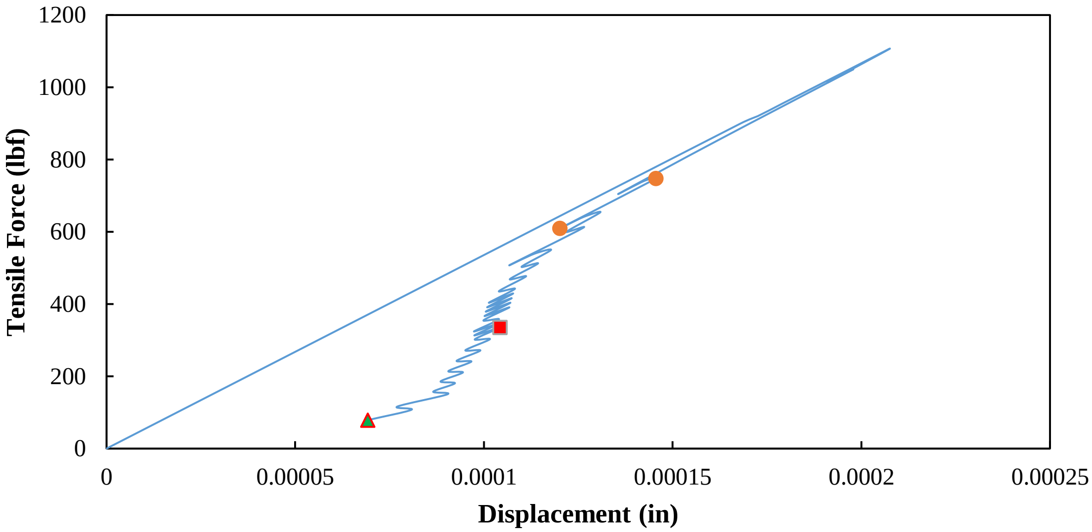

Figure 3-12 Tensile load versus vertical displacement of top nodes for the masonry prism with regular lattice mesh shown in Figure 3-11.

Figure 3-12 shows the load-displacement curve for the direct tensile test shown in Figure 3-11. The simulation was run in displacement control with a constraint that limits the number of failed struts at each increment. This constraint reduces the displacement values at the free degrees of freedom where the traction is applied. This reduction in applied displacements introduces snap-backs on the load-displacement diagram. As it can be seen, the post-peak behavior exhibits snap-back instabilities. Not only does it need a precise and delicate experiment program to capture snap-backs during a test in laboratory, but also it is challenging enough to trace the equilibrium path through a continuum FE model even if an equilibrium solution algorithm like Arc-Length is utilized. This could be considered as one of the advantages of the lattice modeling in presenting the load-displacement curve.

Figure 3-13 illustrates the second interface crack propagation at different load increments, i.e., the four points on the load-displacement curve. The failure starts from the lateral sides of the interface layer sweeping to the center of the specimen. Two top deformed meshes in this figure correspond to the two orange points in Figure 3-12, as the sudden drop in the load-displacement curve from $748\ (lbf)$ to $609\ (lbf)$ is due to the failure of two more frame elements in the top left mesh leading to the top right mesh with a total of 12 failed struts. This indicates the relation between localized fracture processes and snap-back instabilities. The bottom left mesh is related to the square point in Figure 3-12 at a load level of $335\ (lbf)$. The bottom right mesh also corresponds to the triangular point in the curve where the load level was dropped to $79\ (lbf)$ and almost all the interface struts were already swept away. Looking at Figure 3-12 and Figure 3-13, it is observed that a considerable amount of stain energy is released and dissipated due to the failure of the first 10 interface elements in the lattice mesh. It should also be mentioned that red colored struts at these deformed meshes indicate that the interface element is under tension with an internal tensile force greater than 65% of its tensile strength capacity and is going to touch the tension cut off line as shown in Figure 3-10.

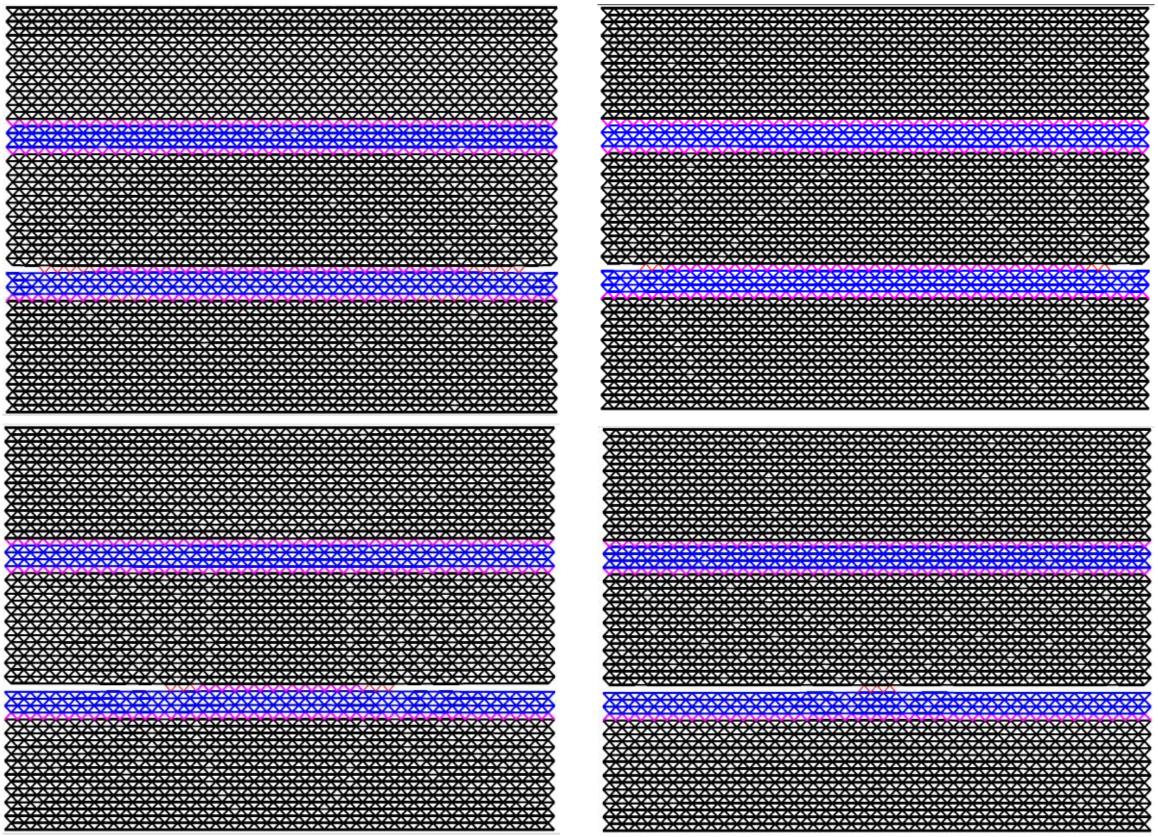

Figure 3-13 Interface fracture propagation for the direct tensile test happening at interface 2, from top left to bottom right, corresponding to the four highlighted points in Figure 3-12 (Deformations have been magnified by 300).

Another direct tension test was simulated on the same specimen with a randomly-generated lattice mesh as depicted in Figure 3-14 and Figure 3-15. The four points in Figure 3-14 from the load level of $963\ (lbf)$ down to $45\ (lbf)$ correspond to the meshes in Figure 3-15 from top left to the bottom right, respectively. In this case, failure initiates from the left side of the interface 3 due to its random nature of struts geometry. The peak load in the random lattice is $963\ (lbf)$, or $40.8\ (psi)$, compared to $1107\ (lbf)$, or $46.9\ (psi)$, for the regular lattice.

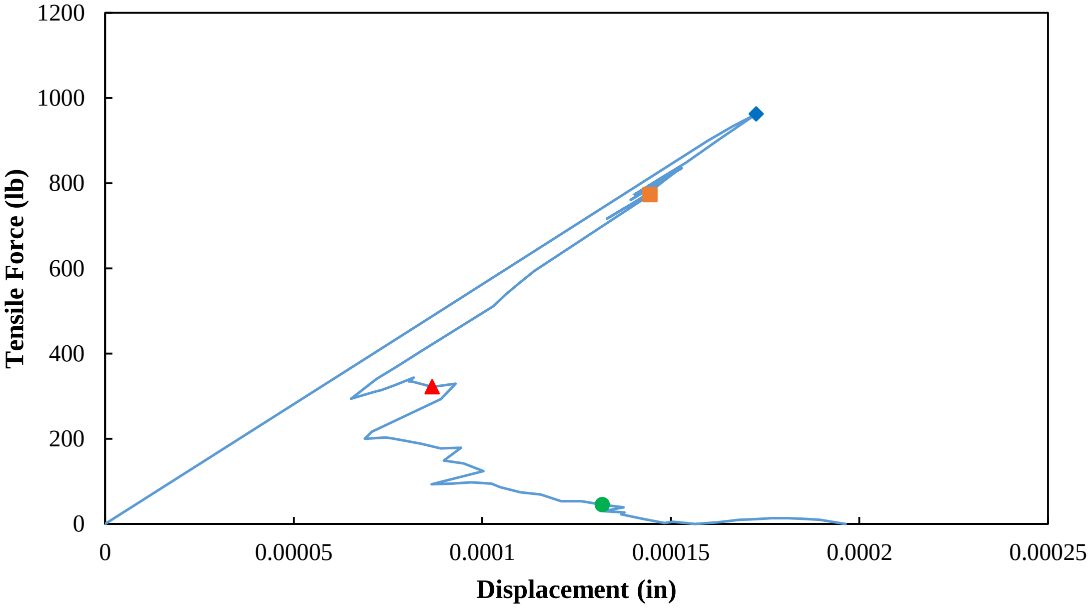

Figure 3-14 Tensile load versus vertical displacement of top nodes for the masonry prism with 'random' lattice mesh.

These stresses correspond to the tensile strength of the interface element which was $47\ (psi)$ as an input into the numerical model. Therefore, the regular triangular lattice model can better predict the peak load than the random lattice mesh. This was tested even for a finer random lattice mesh and the peak load went down from $963\ (lbf)$ to $926\ (lbf)$. This trend is also true for the regular square mesh with $D.O.R = 0$ which is actually a random mesh with $A/s = 0$, as shown in Figure 3-5(a). By reducing the ratio A/s, the peak load decreases independent of the mesh refinement. One possible explanation might be that the internal normal forces at vertical interface struts of a regular square mesh is greater than those at the inclined struts of a triangular regular mesh.

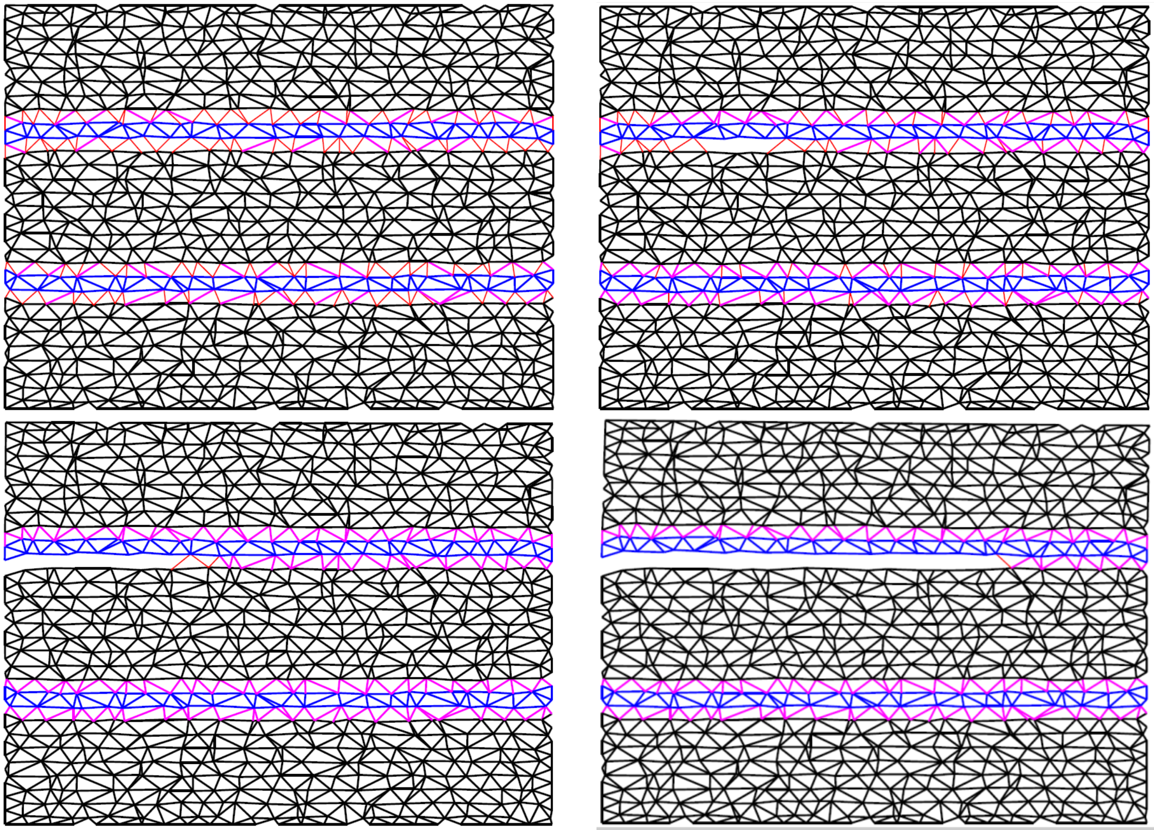

Figure 3-15 Interface fracture propagation for the direct tensile test happening at interface 3 for a random mesh, from top left to bottom right, corresponding to the four highlighted points in Figure 3-14(Deformations have been magnified by 300).

3.5.2 Interface behavior in triplet test simulations

Some lattice simulations have been conducted for the triplet test for situations where there is no normal confinement and also cases in which confined normal load is applied.

3.5.2.1 Unconfined triplet simulation

The same masonry composite as shown in Figure 3-11 was considered here with a different loading and boundary conditions shown in Figure 3-16. The shear load is applied on the middle brick at the right end while two other bricks are supported at the left end. Figure 3-17 illustrates the load-displacement curve for the unconfined triplet lattice model shown in Figure 3-16. Due to the beam removal strategy in the lattice model, after removing one or two frame elements the load is redistributed over neighboring struts and at some points a portion of strain energy is 'released' leading to snap-back instabilities in the load-displacement curve.

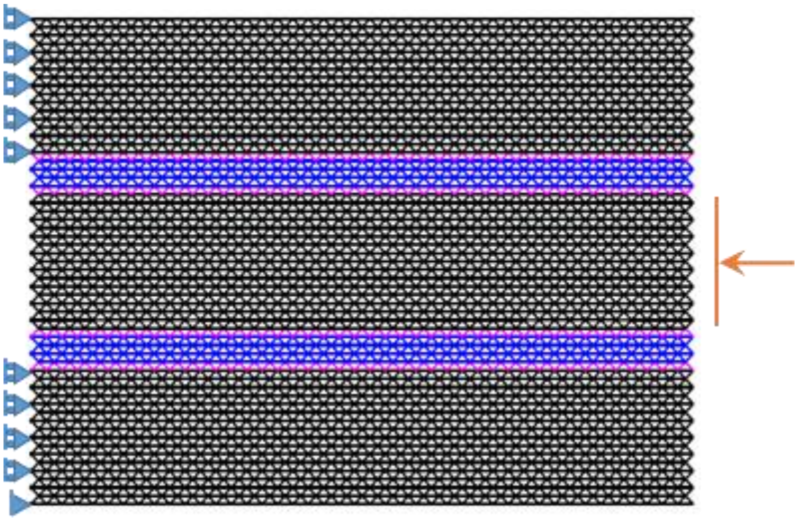

Figure 3-16 Unconfined triplet test simulation on a regular triangular lattice mesh.

There are four points on the curve at which the deformed mesh and interface failure progress were evaluated. Figure 3-18 is related to the four highlighted points on the load-displacement curve. This figure shows the propagation of crack on the interfaces especially interfaces 2 and 3, namely inner interfaces. There are partial and full discontinuities on the interfaces. 'Partial discontinuity' exists when just one diagonal strut element is removed at the interface layer and the other diagonal element is still in the mesh. 'Full discontinuity' is related to situations where all the struts have been removed and there is a crack on the mesh.

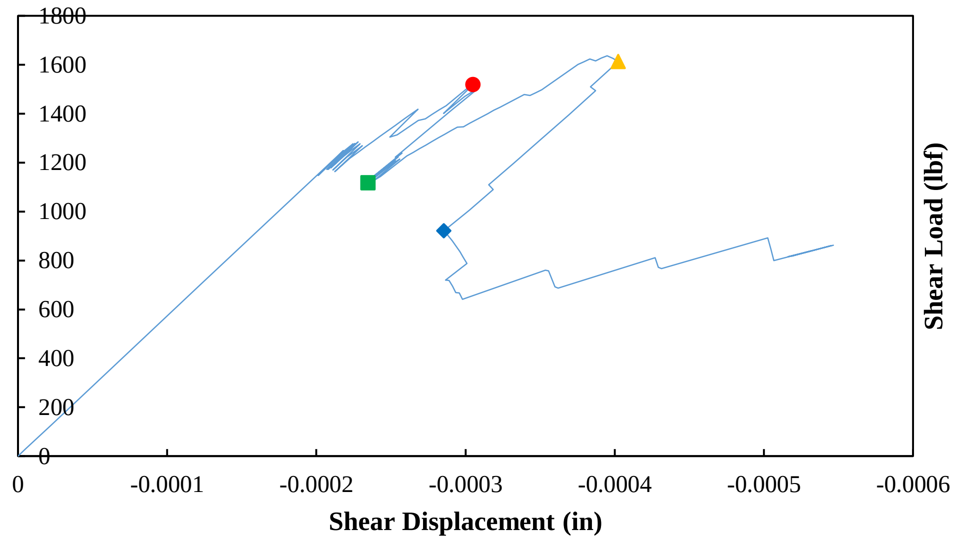

Figure 3-17 Shear load versus horizontal shear displacement of the unconfined triplet simulation for the regular lattice mesh shown in Figure 3-16.

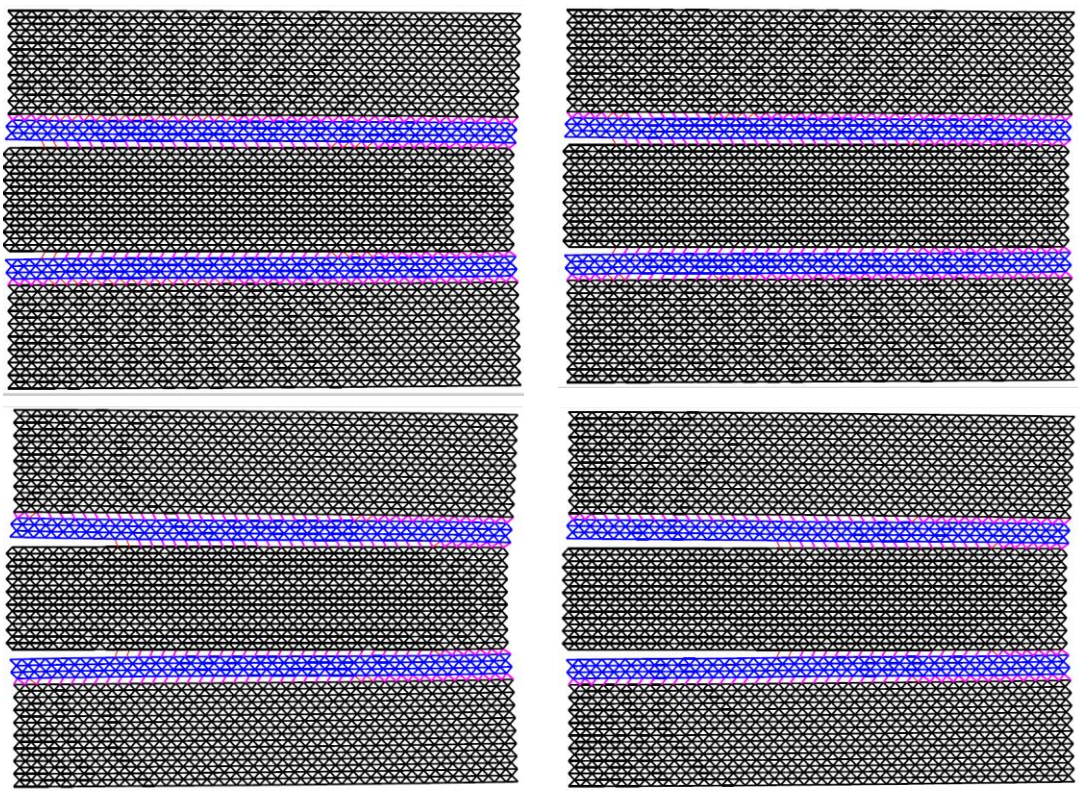

Figure 3-18 Interface fracture propagation for the unconfined triplet test simulation from top left to bottom right, corresponding to the four highlighted points in Figure 3-17 (Deformations have been magnified by 300).

It is seen, in Figure 3-18, that the failure of interface elements starts from the left end rather than right end which might be due to the boundary conditions on the left end of the outer bricks and the direction of shear loading. Moreover, since the middle brick moves along the horizontal direction while two others are supported at the left end, inner interfaces, i.e., 2 and 3, encounter more fractures than the outer ones. Full discontinuity or cracking is only observed at the inner interfaces starting at the left end. Outer interfaces only experience partial discontinuities.

Bottom left and bottom right meshes in Figure 3-18 correspond to the yellow triangular and blue square points in Figure 3-17, respectively. According to the load-displacement curve, there is a snap-back for these two points, which means that a considerable amount of strain energy was released between these two steps. This is especially conspicuous if the right ends of the bottom meshes are compared, as there are greater deformations at the right end of the bottom left mesh than those of the bottom right, which indicate that a portion of shear displacement and strain energy were released.

3.5.2.2 Confined triplet simulation

Another important simulation for the triplet test is related to the situations where there is a constant normal confinement while applying shear. The implementation of this confinement for the triplet test was a delicate process where considerable efforts were made. Figure 3-19 shows the same masonry prism as before with the loading and boundary conditions for the confined triplet test simulation on a regular triangular mesh. During each simulation for a specified normal confinement, its value is kept constant within an acceptable tolerance. The normal confining load is applied at the beginning of each increment and then the shear displacement is applied at the right end on the middle brick. At the next increment, the confinement is applied on the last converged displacement vector and this process continues until the loss of strength of the lattice model. Figure 3-20 shows the load-displacement curve for the confinement level of $500\ (lbf)$. Comparing load-displacement curves for Figure 3-17 and Figure 3-20, it is obvious that by applying the normal confining load, the maximum shear strength increases from about 1600 to $5300\ (lbf)$ confirming Coulomb friction law. In Figure 3-20, there are again four highlighted points related to the meshes shown in Figure 3-21.

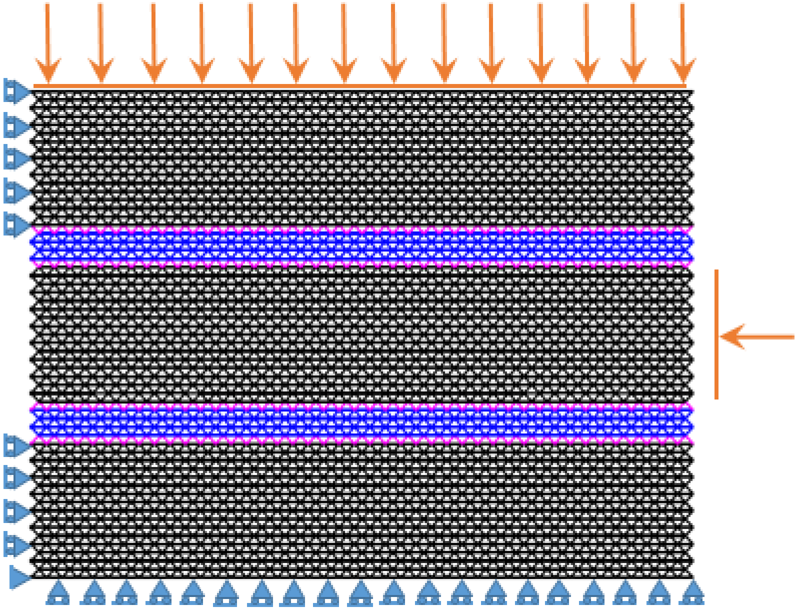

Figure 3-19 Confined triplet test simulation on a regular triangular lattice mesh.

It should be mentioned that the interface struts' color in the deformed mesh changes before failure depending on the type of failure. The failure surface of interface element with compressive cap was shown in Figure 3-10. If the strut's failure path in $\sigma - \tau$ plane is going to touch the tension cut-off line, the color would be red, while if the stress path is towards the compressive cap, the color would be green. In cases when the Coulomb friction line is touched, the color would be light blue. These color changes can be seen in Figure 3-21. For unconfined triplet simulations where there was no compressive normal confinement, almost all the struts failed under tension cut-off law, i.e., red strut, while for the confined situations, as shown in Figure 3-21, compressive cap, i.e., green, and Coulomb friction line, i.e., light blue, also played role in the failure mechanism of the interface frame elements.

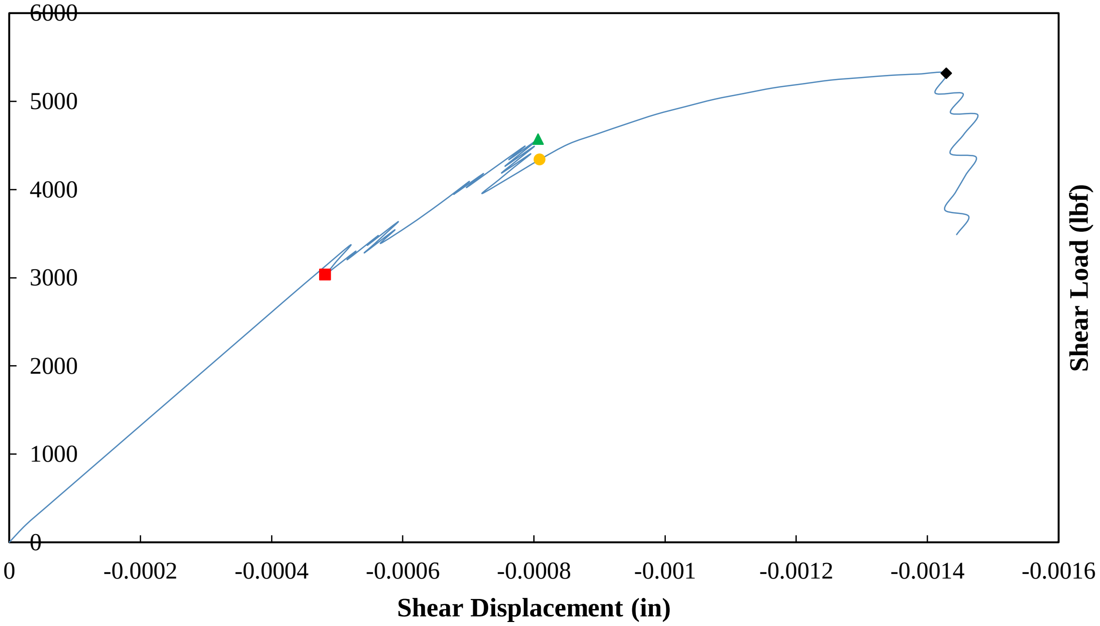

Figure 3-20 Shear load versus horizontal shear displacement of the confined triplet simulation with the confinement level of 500 (lbf) for the regular lattice mesh shown in Figure 3-19.

In Figure 3-21, the failure of interfaces does not start from the left end unlike the unconfined triplet simulation. Inner interfaces experience the partial fracture earlier than the outer ones. Up to the circular orange point in Figure 3-20, i.e., bottom left mesh, the full fracture or crack has not occurred along the interface layers. Although there are some slight strain energy recoveries in the form of snap-backs in Figure 3-20 as opposed to the considerable amount of strain energy releases in Figure 3-17, the whole load-displacement path in Figure 3-20 looks like a parabolic curve with a gradual degradation of tangent stiffness. The bottom right mesh in Figure 3-21 corresponds to the last point on the load-displacement curve with the maximum shear load.

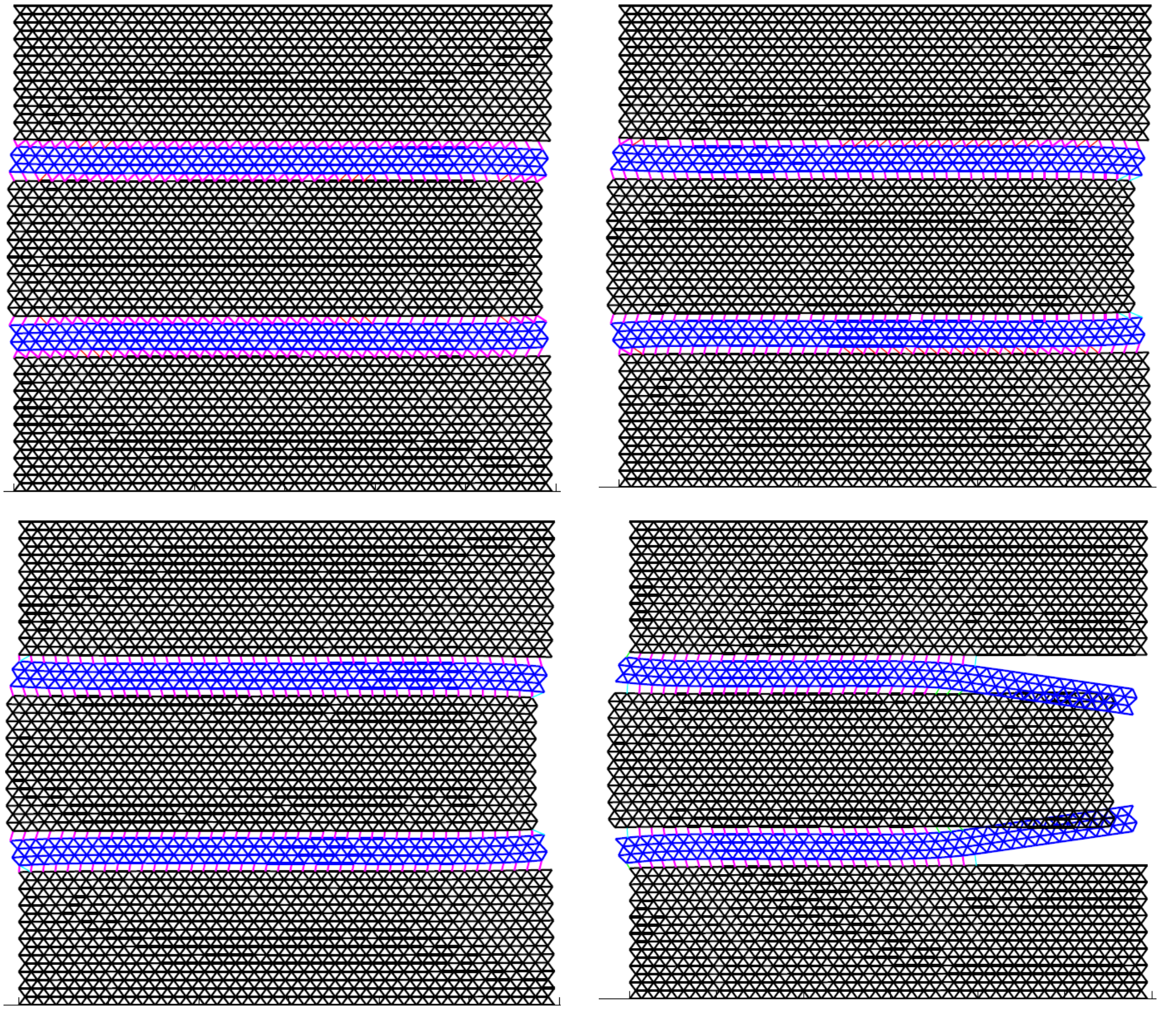

Figure 3-21 Interface fracture propagation for the confined triplet test simulation from top left to bottom right, corresponding to the four highlighted points in Figure 3-20 (Deformations have been magnified by 300). The confinement level is 500 (lbf).

The shear strength capacity of the brick-mortar interface increases with increasing the normal confinement in triplet simulations, see Equation (2-2) and Figure 2-11. The triplet lattice model in Figure 3-19 was simulated for different normal confining loads. Figure 3-22 illustrates the variation of maximum shear stress versus normal confining stress for the experimental results presented in Section 2.2.3.2 and the implemented lattice model. There is a reasonable trend of increasing shear stress for the lattice. The lattice formulation exhibits lower failure envelope than the laboratory results, which might be related to the nature of the lattice model where the continuum domain is discretized into frame elements.

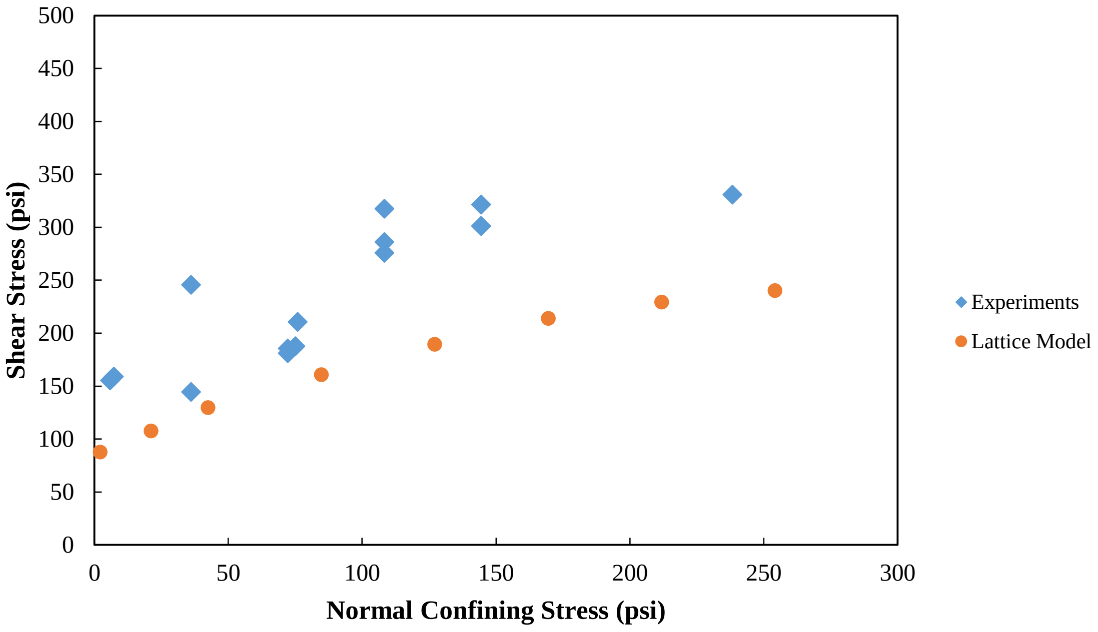

Figure 3-22 Coulomb failure envelope of the experimental results and the lattice model illustrated in Figure 3-19 for the confined triplet tests.

3.6 Summary

The first important step in using a lattice approach is to discretize the continuum domain to be analyzed. This discretization was performed in this study by using the

Voronoi diagram as was explained in Section 3.1. In this discretization, a special care should be given to the boundary regions of the lattice mesh. The lattice model is capable of generating regular square and triangular meshes besides random meshes the degree of randomness of which can vary as desired. One of the attractive features of lattice models is the material structure overlay in which the material structure is simply projected on top of the lattice and various properties are assigned to the lattice elements depending on their specific coordinates in the projected material structure. This feature was used to model layered masonry composites consisting of brick units, mortar joints, and their interface bonds. 2D frame elements with three degrees of freedom at nodes were used in the simulations of the masonry, though the model is also capable of using truss elements. As observed in other studies, using frame elements in the lattice model can better capture the crack patterns observed in experimental specimens. It was also noticed through triplet simulations that the lattice may become unstable when too many struts are removed.

In addition, instead of using conventional constitutive relation for the lattice model, an innovative approach proposed by Bolander and Saito [41] was employed which embeds flexible interfaces, having normal, tangential, and rotational springs, among the particles generated by the Voronoi diagram. This approach is especially suitable when a zero-thickness interface element with a traction-separation constitutive relation needs to be projected onto the lattice mesh.

Furthermore, the simulation of fracture was performed with a ‘linear elastic’ analysis of the lattice under loading and removing an element from the mesh which exceeds a certain fracture criterion according to the failure envelope. After removing the element, the lattice mesh contains one less element. The simulation is continued by performing a linear elastic analysis of the new mesh, where the forces that were carried by the removed element are now redistributed over the neighboring elements. This procedure continues until the next element satisfies its fracture criterion. The erosion strategy leads to an ‘instantaneous relaxation’ of the load resulting in a sudden drop in form of snap-backs in the load-displacement diagrams. A tension cut-off and compression cap were considered for the fracture law of the brick and mortar; while that of the interface struts involved a Coulomb shear envelope in addition to the tension-cut off and compressive cap.

Numerical simulations for direct tension tests, on one hand, and triplet test with and without normal confinements, on the other hand, were presented for the lattice model. One of the features of the lattice model is to capture the snap-back instabilities in load-displacement curves while using a linear elastic analysis with a beam removal strategy. The implemented lattice model is able to predict the failure of the brick-mortar interface, and to capture its debonding in tension and its delamination in shear, and also to record snap-back instabilities caused by the localization of the fracture process.

Chapter 4 THE MECHANICS OF INTERFACE CRACKS

Interface is the weakest part of composites like masonry the failure of which may often occur at this weak part by debonding process and separation which form interface cracks. This has made the interfacial fracture mechanics an important topic of research in applied mechanics over the past few decades. In general, the failure mechanism of composites depends on the geometry of the specimen, the applied loading, and the surrounding materials and interface toughness. The interface debonding may be due to a lower interface toughness compared to that of the abutting dissimilar elastic materials. Since in masonry composites an interface is a low-toughness fracture path through joined solids, i.e., brick units and mortar joints, mode mixity of crack propagation must be concerned. Because unlike an isotropic brittle solid, the interface crack in a heterogeneous masonry is not free to evolve with pure mode 1 stressing at its tip. Different elastic moduli of the materials surrounding the interface, possible non-symmetric loading and also geometry may induce a made 2 failure component. Because of the strut removal strategy, the implemented lattice model is capable of capturing discontinuities and cracks occurring at the simulated mesh during loading. Mode 1 and mode 2 displacements of the crack tip can be obtained by the lattice model while the discontinuity evolves. This feature along with energy method may be used to determine required fracture quantities of mode 1 and 2. The following sections explain the essentials of the mechanics of interface cracks before discussing about applying the concepts of interfacial fracture mechanics in the lattice model which is the subject of the following chapters.

4.1 Dundur’s Parameters

Consider two isotropic elastic solids which are in contact through their interface along x-axis as shown in Figure 4-1. Material 1 is above the interface and the origin is at the crack tip. Let μ_j, E_j, and ν_j ($j = 1,2$ as material index) be the shear modulus, Young’s modulus, and Poisson’s ratio of two materials. Dundur’s elastic mismatch parameters [49] can be employed for a wide class of plane problems of elasticity.

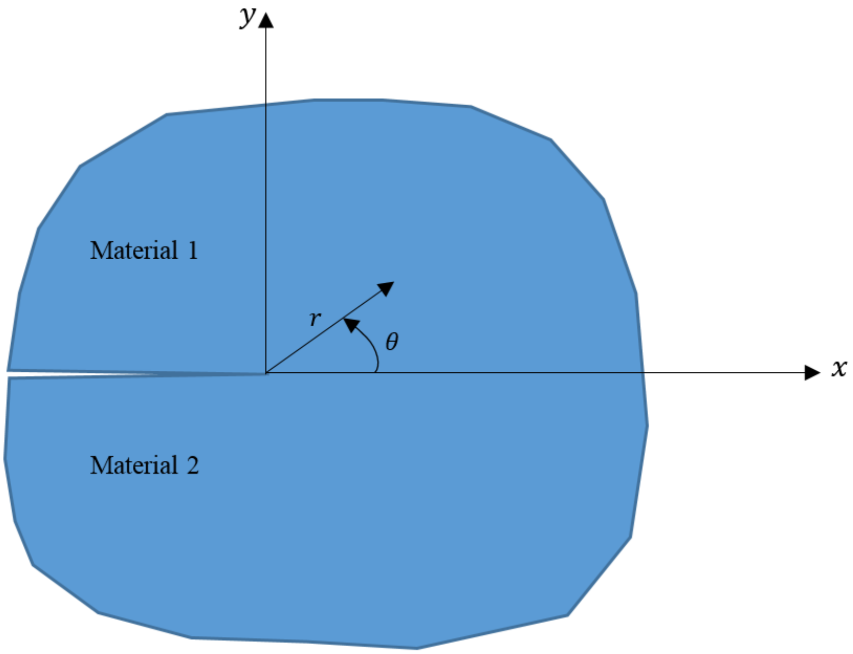

Figure 4-1 A small region near crack tip along bi-material interface.

Since there is displacement continuity along the interface, it follows that

$$(\varepsilon_x)_1 = (\varepsilon_x)_2, \quad (4\text{-}1)$$

where $(\blacksquare)_1$ and $(\blacksquare)_2$ belong to material 1 and 2, respectively. From Equation (4-1) and for plane strain, one can obtain

$$(\sigma_x)_1 = \frac{\mu_1(1-\nu_2)}{\mu_2(1-\nu_1)}(\sigma_x)_2 + \frac{\sigma_y}{1-\nu_1}\left(\nu_1 - \frac{\mu_1}{\mu_2}\nu_2\right). \tag{4-2}$$

If a parameter named α is defined as below

$$\frac{\mu_1(1-\nu_2)}{\mu_2(1-\nu_1)} = \frac{1+\alpha}{1-\alpha}, \tag{4-3}$$

then the Dundur's parameter α for plane strain can be expressed in terms of the elastic properties of the adherent linear isotropic media as

$$\alpha = \frac{\mu_1(1-\nu_2)-\mu_2(1-\nu_1)}{\mu_1(1-\nu_2)+\mu_2(1-\nu_1)}. \tag{4-4}$$

Thus, Equation (4-2) can be represented as

$$(\sigma_x)_1 = \frac{1+\alpha}{1-\alpha}(\sigma_x)_2 + \frac{2\sigma_y}{1-\alpha}(2\beta - \alpha), \tag{4-5}$$

where α and β are two Dundur's elastic mismatch parameters which are generally expressed by

$$\alpha = \frac{\mu_1(\kappa_2+1)-\mu_2(\kappa_1+1)}{\mu_1(\kappa_2+1)+\mu_2(\kappa_1+1)} \tag{4-6}$$

and

$$\beta = \frac{\mu_1(\kappa_2-1)-\mu_2(\kappa_1-1)}{\mu_1(\kappa_2+1)+\mu_2(\kappa_1+1)}, \tag{4-7}$$

where $\kappa_j = 3 - 4\nu_j$, Kolosov's constant, for plane strain and $\kappa_j = (3 - \nu_j)/(1 + \nu_j)$ for plane stress. For plane strain

$$\beta = \frac{\mu_1(1-2\nu_2)-\mu_2(1-2\nu_1)}{2[\mu_1(1-\nu_2)+\mu_2(1-\nu_1)]}\,. \qquad (4\text{-}8)$$

The α-parameter is a measure of the mismatch in the in-plane tensile modulus across the interface [32]. When $E_1 \gg E_2$ meaning that material 1 is extremely stiff compared to material 2, α approaches 1 while it would be -1 when $E_1 \ll E_2$ or material 1 is extremely compliant. When there is no mismatch like a homogeneous isotropic elastic solid, $\alpha = \beta = 0$, and their sign is changed when two materials are switched with respect to the interface. The β-parameter measures the mismatch in the in-plane bulk moduli [32]. As it can be seen in (4-8), when both materials are incompressible, $\nu_1 = \nu_2 = 1/2$, β vanishes, and $\beta = \alpha/4$ when $\nu_1 = \nu_2 = 1/3$.

The physical accepted values of α and β for plane strain bi-material systems lie inside a parallelogram enclosed by $\alpha = \pm 1$ and $\alpha - 4\beta = \pm 1$ in the (α, β) plane, assuming nonnegative Poisson's ratios, as shown in Figure 4-2. In plane stress this range for α and β is somewhat more restricted. In this figure, material 1 is stiffer leading to a positive α. It may be noticed that most of the points in Figure 4-2 fall between $\beta = 0$ and $\beta = \alpha/4$. The point associated with Brick/Mortar interface is related to this study while all others except Granite/Mortar corresponds to reference [32]. The Point for Granite/Mortar interface was reported by Büyüköztürk and Lee [50] for high strength aggregates and mortar interface in concrete composites. It is seen that the points of Brick/Mortar and Granite/Mortar interfaces are in proximity in the (α, β) plane, as they are both related to cementations bi-material systems.

Crack tip displacement and stress fields oscillate when $\beta \neq 0$, which results in crack surface interpenetration. This interpenetration introduces ambiguity into the characteristics of interface fracture [26], [31]. However, since for many bi-material systems of interest including masonry and concrete [50], the value of β is small [51], it is assumed that a zero-β hypothesis should provide an adequate interface fracture characterization in many cases.

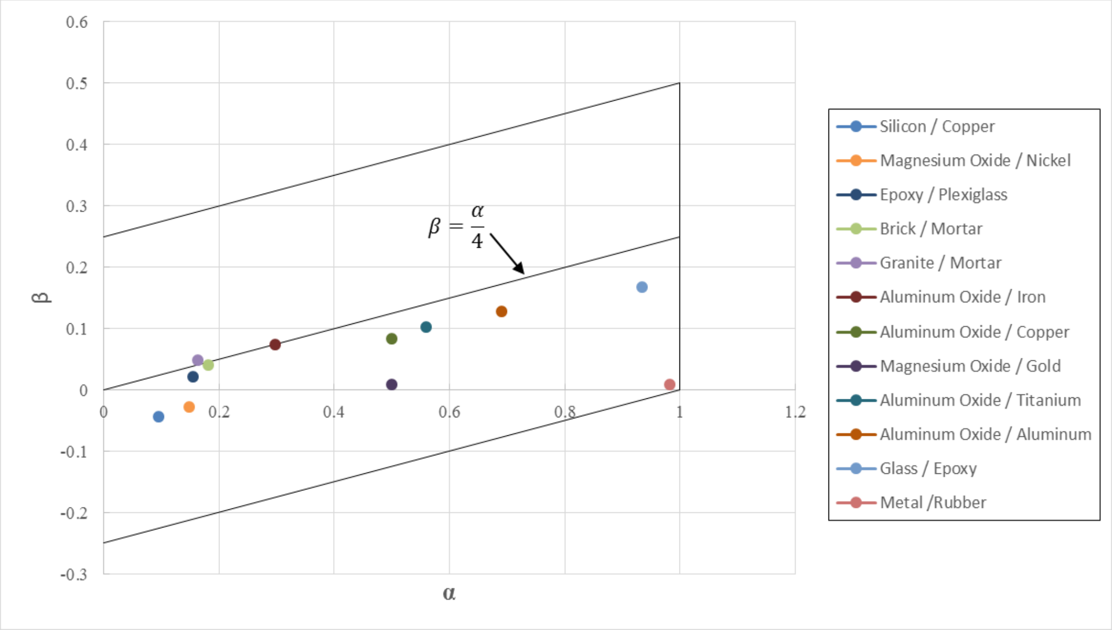

Figure 4-2 Values of Dundur's parameters for some plane strain bi-material systems (Material 1 / Material 2).

4.2 Complex Representation of Crack Problems

Muskhelishvili [21] showed that any problem in the plane theory of elasticity can be solved by finding two complex functions, satisfying the boundary conditions of that problem. Assuming plane deformations and no body forces for the equilibrium equations of an elastic body, it can be shown that there always exists a *stress function* or *Airy function* $U(x, y)$ satisfying bi-harmonic equation

$$\Delta\Delta U = 0 \quad \text{or} \quad \frac{\partial^4 U}{\partial x^4} + 2\frac{\partial^4 U}{\partial x^2 \partial y^2} + \frac{\partial^4 U}{\partial y^4} = 0. \qquad (4\text{-}9)$$

The solution of Equation (4-9) is called bi-harmonic function. The derivatives of $U(x, y)$ are continuous up to and including the fourth order and are single-valued, starting from the second order, throughout the region under consideration. Using $U(x, y)$, the stresses and also displacements may be obtained at every point on the body.

Muskhelishvili also showed that every stress function or bi-harmonic function $U(x, y)$ of the two variables x and y may be represented in a very simple manner by using two functions of the complex variable $z = x + iy$, $i = \sqrt{-1}$. This is an important characteristic of stress functions for the plane theory of elasticity because the properties of functions of a complex variable are generally well known. $U(x, y)$ may be expressed in terms of two analytic complex functions $\phi(z)$ and $\chi(z)$, or $\Phi(z)$ and $\Psi(z)$ as [21]

$$\begin{gathered} U(x, y) = Re\{\bar{z}\phi(z) + \chi(z)\}\ or \\ U(x, y) = Re\{\bar{z}\int \Phi(z)dz + \iint \Psi(z)dz\}, \end{gathered} \qquad (4\text{-}10)$$

where

$$\phi(z) = \int \Phi(z)dz + const., \text{ and } \chi(z) = \iint \Psi(z)dz + +const., \qquad (4\text{-}11)$$

in which $Re\{\blacksquare\}$ denotes the real part of complex variable $\blacksquare$, $\bar{z}$ is the complex conjugate of z, i.e., $\bar{z} = x - iy$, and $\phi(z)$, $\chi(z)$ are also called Goursat functions satisfying the boundary conditions of the problem under consideration. These type of functions were first used by French mathematician, Édouard Goursat, in 1898 and are therefore sometimes referred to as Goursat functions. A complex function $\phi(z)$ is *analytic* or *holomorphic* in a region lying entirely in the complex plane if it is single valued or unique in that region and its complex derivative $\phi'(z) = \partial\phi/\partial z$ exists at each point of the region [52]. If a complex function is holomorphic or analytic in a region, then all derivatives of that complex function exist and are holomorphic in that region. It follows that

$$\Delta U = 4Re\{\Phi(z)\}, \text{ and } \Delta\Delta U = 0. \tag{4-12}$$

Therefore, stresses and displacements of a homogeneous isotropic elastic solid may be obtained using these two Goursat functions as [21]

$$(\sigma_x) + (\sigma_y) = 2[\phi'(z) + \overline{\phi'(z)}] = 4Re[\phi'(z)] = 4Re[\Phi(z)], \tag{4-13}$$

$$(\sigma_y) - (\sigma_x) + 2i(\sigma_{xy}) = 2[\bar{z}\phi''(z) + \chi''(z)] = 2[\bar{z}\Phi'(z) + \Psi(z)], \text{ and} \tag{4-14}$$

$$2\mu(u + iv) = \kappa\phi(z) - z\overline{\phi'(z)} - \overline{\chi'(z)} = \kappa\int \Phi(z)dz - z\overline{\Phi}(\bar{z}) - \int \overline{\Psi}(\bar{z})d\bar{z}, \tag{4-15}$$

where u, v are components of displacement along x and y axes, σ_x, σ_y, σ_{xy} are components of stress, μ denotes the shear moduli, κ represents the Poisson's ratios as defined earlier, $\phi'(z) = \Phi(z)$, $\chi''(z) = \Psi(z)$, the prime denotes differentiation with respect to z and an overbar complex conjugate. The details have been elaborated by Muskhelishvili in the reference [21]. Hence, for any specific homogeneous isotropic elastic body, there are two complex functions $\phi(z)$ and $\chi(z)$ which satisfy the boundary conditions of that body by the help of which the stresses and displacements may be determined.

4.2.1 Homogeneous Cracks

Equations (4-13) to (4-15) may be employed to obtain stress and displacement fields in a homogeneous isotropic elastic solid with a traction free crack like what is shown in Figure 4-1 such that materials 1 and 2 are the same and there is no bi-material interface. The following complex eigenvalue Goursat functions may be considered to determine the stress and displacement values [53].

$$\phi(z) = \sum_{n=0}^{\infty} A_n z^{\lambda_n}, \chi(z) = \sum_{n=0}^{\infty} B_n z^{\lambda_n+1}, \tag{4-16}$$

where the eigenvalues λ_n $(n = 0, 1, 2, \dots)$ are real and A_n and B_n are complex constants of the form $(a_n^1 + i a_n^2)$ and $(b_n^1 + i b_n^2)$, respectively. Since the crack surfaces are also traction free, one can write

$$\sigma_y = \sigma_{xy} = 0 \text{ for } \theta = \pm\pi. \tag{4-17}$$

Adding Equations (4-13) and (4-14) to obtain $\sigma_y + i\sigma_{xy}$ in terms of the λ_n and constants in (4-16) and employing the boundary conditions (4-17), the eigenvalues and constants are obtained after some manipulations by

$$\lambda_n = \frac{n}{2}; \quad n = 0, 1, 2, \dots \text{ and} \tag{4-18}$$

$$-b_n^1 = \left(\frac{\frac{n}{2} + (-1)^n}{\frac{n}{2} + 1}\right) a_n^1, \quad -b_n^2 = \left(\frac{\frac{n}{2} - (-1)^n}{\frac{n}{2} + 1}\right) a_n^2. \tag{4-19}$$

Equations (4-13) and (4-14) are again used to obtain $\sigma_x + i\sigma_{xy}$ in terms of a_n^1, a_n^2, b_n^1, and b_n^2. Having $\sigma_y + i\sigma_{xy}$ and $\sigma_x + i\sigma_{xy}$ in terms of the complex constants and eigenvalues in Equations (4-18) and (4-19), substituting the trigonometric form of complex numbers, and separating into real and imaginary parts, one can determine the stresses σ_x, σ_y, and σ_{xy} and displacement u and v as series expansions in terms of n, r, θ, a_n^1, and a_n^2, as presented by Equations (1.34) to (1.38) in reference [53].

It can be seen from stress field equations (1.34), (1.35), and (1.36) in [53] that the first term, $n = 1$, of the stress series gives stress as a function of the reciprocal of $\sqrt{r}$ providing infinite stress at the crack tip while the higher order terms, $n > 1$, result in zero stress at the crack tip. Thus, only the first term of the infinite expansion corresponds to the crack tip stress singularity. The famous mixed mode near crack tip stresses and displacements are found considering only $n = 1$ as follows:

$$\sigma_x = \frac{a_1^1}{\sqrt{r}}\left(1 - sin\frac{\theta}{2}sin\frac{3\theta}{2}\right)cos\frac{\theta}{2} + \frac{a_1^2}{\sqrt{r}}\left(2 + cos\frac{\theta}{2}cos\frac{3\theta}{2}\right)sin\frac{\theta}{2}, \qquad \text{(4-20)}$$

$$\sigma_y = \frac{a_1^1}{\sqrt{r}}\left(1 + sin\frac{\theta}{2}sin\frac{3\theta}{2}\right)cos\frac{\theta}{2} - \frac{a_1^2}{\sqrt{r}}cos\frac{\theta}{2}cos\frac{3\theta}{2}sin\frac{\theta}{2}, \qquad \text{(4-21)}$$

$$\sigma_{xy} = \frac{a_1^1}{\sqrt{r}}cos\frac{\theta}{2}cos\frac{3\theta}{2}sin\frac{\theta}{2} - \frac{a_1^2}{\sqrt{r}}\left(1 - sin\frac{\theta}{2}sin\frac{3\theta}{2}\right)cos\frac{\theta}{2}, \qquad \text{(4-22)}$$

$$u = \frac{a_1^1\sqrt{r}}{4\mu}\left\{(2\kappa - 1)cos\frac{\theta}{2} - cos\frac{3\theta}{2}\right\} - \frac{a_1^2\sqrt{r}}{4\mu}\left\{(2\kappa + 3)sin\frac{\theta}{2} + sin\frac{3\theta}{2}\right\}, \text{ and} \qquad \text{(4-23)}$$

$$u = \frac{a_1^1\sqrt{r}}{4\mu}\left\{(2\kappa + 1)sin\frac{\theta}{2} - sin\frac{3\theta}{2}\right\} + \frac{a_1^2\sqrt{r}}{4\mu}\left\{(2\kappa - 3)cos\frac{\theta}{2} + cos\frac{3\theta}{2}\right\}. \qquad \text{(4-24)}$$

Stress fields directly ahead of the crack tip, $\theta = 0$, are only in terms of $a_1^1/\sqrt{r}$ and $a_1^2/\sqrt{r}$, which if compared with Irwin's expressions of stresses in mode 1 and mode 2, it follows that

$$\begin{aligned} a_1^1 &= \frac{K_1}{\sqrt{2\pi}}, \\ a_1^2 &= \frac{K_2}{\sqrt{2\pi}}, \end{aligned} \qquad (4\text{-}25)$$

showing that the coefficients a_1^1 and a_1^2 are measures of stress intensity factors in mode 1 and 2, respectively.

Therefore, employing complex function approach of Muskhelishvili, an infinite series solution for a crack in a 2D isotropic homogeneous material was derived and the first term of this series has been shown to be related to the near crack tip singular stress field as given by Irwin. Solutions given by Equations (4-20) to (4-24) can be split into two separate fields associated with the mode 1 and mode 2 displacements. a_1^1 and a_1^2 in these equations correspond to mode 1 and mode 2, respectively.

4.2.2 Bi-material Interface Cracks

In bi-material systems, the elastic properties are discontinuous across the interface, where four complex functions, or Goursat functions, $\Phi_j(z)$, $\Psi_j(z)$, $j = 1, 2$, of the complex variable $z = x + iy$ are needed to completely characterize the problem. Similarly, the basic equations for displacement and stress fields for two dimensional isotropic elasticity as used by Kolosov-Muskhelishvili are [21], [23] as follows:

$$(\sigma_x)_j + (\sigma_y)_j = 4Re\left[\phi'_j(z)\right] = 4Re[\Phi_j(z)], \qquad (4\text{-}26)$$

$$\begin{gathered} (\sigma_y)_j - (\sigma_x)_j + 2i\left(\sigma_{xy}\right)_j = 2[\bar{z}\phi''_j(z) + \chi''_j(z)] = \\ 2[\bar{z}\Phi'_j(z)+\Psi_j(z)], \text{ and} \end{gathered} \qquad (4\text{-}27)$$

$$\begin{gathered} 2\mu_j\left(u_j + iv_j\right) = \kappa_j\phi_j(z) - z\overline{\phi'_j(z)} - \overline{\chi'_j(z)} = \kappa_j \int \Phi_j(z)dz - \\ z\overline{\Phi_j}(\bar{z}) - \int \overline{\Psi_j}(\bar{z})d\bar{z}, \end{gathered} \qquad (4\text{-}28)$$

where z belongs to material 1 region for $j = 1$ and material 2 region for $j = 2$, u_j, v_j are components of displacement along x and y axes, shown in Figure 4-1, $(\sigma_x)_j$, $(\sigma_y)_j$, $\left(\sigma_{xy}\right)_j$ are components of stress, μ_j denotes the shear moduli, and κ_j is the Kolosov's constant representing the Poisson's ratios for material j, $j = 1, 2$.

Erdogan [54] used Equations (4-26) to (4-28) to solve for stress distribution in a nonhomogeneous elastic plane with cracks where a bi-material interface has some cracks with specified lengths. As mentioned by Erdogan, the holomorphic functions $\Phi_1(z)$ and $\Psi_1(z)$ were defined in region 1, but not in region 2. By extending the definition of $\Phi_1(z)$ into region 2 and $\Phi_2(z)$ into region 1 in such a way that they are holomorphic on the unloaded parts of the boundary, the following substitution may be made [54]:

$$\Psi_j(z) = -\Phi_j(z) - \overline{\Phi}_j(z) - z\Phi'_j(z), \tag{4-29}$$

where z is in region 1 for $j = 1$ and z is in region 2 for $j = 2$. From Equations (4-26) to (4-29), one may write [54]

$$(\sigma_y)_j - i\left(\sigma_{xy}\right)_j = \Phi_j(z) - \Phi_j(\bar{z}) + (z - \bar{z})\overline{\Phi'_j(z)} \text{ and} \tag{4-30}$$

$$2\mu_j\left(u'_j + iv'_j\right) = \kappa_j\Phi_j(z) + \Phi_j(\bar{z}) - (z - \bar{z})\overline{\Phi'_j(z)}. \tag{4-31}$$

The purpose was to find the stress distributions in region 1 (lower-half plane) and in region 2 (upper-half plane) provided that surface tractions vanish along crack surfaces (union of cracked segments named L') , there are displacement and stress continuities along the bonded interface (union of bonded segments named L), and the x, y-components of resultant force acting along the bonded interface are known. Using

Muskhelishvili's equations and considering the above three conditions, he showed that the problem may be reduced to the solution of a homogeneous Hilbert problem as given by [54]

$$\begin{aligned} {\Phi_1}^{+}(t) + \alpha^{*}{\Phi_1}^{-}(t) = 0 \quad \text{on } L, \\ {\Phi_1}^{+}(t) - {\Phi_1}^{-}(t) = 0 \quad \text{on } L' \text{ as boundary condition,} \end{aligned} \qquad \text{(4-32)}$$

where t is the coordinate on the real $x - axis$ or plane cut along L, superscripts $+$ and $-$ refer to the values of the functions as z approaches t from the upper and lower half-planes, respectively, subscript 1 refers to material 1, $\Phi_1(z)$ is holomorphic in the whole plane cut along L, and α^{*} is a bi-elastic constant defined by

$$\alpha^{*} = \left(\frac{\kappa_1}{\mu_1} + \frac{1}{\mu_2}\right) / \left(\frac{\kappa_2}{\mu_2} + \frac{1}{\mu_1}\right). \qquad \text{(4-33)}$$

Equation (4-32) is a homogeneous Hilbert problem since its right hand side is zero. Muskhelishvili called the problem in (4-32) "the problem of linear relationship of the boundary values" because the boundary values are connected or related by a linear expression with, in general, variable coefficients. It should be noted that for the entire plane $\Phi_1(z) + \Phi_2(z) = 0$ [54].

From the general solution of the Hilbert problem, Erdogan [54] obtained the complex stress function, $\Phi_1(z)$, in the vicinity of the crack tip, as shown in Figure 4-1. Substituting $\Phi_1(z)$ into Equations (4-26) and (4-30), one obtains

$$(\sigma_x)_1 + (\sigma_y)_1 = 4Re\left[\frac{\alpha_0}{\sqrt{r}} e^{\varepsilon(\theta-\pi)} e^{-i\left(\varepsilon \ln r + \frac{\theta}{2}\right)}\right] + O(\sqrt{r}) \text{ and} \qquad \text{(4-34)}$$

$$\begin{aligned}(\sigma_y)_1 - i(\sigma_{xy})_1 = \frac{\alpha_0}{\sqrt{r}}\left[e^{\varepsilon(\theta-\pi)}e^{-i\left(\varepsilon\ln r+\frac{\theta}{2}\right)} + e^{-\varepsilon(\theta-\pi)}e^{i\left(-\varepsilon\ln r+\frac{\theta}{2}\right)}\right] \\ -\frac{\overline{\alpha_0}}{\sqrt{r}}\left[(2\varepsilon+i)e^{\varepsilon(\theta-\pi)}\sin(\theta)\,e^{i\left(\frac{3\theta}{2}+\varepsilon\ln r\right)}\right] + O(\sqrt{r}),\end{aligned} \qquad (4\text{-}35)$$

where $\alpha_0 = (k_1 - ik_2)/2\sqrt{2}$ is a complex constant, $k_1 = K_1/\sqrt{\pi}\cosh(\pi\varepsilon)$, $k_2 = K_2/\sqrt{\pi}\cosh(\pi\varepsilon)$, r and θ are shown in Figure 4-1, and ε is the bi-elastic constant defined as

$$\varepsilon = \frac{1}{2\pi} ln(\frac{1-\beta}{1+\beta}). \qquad (4\text{-}36)$$

Displacement values may also be obtained by putting $\Phi_1(z)$ into Equation (4-31) and resolving it into real and imaginary components. Erdogan [54] obtained the above stress components in Cartesian coordinate system while Sih and Rice [55] determined the stress components in polar coordinates taking advantage of the bi-harmonic Airy stress function developed by Williams [22] besides the complex function approach of Muskhelishvili.

Using Equation (4-35) with some manipulations, the tractions on the interface directly ahead of the tip, i.e., $\theta = 0$, are given by

$$(\sigma_y)_j + i\left(\tau_{xy}\right)_j = K(2\pi r)^{-1/2}r^{i\varepsilon} \qquad (4\text{-}37)$$

or

$$(\sigma_y)_j = Re[Kr^{i\varepsilon}]\,(2\pi r)^{-1/2},\ \ \left(\tau_{xy}\right)_j = Im[Kr^{i\varepsilon}]\,(2\pi r)^{-1/2}, \qquad (4\text{-}38)$$

where $K = K_1 + iK_2$ is the complex stress intensity factor, $r^{i\varepsilon} = e^{i\varepsilon ln(r)} = \cos(\varepsilon ln(r)) + i\, sin(\varepsilon ln(r))$ is a so-called oscillatory singularity, and ε is the bi-elastic constant defined in Equation (4-36).

Employing Erdogan [54] or Sih and Rice [55] approach, the relative crack flank displacements of two points on the top and bottom of crack surfaces, Δu and Δv, at a distance r behind the crack tip are expressed as

$$\Delta v + i\Delta u = \frac{8K\sqrt{\frac{r}{2\pi}}}{(1+2i\varepsilon)\cosh(\pi\varepsilon)E_*} r^{i\varepsilon}, \tag{4-39}$$

where $\Delta u = u(r, \theta = \pi) - u(r, \theta = -\pi)$, $\Delta v = v(r, \theta = \pi) - v(r, \theta = -\pi)$, $\frac{1}{E_*} = \frac{1}{2}(\frac{1}{\bar{E}_1} + \frac{1}{\bar{E}_2})$ and $\bar{E}_j = E_j/(1 - {\nu_j}^2)$ for plane strain and $\bar{E}_j = E_j$ for plane stress. For plane strain problems, Equation (4-39) reduces to

$$\Delta v + i\Delta u = \frac{2\left[\frac{1-\nu_1}{\mu_1} + \frac{1-\nu_2}{\mu_2}\right]K\sqrt{\frac{r}{2\pi}}}{(1+2i\varepsilon)\cosh(\pi\varepsilon)} r^{i\varepsilon}. \tag{4-40}$$

The complex stress intensity factor K can generally be expressed in terms of its modulus$|K| = \sqrt{{K_1}^2 + {K_2}^2}$, and the loading phase angle ψ by

$$K = |K|e^{i\psi}. \tag{4-41}$$

Since the crack surface displacement is a complex number, $\Delta v + i\Delta u$, it can also be written as $\Delta v + i\Delta u = [\Delta u^2 + \Delta v^2]^{1/2}e^{i\varphi}$, where $\varphi = arc\tan(\frac{\Delta u}{\Delta v})$. By equating this expression with Equation (4-40) and after some manipulations, $|K|$can be expressed in terms of the crack surface displacements as [28]

$$|K| = [(1 + 4\varepsilon^2)(\Delta u^2 + \Delta v^2)]^{1/2}/q, \tag{4-42}$$

where $q = \sqrt{2}\left[\frac{1-\nu_1}{\mu_1} + \frac{1-\nu_2}{\mu_2}\right]/(\sqrt{\pi}\cosh(\pi\varepsilon))$ for plane strain. The loading phase angle is given by

$$\psi = \omega + \gamma, \tag{4-43}$$

where $\gamma = arc\tan(2\varepsilon)$ is the principal argument of the complex number $1 + i2\varepsilon$, and $\omega = \varphi - \varepsilon ln(r)$.

G. R. Irwin [56] also used Equations (4-20) and (4-21) to characterize the mode 1 stress field near the end of a somewhat brittle tensile fracture of a homogeneous solid, introducing the coefficient $(EG/\pi)^{1/2}$ as the stress intensity factor for plane stress. The energy release rate and the modulus of stress intensity are generally correlated by the Irwin-type relation for bi-material interface cracks expressed as

$$G = \frac{(1-\beta^2)|K|^2}{E_*} = \frac{|K|^2}{E_*\cosh^2(\pi\varepsilon)}\,. \tag{4-44}$$

For plane strain problem, $|K|$ is related to G by

$$G = \frac{\left(\frac{1-\nu_1}{\mu_1}+\frac{1-\nu_2}{\mu_2}\right)|K|^2}{4\cosh^2(\pi\varepsilon)} \tag{4-45}$$

or

$$|K| = \sqrt{\frac{4\cosh^2(\pi\varepsilon)G}{\frac{1-\nu_1}{\mu_1}+\frac{1-\nu_2}{\mu_2}}}\,. \tag{4-46}$$

Equations (4-42) to (4-46) can be used to obtain interfacial fracture quantities from numerical solutions. The energy release rate, G, can firstly be calculated through an energy method like virtual crack extension procedure [27] or other numerical solutions such as the lattice model with strut removal strategy where a discontinuity may be developed during analysis due to applied loading in form of a crack. This will further be explained in detail. Equation (4-46) can then directly be used to obtain $|K|$, which is independent of the crack flank displacements and the distance r behind the crack tip. As an internal consistency check, the relative near tip crack surface displacements obtained directly from numerical simulations may be inserted into Equation (4-42) to obtain an independent estimate of $|K|$ to be compared with that of Equation (4-46) [29]. The stress intensity factors for mode 1 and mode 2 are then calculated using the phase angle by

$$K_1 = Re(K) = |K|\cos(\psi) \text{ and} \tag{4-47}$$

$$K_2 = Im(K) = |K|\sin(\psi). \tag{4-48}$$

In circumstances when the Dundur's parameter β is nonzero and thus $\varepsilon \neq 0$, a pure mode 1 crack with zero shear traction along the interface happens at a distance $\hat{L}$ ahead of the tip and a pure mode 2 crack with zero normal traction on the interface is at that point. Since the ratio of the shear traction to normal traction on the interface varies (very slowly) with distance to the tip when $\beta \neq 0$, the measure of the proportion of mode 2 to mode 1 in the vicinity of the crack tip requires the specification of some length quantity, $\hat{L}$ [32]. The choice of this characteristic length, $\hat{L}$, is somewhat arbitrary but when chosen it should not change throughout the analysis. This characteristic length establishes a new rotated quantity $\widehat{K}_1 + i\widehat{K}_2$ with the same modulus $|K|$ as $K_1 + iK_2$(note that $\left|\hat{L}^{i\varepsilon}\right| = 1$ and $\left|K\hat{L}^{i\varepsilon}\right| = |K|$) but an augmented phase angle $\hat{\psi}$ which unlike ψ is insensitive to the choice of length unit [29]. From the definition of complex stress intensity factor in (4-41), one may write

$$K = |K|e^{i\psi} \overset{\times\hat{L}^{i\varepsilon}}{\Longrightarrow}$$

$$K\hat{L}^{i\varepsilon} = |K|e^{i\psi}\hat{L}^{i\varepsilon} \xRightarrow{\hat{L}^{i\varepsilon}=e^{i\varepsilon ln\hat{L}}} K\hat{L}^{i\varepsilon} = |K|e^{i\psi}e^{i\varepsilon ln\hat{L}} = |K|e^{i(\psi+\varepsilon ln\hat{L})} = |K|e^{i\hat{\psi}}.$$

Therefore, the effect of characteristic length is considered as

$$K\hat{L}^{i\varepsilon} = |K|e^{i\hat{\psi}} \text{ and} \tag{4-49}$$

$$\hat{\psi} = \psi + \varepsilon ln\hat{L}. \tag{4-50}$$

From Equation (4-43), one could obtain ψ by

$$\psi = \omega + \gamma = \varphi - \varepsilon ln(r) + \gamma \xRightarrow{+\varepsilon ln\hat{L}} \psi + \varepsilon ln\hat{L} = \varphi - \left(\varepsilon ln(r) - \varepsilon ln\hat{L}\right) + \gamma =$$

$$\varphi - \varepsilon ln\left(\frac{r}{\hat{L}}\right) + \gamma.$$

Thus,

$$\hat{\psi} = \varphi - \varepsilon ln\left(\frac{r}{\hat{L}}\right) + \gamma, \tag{4-51}$$

which determines that value of augmented phase angle $\hat{\psi}$. Therefore, the value of ψ is replaced by $\hat{\psi}$ in Equations (4-43), (4-47), and (4-48) when the characteristic specimen length $\hat{L}$ is introduced in the analysis and the modulus of K remains the same. In this study, $\hat{L}$ is usually considered as specimen height, e.g., $h_1 + h_2$ in Figure 1-1.

4.3 Summary

Interfacial fracture mechanics is an important topic of research in applied mechanics over the past few decades since the interface of two materials in contact is the weakest part of composites like masonry along which failure usually occurs. Different elastic properties of abutting dissimilar materials introduce mismatches in the in-plane tensile modulus and bulk modulus across the interface, quantified by the α-, and β-parameters, respectively. These parameters are obtained by using the displacement continuity conditions along the interface in plane theory of elasticity. For bi-material systems, the physical accepted values of α and β for plane strain bi-material systems lie inside a parallelogram in the (α, β) plane, assuming nonnegative Poisson's ratios. This range is somewhat more restricted for plane stress. It was observed that the points of Brick/Mortar interface in this study and Granite/Mortar interface reported by Büyüköztürk and Lee [50] are in proximity in the (α, β) plane, as they are both related to cementations bi-material systems. Moreover, β has an important property which corresponds to so-called oscillatory singularity [32] bringing some complications that are absent in the elastic fracture mechanics of homogeneous solids. Crack tip displacement and stress fields oscillate when $\beta \neq 0$, which results in crack surface interpenetration. This interpenetration introduces ambiguity into the characteristics of interface fracture [26], [31]. Nonetheless, for many bi-material systems of interest including masonry and concrete [50], the value of β is small [51], and may be regarded as zero.

Most of the research in developing analytical solutions of the mechanics of interface cracks in recent decades is based on the work of Muskhelishvili as he showed that any problem in the plane theory of elasticity can be solved by finding two complex functions so called Goursat functions, satisfying boundary conditions of that problem. Using these two complex functions, stresses and displacements of a homogeneous isotropic elastic solid may be determined. He employed complex functions since the properties of functions of a complex variable are generally well known.

In bi-material systems, the elastic properties are discontinuous across the interface, where four complex functions of the complex variable are needed to completely characterize the problem. The same Muskhelishvili's equations developed for displacement and stress fields of a two dimensional homogeneous isotropic solid are also employed in solving bi-material interface cracks. Erdogan [54] used these relations to solve for stress distribution in a nonhomogeneous elastic plane with cracks where a bi-material interface has some cracks with specified lengths. Using Muskhelishvili's equations and considering the boundary conditions, he showed that the bi-material interface crack problem may be reduced to the solution of a homogeneous Hilbert problem which Muskhelishvili called "the problem of linear relationship of the boundary values". From the general solution of the Hilbert problem, Erdogan [54] obtained the stress components in Cartesian coordinate system while Sih and Rice [55] determined the stress components in polar coordinates taking advantage of the bi-harmonic Airy stress function developed by Williams [22] along with the complex function approach of Muskhelishvili. Employing Erdogan [54] or Sih and Rice [55] approach with some further developments, it is possible to correlate the complex stress intensity factor modulus with the energy release rate as crack evolves. This may be used in numerical simulation techniques to obtain the fracture quantities of the bi-material systems while the crack propagates as used in the crack surface displacement method [29]. When the Dundur's parameter β is nonzero and thus $\varepsilon \neq 0$, there may be a need to specify a length quantity, $\hat{L}$, to make the loading phase angle insensitive to the choice of length unit. Although this length can be chosen arbitrarily, when selected it should not change throughout the analysis. This characteristic length introduces new values for the complex stress intensity factor, not its modulus, and also the loading phase angle.

Chapter 5 LATTICE SIMULATIONS OF SOME CLASSIC FRACTURE PROBLEMS

The implemented 2D lattice model explained in chapter 3 is capable of simulating crack path evolution in the form of strong discontinuities at a homogeneous or heterogeneous solid. Since the crack propagation is captured by the lattice during an analysis, it is postulated that the fracture mechanics quantities like the energy release rate or the stress intensity factors associated with the evolving crack may be determined by the lattice. Other numerical techniques like the classic finite element method of virtual crack extension ([27], [28], [29], [30]) or the well-known extended finite element method (XFEM) ([57], [58], [59]) may also be used for obtaining the fracture quantities of crack problems. In the virtual crack extension procedure, as used by Charalambides et al. [28] and Matos et al. [29], a pre-cracked finite element mesh with length a was considered and the virtual crack extension method was applied by virtually increasing the crack length and changing the stiffness of a ring of elements around the crack tip. This method is not based on a progressive crack evolution where the crack length a increases during a single simulation. XFEM, which is based on the mathematical foundation of the partition of unity finite element method, is also capable of measuring the fracture quantities. However, its implementation needs much more effort and considerations than the lattice regarding, for instance, modeling the arbitrary crack propagation paths handled by level set method, multiple crack configurations, cracks intersecting with other discontinuities, and also cracks emanating from holes or other internal interfaces. Although the goal here is not to compare the capabilities of XFEM and the lattice model, its relative simplicity both in theory and implementation along with accepted results make the lattice model an interesting approach in solving crack problems in the context of fracture mechanics.

In this chapter, some well-known classic crack problems for which analytical solutions are available are simulated by the implemented lattice model. The stress intensity factors calculated by the analytical solutions are compared with those obtained by the lattice to confirm its numerical capabilities in predicting the desired fracture quantities. The energy method, which will be explained in the next section, is employed to directly obtain the energy release rate from the lattice mesh as crack evolves. Three benchmark problems have been considered for this purpose, namely the center cracked problem in a homogeneous domain, the single edge notch problem in a homogeneous solid, and at last, the center interface cracked problem in a bi-material system.

5.1 Energy Method

As mentioned before, Equations (4-42) to (4-46) may be used to obtain interfacial fracture quantities from numerical solutions. The main quantity to be calculated is the energy release rate of the interface fracture. This value is determined by an energy approach using the total potential energy, Π, of the lattice solution. Assume that a lattice analysis has been performed on a given planar linear elastic body of '*unit thickness*' containing a crack. The total potential energy of the lattice model solution may be expressed as [60], [27]

$$\Pi = \frac{1}{2}\{u\}^T[K]\{u\} - \{u\}^T\{f\}, \tag{5-1}$$

where $\{u\}$ is a vector of displacements associated with lattice computational or nodal points or nuclei, $[K]$ is the global stiffness matrix of the lattice mesh, and $\{f\}$ is the vector of prescribed nodal loads. The energy release rate is obtained by differentiating Equation (5-1) with respect to crack length, a, as [61]

$$G = -\frac{\partial \Pi}{\partial a} = -\frac{\partial}{\partial a}\left[\{u\}^T\left(\frac{1}{2}[K]\{u\} - \{f\}\right)\right] = \\ -\left[\frac{\partial \{u\}^T}{\partial a}\left(\frac{1}{2}[K]\{u\} - \{f\}\right) + \{u\}^T\left(\frac{1}{2}\frac{\partial [K]}{\partial a}\{u\} + \frac{1}{2}[K]\frac{\partial \{u\}}{\partial a} - \frac{\partial \{f\}}{\partial a}\right)\right]. \tag{5-2}$$

Thus, one can write

$$G = -\left[\frac{\partial \{u\}^T}{\partial a}\left(([K]\{u\} - \{f\}) - \frac{1}{2}[K]\{u\}\right) + \left(\frac{1}{2}\{u\}^T\frac{\partial [K]}{\partial a}\{u\} + \\ \frac{1}{2}\{u\}^T[K]\frac{\partial \{u\}}{\partial a} - \{u\}^T\frac{\partial \{f\}}{\partial a}\right)\right]. \tag{5-3}$$

The value of $([K]\{u\} - \{f\})$ is precisely zero in the finite element and lattice equilibrium solutions at each iteration. Thus,

$$G = -\left[\left(-\frac{1}{2}\frac{\partial \{u\}^T}{\partial a}[K]\{u\} + \frac{1}{2}\{u\}^T[K]\frac{\partial \{u\}}{\partial a}\right) + \left(\frac{1}{2}\{u\}^T\frac{\partial [K]}{\partial a}\{u\} - \\ \{u\}^T\frac{\partial \{f\}}{\partial a}\right)\right]. \tag{5-4}$$

Since the stiffness matrix $[K]$ is symmetric, it can easily be shown that the scalar value on the first parenthesis is zero. This follows that

$$G = -\left[\frac{1}{2}\{u\}^T\frac{\partial [K]}{\partial a}\{u\} - \{u\}^T\frac{\partial \{f\}}{\partial a}\right]. \tag{5-5}$$

Since the crack surfaces here are traction free, one can conclude that $\frac{\partial \{f\}}{\partial a} = 0$. Hence,

$$G = -\frac{\partial \Pi}{\partial a} = -\frac{1}{2}\{u\}^T\frac{\partial [K]}{\partial a}\{u\}. \tag{5-6}$$

Equation (5-6) is the main ingredient to obtain the fracture properties of the interface using the numerical lattice model. $\frac{\partial [K]}{\partial a}$ is the change in the global stiffness matrix when the change in crack length is ∂a, and $\{u\}$ denotes the nuclei displacement vector 'before' the crack length change by ∂a. The approach of choosing $\{u\}$ '*before*' the crack length change is similar to the 'Explicit Forward Euler' approach in, for example, the time stepping scheme used in solving 1st order transient finite element problems. In the numerical solution, $\frac{\partial [K]}{\partial a}$ is approximated by the ratio $\frac{\Delta [K]}{\Delta a}$ expressed as

$$\frac{\partial [K]}{\partial a} \cong \frac{\Delta [K]}{\Delta a} = \frac{1}{\Delta a}\left[[K]_{a+\Delta a} - [K]_a\right], \tag{5-7}$$

where $[K]_{a+\Delta a}$ is the stiffness matrix after the crack growth Δa. Therefore, using Equation (5-6) the interfacial energy release rate may numerically be determined by the lattice analysis as the crack propagates through the interface. It should be mentioned that the value of G obtained from Equation (5-6) is for a specimen with unit thickness. If the thickness $t \neq 1$, then G should be divided by t.

5.2 The Center Cracked Lattice Simulation

In order to validate the fracture analysis results of the lattice, it is required to compare its numerical results with the classic analytical solutions available in the literature. Tada, Paris and Irwin [62] presented a comprehensive review of stress analysis of cracks from two dimensional common test specimens to three dimensional cracked configurations. Figure 5-1 illustrates the homogeneous finite width center cracked test specimen with constant thickness on which a far field tensile stress is applied. Mode 1 crack tip stress intensity factor of this problem is expressed as [62]

$$K_1 = \sigma\sqrt{\pi a}F(a/b), \tag{5-8}$$

where $2a$ is the center crack length, σ is the far field tensile stress, $2b$ is the width of the plate or configuration as illustrated in Figure 5-1, and $F(a/b)$ is an empirical relation. In this study, $F(a/b)$ with 0.3% accuracy of any a/b which was obtained with a modification of Koiter's formula was considered as follows [62], [63]:

$$F(a/b) = \{1 - 0.025(a/b)^2 + 0.06\,(a/b)^4\}\sqrt{sec(\frac{\pi a}{2b})}. \tag{5-9}$$

In Figure 5-1 when $h/b \geq 3$, the plate is practically regarded as an infinite strip as far as the effects of h/b on the stress intensity factor is concerned [62]. Moreover, the values of σ and a need to be updated as the crack propagates during an analysis of a progressive simulation like the lattice model.

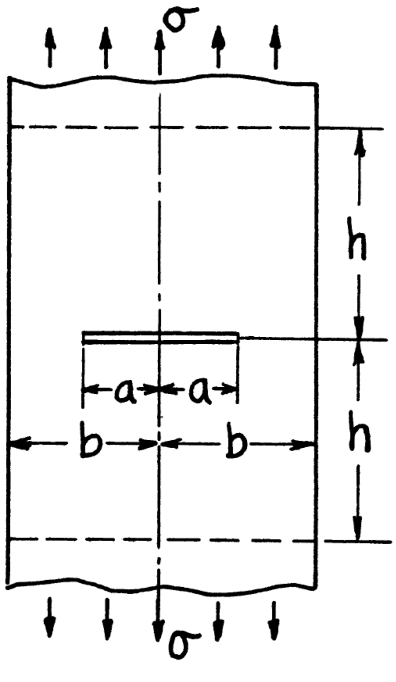

Figure 5-1 Homogeneous finite width center cracked configuration with far field tension [62].

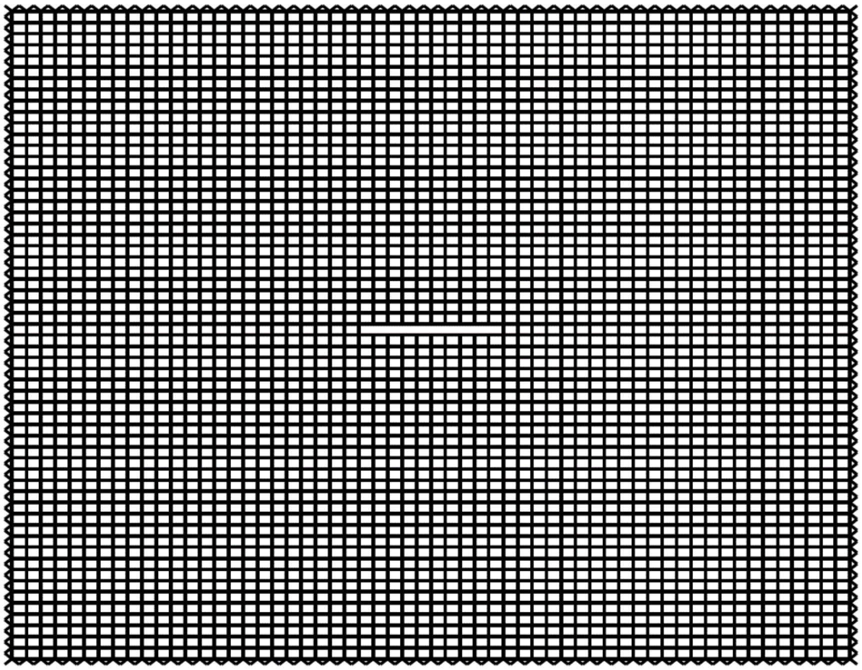

Figure 5-2 Homogeneous finite width center cracked lattice mesh to determine the mode 1 stress intensity factor.

This problem was simulated in the lattice model trying to obtain the stress intensity factor of the crack tip by using the energy method explained in Section 5.1 and Equations (4-43) to (4-51). Figure 5-2 shows the lattice mesh employed to simulate the problem. Different simulations were conducted where the height of the configuration, $2h$, is increased at each simulation to account for the far field tension. If the difference between K_1 obtained by Equations (5-8) and that of the lattice model is considered, the error percentage may be regarded as

$$Error\ \% = \frac{|K_1^l - K_1^a|}{K_1^a} \times 100, \tag{5-10}$$

where K_1^a is the stress intensity factor of the analytical relation, and K_1^l is that of the lattice in $(lbf/in^2)\sqrt{in}$. Figure 5-3 shows the error percentage of four lattice simulations with different h/b ratios as the crack length, a, increases. As illustrated, the error plummets as the height of the specimen, h/b, goes up. The error is just under 40% for $h/b = 1$ while it descends under 1% when $h/b = 4$. This error decreases further with higher values of h/b. It is confirmed that the implemented lattice model is accurately capable of predicting the mode 1 stress intensity factor for the center cracked problem with far field tension.

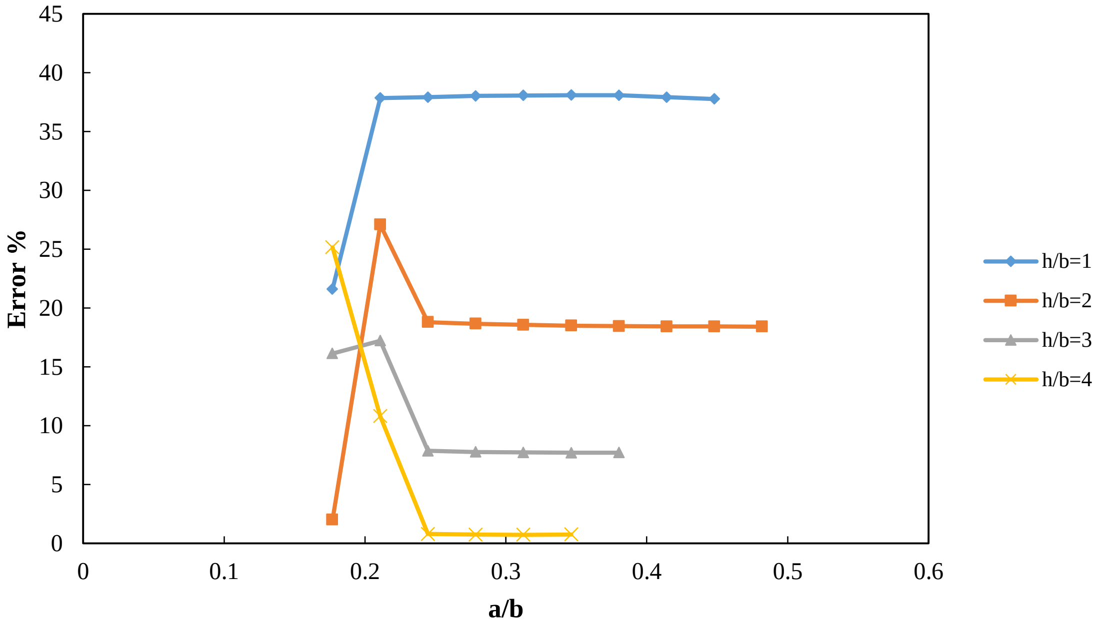

Figure 5-3 Error % of Mode 1 Stress Intensity factor between the analytical solution and the lattice model of the centered crack problem under tension.

Figure 5-4 compares the values of K_1 between the lattice and the analytical solutions for $h/b = 4$. Lattice model can accurately predict the mode 1 stress intensity factor values of the analytical solution for $a/b \geq 0.25$. As mentioned, the values of σ and a in Equation (5-8) have to be updated during the analysis as $\sigma = P/A$ where P is obtained from the load-displacement curve of the problem. Figure 5-5 also shows the tensile load-displacement curve of the lattice mesh shown in Figure 5-2 with $a =$

$0.8\ (in)$. The fracture energy release is illustrated in form of snap-back instabilities for the horizontally evolved crack.

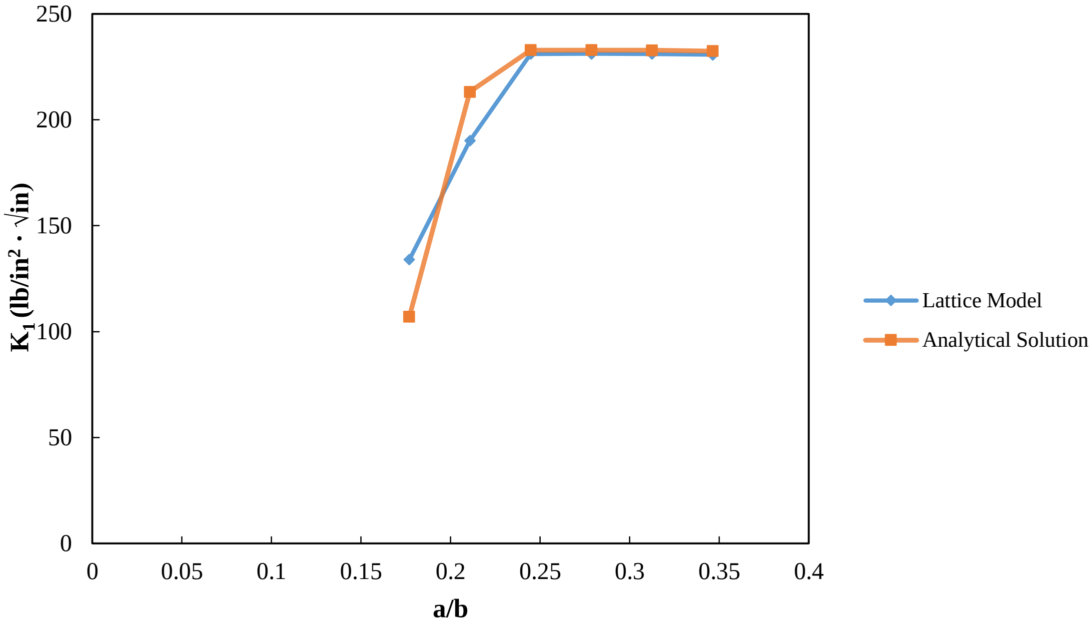

Figure 5-4 Comparison of K_1 between the lattice and analytical solution for the center cracked problem under tension ($h/b = 4$)

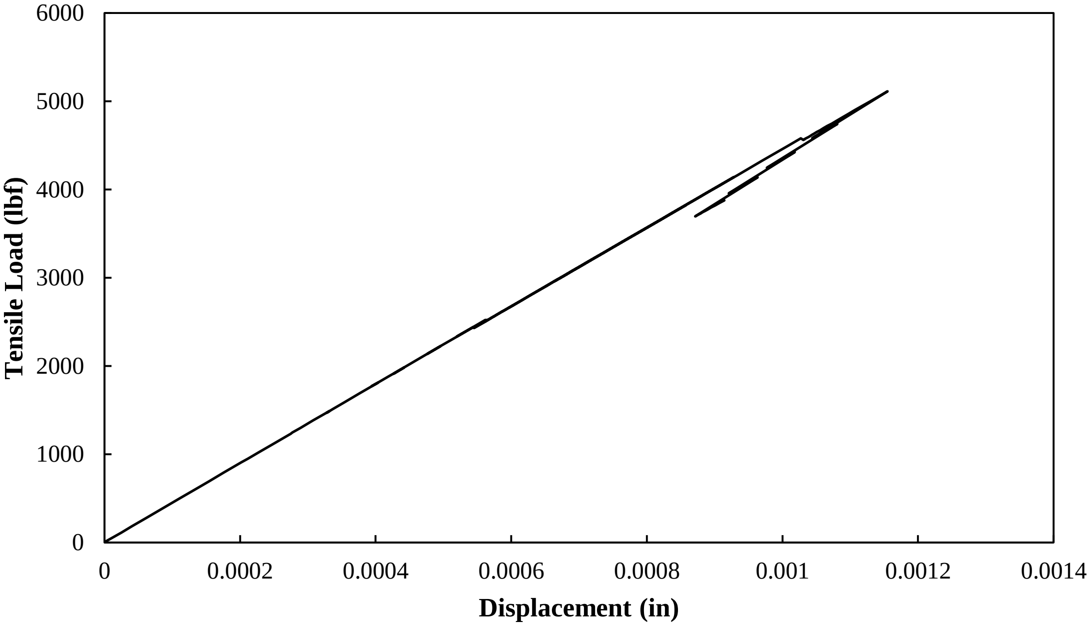

Figure 5-5 Load-Displacement of the tensile lattice mesh shown in Figure 5-2 for $h/b = 4$.

5.3 The Single Edge Notch Lattice Simulation

A single edge notch problem was also considered to evaluate the lattice model's results. Figure 5-6 shows the homogeneous finite width single edge notch test specimen with constant thickness on which a far field tensile stress is applied. Mode 1 crack tip stress intensity factor of this problem is again expressed as [62]

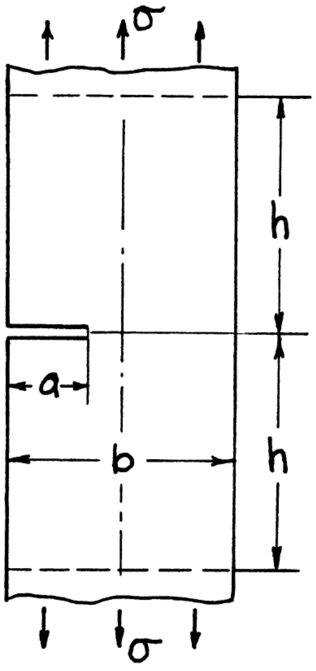

Figure 5-6 Homogeneous finite width single edge notch configuration with far field tension [62].

$$K_1 = \sigma\sqrt{\pi a}F(a/b), \tag{5-11}$$

where a is the edge crack length, σ is the tensile far field stress, b is the width of the plate or configuration as illustrated in Figure 5-6, and $F(a/b)$ may be expressed as [62]

$$F(a/b) = \sqrt{\frac{2b}{\pi a}\tan(\frac{\pi a}{2b})}.\frac{0.752+2.02(a/b)+0.37\left(1-\sin\left(\frac{\pi a}{2b}\right)\right)^3}{\cos\left(\frac{\pi a}{2b}\right)}\,. \tag{5-12}$$

Figure 5-7 shows the lattice mesh of the single edge notch configuration under direct tension as in Figure 5-6. This lattice mesh was simulated for five different ratios of $2h/b$. It is observed that as this ratio increases, the error percentage, defined in Equation (5-10), declines, as illustrated in Figure 5-8. As expected, the error for $2h/b = 5$ is the lowest which better simulates a farther tensile field than smaller ratios. However, the error percentage increases in all cases as the crack propagates through the configuration.

Figure 5-9 compares the values of K_1 between the lattice and the analytical solutions for $2h/b = 5$ for the single edge cracked problem. As it can be seen, the lattice model can accurately predict the mode 1 stress intensity factor values of the analytical solution with an error percentage of less than 3. As $2h/b$ increase, this error approaches zero for the lattice simulations. Again, the values of σ and a in Equation (5-11) have to be updated during the analysis.

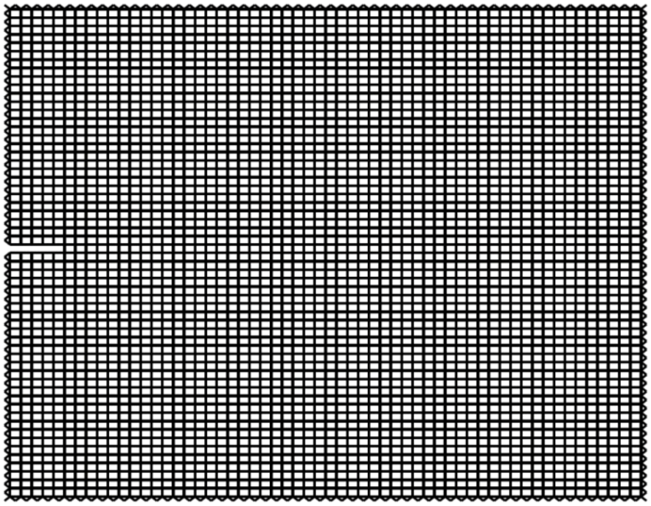

Figure 5-7 Homogeneous finite width single edge notch lattice mesh to determine the mode 1 stress intensity factor.

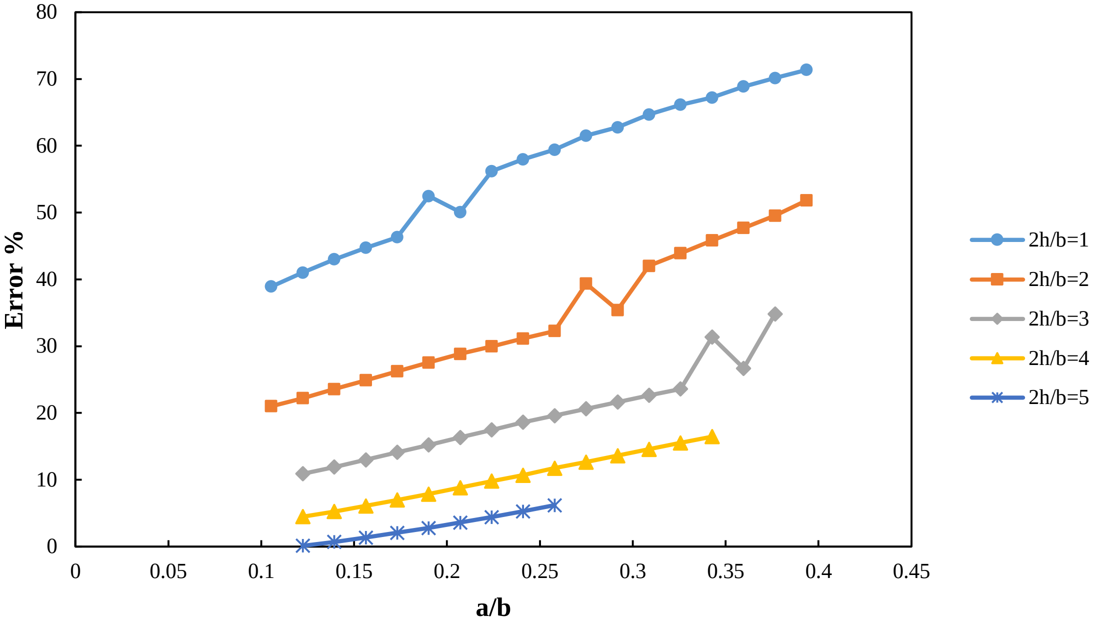

Figure 5-8 Error % of Mode 1 Stress Intensity factor between the analytical solution and the lattice model of the single edge notch problem under tension.

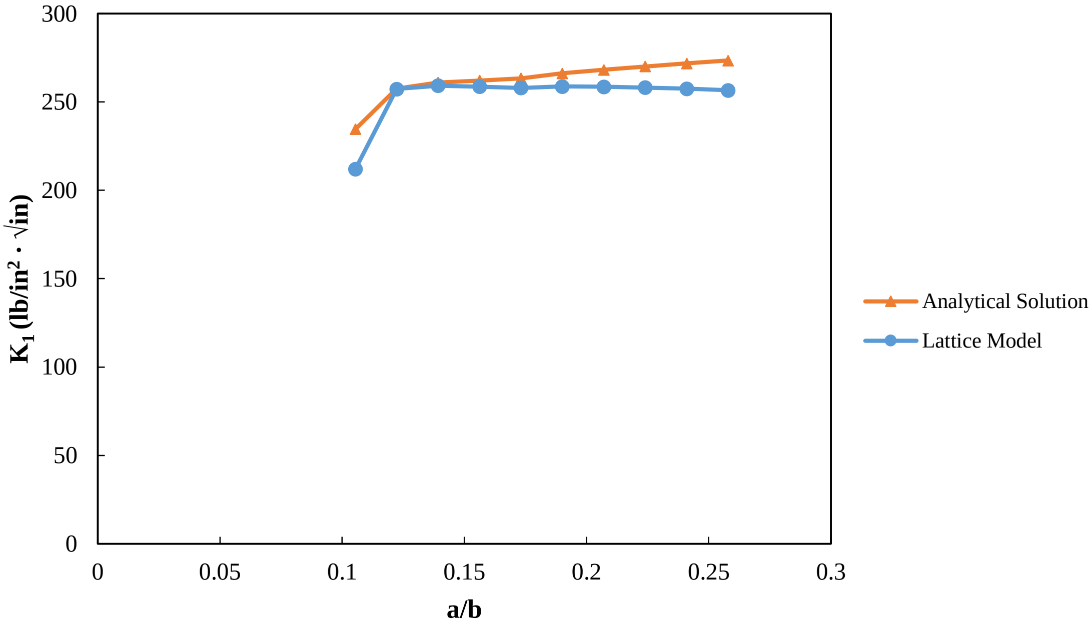

Figure 5-9 Comparison of K_1 between the lattice and analytical solution for the single edge notch problem under tension ($2h/b = 5$).

5.4 The Bi-material Interface Center Cracked Lattice Simulation

To motivate the application of the numerical lattice in characterizing the interface fracture properties of bi-material interfaces such as brick-mortar bond, it may be useful to simulate the bi-material interface center cracked problem. The problem of an isolated finite crack of length $L = 2a$ along the interface between two dissimilar elastic half-spaces subject to two remote stresses σ_{yy}^{∞} and σ_{xy}^{∞} was analytically solved. Figure 5-10 illustrates this bi-material interface crack problem.

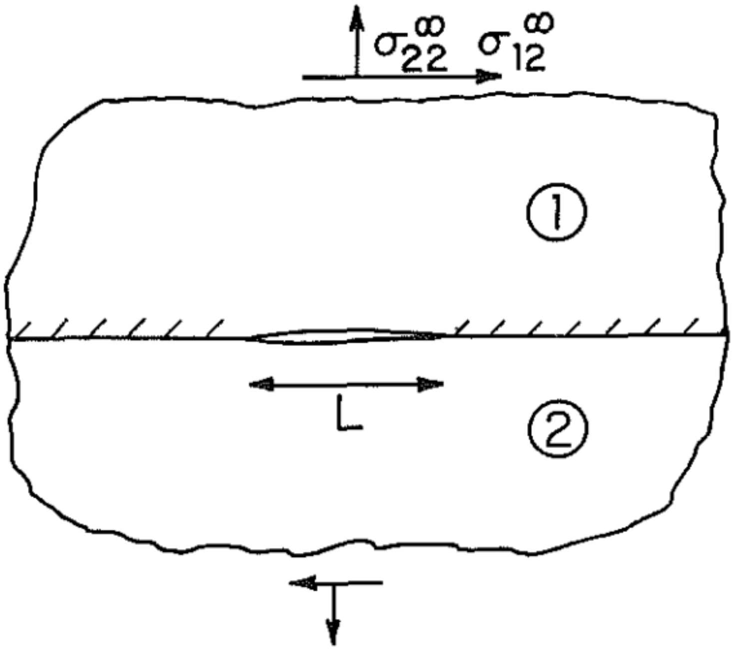

Figure 5-10 The bi-material interface isolated center cracked problem with remotely applied stresses [64].

The complex stress intensity factor at the right hand tip of the crack is expressed as [23], [64]

$$K = K_1 + iK_2 = (\sigma_{yy}^{\infty} + i\sigma_{xy}^{\infty})(1 + 2i\varepsilon)(\pi L/2)^{1/2} L^{-i\varepsilon} , \qquad (5\text{-}13)$$

where σ_{yy}^{∞} and σ_{xy}^{∞} are remotely applied stresses shown in Figure 5-10, ε is the bi-elastic constant defined in Equation (4-36), and $L = 2a$ is the crack length. When the configuration is only under direct tension, i.e., $\sigma_{xy}^{\infty} = 0$, (5-13) reduces to

$$K = K_1 + iK_2 = \sigma_{yy}^{\infty}(1 + 2i\varepsilon)(\pi L/2)^{1/2}L^{-i\varepsilon}. \tag{5-14}$$

Knowing that $\left|L^{i\varepsilon}\right| = 1$ and $\left|KL^{i\varepsilon}\right| = |K|$, the modulus of the complex K is obtained by

$$|K| = \sigma_{yy}^{\infty}\sqrt{\pi a(1 + 4\varepsilon^2)}, \tag{5-15}$$

which reduces to the well-known relation $\sigma_{yy}^{\infty}\sqrt{\pi a}$ in the absence of mismatch for an infinite plate. Figure 5-11 exhibits the lattice mesh with a center crack along the interface to simulate the modulus of K. The lattice has three phases of mortar, interface and brick which are illustrated by different colors of blue, pink, and black, respectively. Let L_x and L_y be the width and height of this domain, respectively.

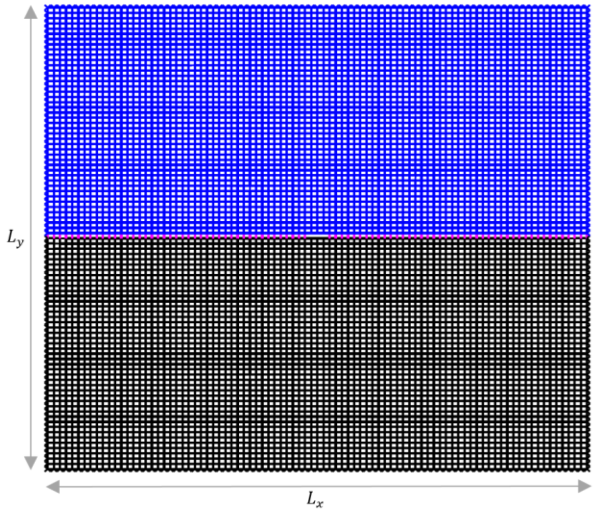

Figure 5-11 Heterogeneous bi-material interface center cracked lattice mesh under direct remote tension to determine the modulus of complex stress intensity factor at crack tip.

To simulate an infinite domain with an isolated crack along its interface, L_x and L_y have to be sufficiently large to account for the remotely applied stresses. The analysis was conducted for four different values of $L_x = L_y$. It was observed that by increasing these parameters in the lattice simulation of the problem the error percentage of $|K|$ drops down, indicating that the lattice model can fairly predict the energy release rate and stress intensity factors of bi-material interfaces (Figure 5-12). It is clear that by further increasing the values of $L_x = L_y$, this error much more decreases. It is seen in Figure 5-12 that the values of error oscillate for each set of $L_x = L_y \geq 20\ (in)$ when $2a/L_x$ is greater than a certain value.

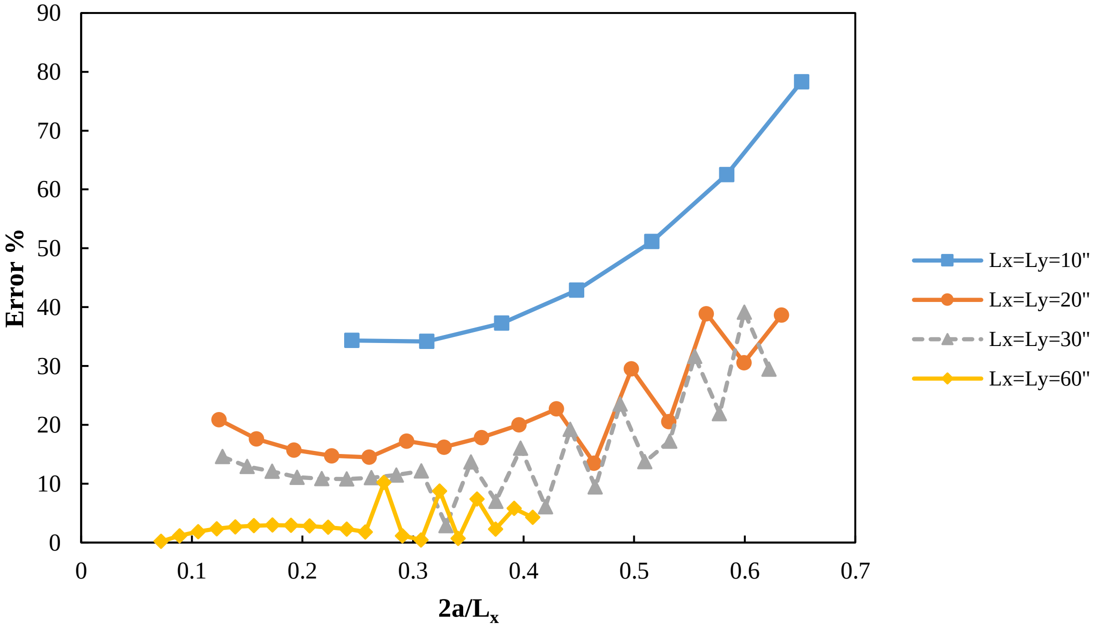

Figure 5-12 Error % of Stress Intensity factor moduli between the analytical solution and the lattice model of the bi-material interface center cracked problem under direct tension.

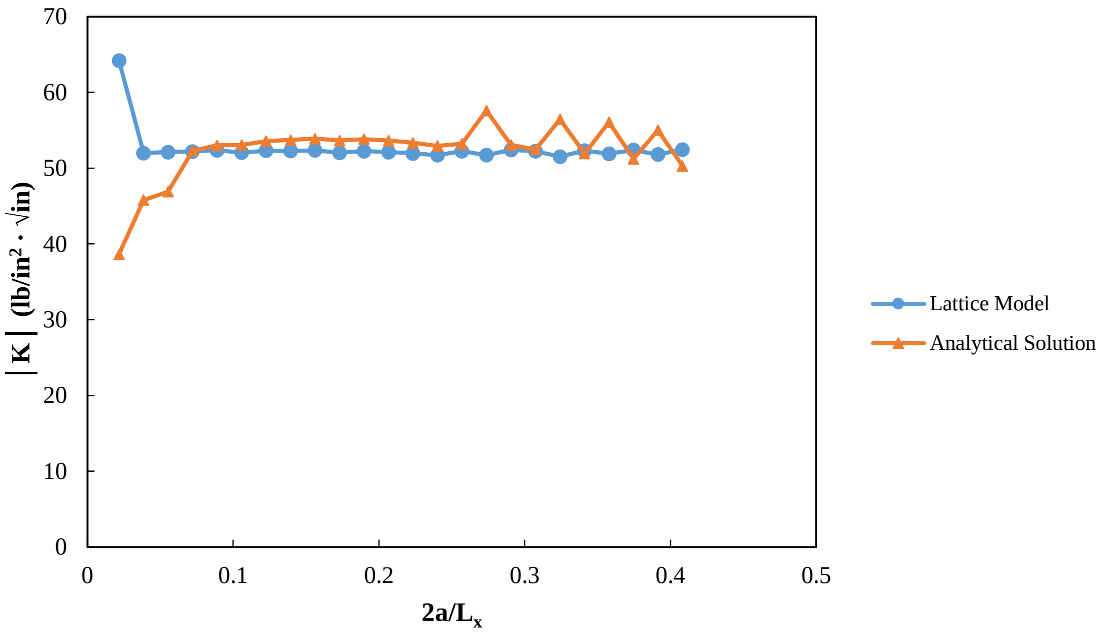

Figure 5-13 Comparison of $|K|$ *between the lattice and analytical solution for the bi-material interface center cracked problem under tension* ($L_x = L_y = 60\ (in)$)*.*

Moreover, Figure 5-13 compares the lattice simulation results with the analytical values determined by Equation (5-15) under direct tension, $\sigma_{xy}^{\infty} = 0$, as the crack propagates. The values of σ_{yy}^{∞} and a in this equation are determined by the lattice model at each increment. As a possible explanation, the oscillatory characters observed in Figure 5-12 and Figure 5-13 are probably due to the fact that when the length of the central crack is larger than a specific value for the finite width lattice mesh, shown in Figure 5-11, that crack is no longer considered a small crack in the lattice mesh compared to its dimensions, which is a required assumption in obtaining $|K|$ in (5-14). Figure 5-13 illustrates that the lattice can fairly predict $|K|$ of the bi-material interface center cracked problem with mostly an error of less than 3% for $L_x = L_y = 60\ (in)$. This error reduces for larger values of L_x and L_y.

5.5 Summary

The implemented 2D lattice model simulates crack path evolution in the form of strong discontinuities at a homogeneous or heterogeneous solid. Unlike the pre-cracked approach of the virtual crack extension procedure or the complicated XFEM, the lattice's relative simple theory and implementation makes it a promising method in solving crack problems in fracture mechanics. Three classic fracture mechanics problems were addressed in this chapter to validate the lattice fracture results. The center cracked problem in a homogeneous domain, the single edge notch problem in a homogeneous solid, and the center interface cracked problem in a bi-material system were solved by the numerical lattice.

The energy method was employed to obtain the energy release rate of the lattice mesh as the crack propagates. In the method, the energy released during the crack growth is mainly determined by considering the change in the global stiffness matrix of the mesh with respect to crack length change. Comparison of the analytical results of the three benchmark problems with the numerical solutions of the lattice for those problems validates the capability of the lattice in predicting the energy release rate and stress intensity factor of crack problems in homogeneous and heterogeneous solids. In all three cases, the lattice gives better results once the dimensions of the mesh are large enough to assure that the stresses are remotely applied.

Finally, it should be mentioned that the lattice square mesh was considered for fracture analyses of the crack problems rather than using random or regular triangular meshes. Unlike the random and regular triangular meshes which provide intrinsic angled or zigzag crack surfaces producing irregular oscillations in the values of energy release rate and stress intensity factor, the regular square mesh can generate straight crack surfaces along the interface which is itself an almost direct straight surface between brick and mortar. The irregular oscillations observed in the values of G and $|K|$ with the regular triangular mesh were discarded by using the square mesh. These oscillations have not been illustrated here for brevity.

Chapter 6 LATTICE SIMULATIONS OF INTERFACE FRACTURE IN MASONRY

In the previous chapter, some classic fracture mechanics problems were solved by the numerical lattice model to obtain the energy release rate and crack tip stress intensity factor. The lattice numerical results were validated by comparing with those of the analytical relations. In this chapter, some common masonry test specimens are simulated to determine their interface fracture quantities. Three types of lattice simulations were performed to obtain the energy release rate and fracture properties of brick-mortar interface. They include (i) a symmetric pre-notched bi-material four-point bending simulation as shown in Figure 6-1, (ii) a direct tension test for mode 1 behavior of the interface, and (iii) an unconfined triplet test to evaluate the interfacial behavior in mode 2. Taking advantage of these simulations' results, one may obtain the interface toughness relation which is interface resistance against failure. It is believed that defining a measurable and usable material property, i.e., toughness, to parameterize fracture resistance of interfaces may be the purpose of the interfacial fracture mechanics [65]. This goal is achieved by using the lattice to solve for bi-material systems where a crack is driven along their interface. Not only is this approach applicable to masonry interfaces, but also any bi-material interface problem may be solved using the implemented lattice.

This numerical tool can also be employed to characterize the post-peak fracture energy of cohesive zone models in the form of bi-linear traction-separation laws in meso scale of continuum finite element. It is very challenging to experimentally measure this fracture energy of cohesive zones where a sudden rupture usually happens once the driving force suppresses the toughness of the bi-material interface. Moreover, the lattice may serve to homogenize a masonry unit cell comprising brick, mortar, and interface into a homogeneous isotropic finite element with an equivalent Young's modulus, load capacity, and dissipated strain energy for the post-peak behavior.

6.1 Four-Point Bending Simulation

This test specimen which is capable of measuring the fracture resistance of bi-material interfaces was first introduced by Charalambides et al [28]. Figure 6-1 illustrates the test configuration with a notch through the upper layer at the center. A pre-crack of length $2a$ is also introduced before applying the load.

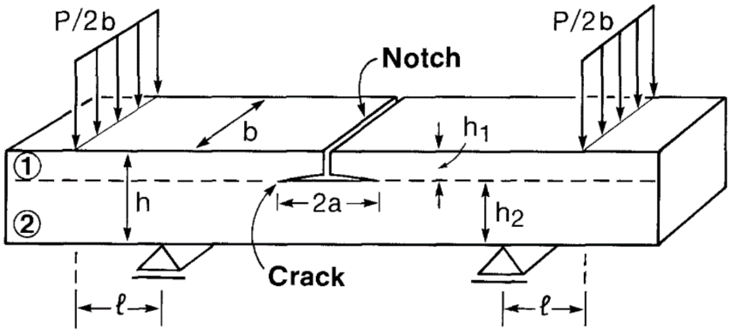

Figure 6-1 The pre-notched bi-material four-point bending beam with two symmetrical interfacial cracks [28]

This test configuration was simulated by the lattice model to evaluate the interface fracture properties during the progressive crack evolution. Because of the symmetry, only one half of the four-point bending beam was accepted in the lattice simulation. For the interface to experience enough length of debonding and delamination, a beam length of $16\ (in)$ with $l = 1\ (in)$ and loading points' distance of

15 (in) was considered for the simulations. These parameters are shown in Figure 6-1. A mortar layer of 1.5 (in) was overlaid on a brick layer of 1 (in) thick. Since the crack propagates into the brick layer at early stages of the simulation when the thickness of brick is greater than that of mortar, a thicker mortar layer was considered in this study for the four-point bending simulation as it results in an interface crack propagation during the analysis which was the main purpose of the simulation to get the interface fracture properties.

An analysis was conducted to select the type of mesh and a regular square mesh gave more consistent results than regular triangular and random meshes. This is probably due to the fact that in a regular square mesh, the crack flanks behind the tip in the continuum mesh are straight surfaces while in a regular triangular mesh with the hexagonal configuration of the continuum mesh, Figure 3-1, the crack surfaces have a zigzag pattern affecting the results of interfacial energy release rate and other fracture quantities.

Figure 6-2 illustrates the lattice mesh and the boundary conditions of the notched symmetric composite beam under the four-point bending used in the lattice analysis. Since the top layer above the crack includes a notch, it is essentially stress free experiencing rigid body motion behind the crack tip. Moreover, because of both opening and sliding of the upper mortar layer relative to the lower brick layer, there is a mixed mode failure in the interface. As it is seen in this figure, the interface struts are failed in an unzipping manner all the way to a region close to the support. Figure 6-3 exhibits the global load-displacement curve of the lattice beam shown in Figure 6-2 under four-point bending boundary conditions as the crack propagates along the interface. The curve experiences a ductile deformation due to the unzipping failure of the interface followed by a hardening part when the crack approaches along the interface to the region close to the roller support.

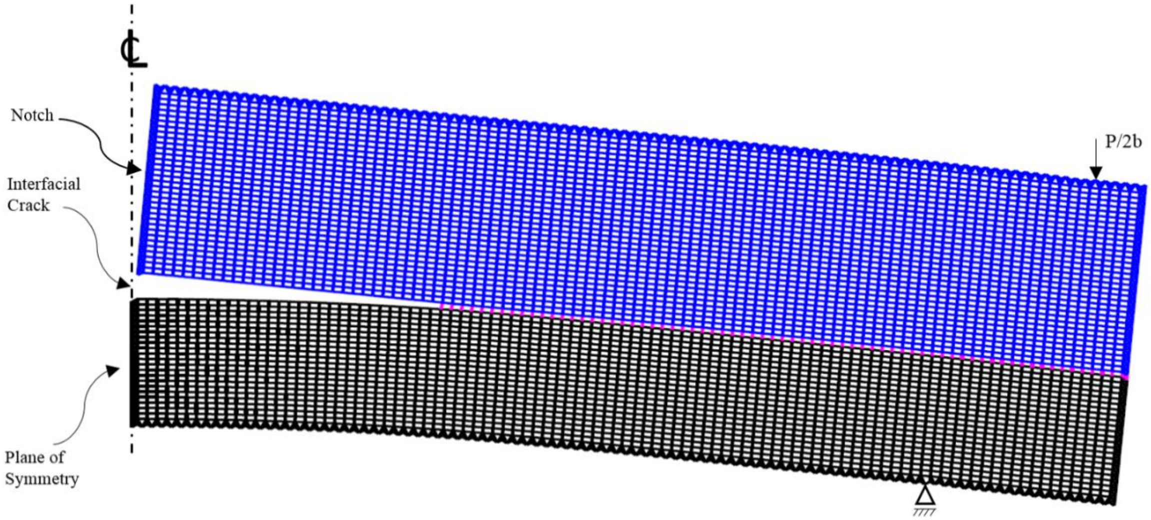

Figure 6-2 The lattice mesh and the boundary conditions of a notched symmetric composite beam used in the lattice analysis under the four-point bending. This figure belongs to an increment with a propagated crack during the analysis.

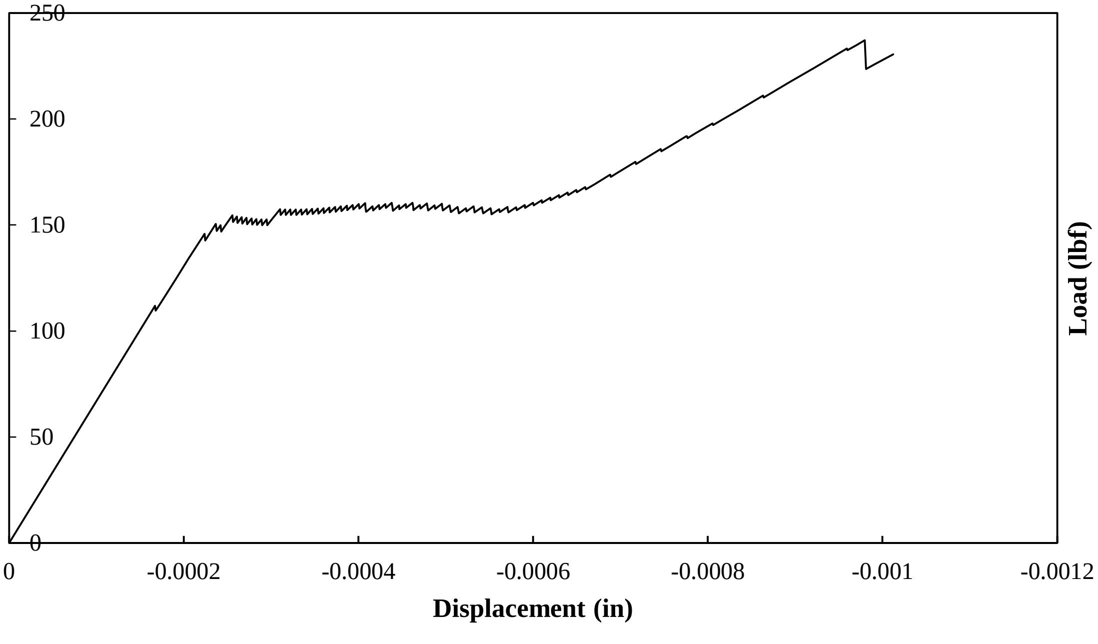

Figure 6-3 Load-displacement curve of the four-point bending lattice simulation shown in Figure 6-2.

Figure 6-4 to Figure 6-7 show the fracture results of the lattice configuration shown in Figure 6-2. The energy release rate, G, and the augmented loading phase angle, $\hat{\psi}$, were calculated in the lattice according to Equations (5-6) and (4-51), respectively. It is interesting to note that the loading phase angle, $\hat{\psi}$, is insensitive to the distance from the crack tip, r, as shown in Figure 6-5, which makes the fracture quantities of mode 1 and mode 2, e.g., the stress intensity factor and the fracture energy, independent of distance r. Also, $b_t = 2S_x$ in the legend of Figure 6-5 where S_x was defined in Figure 3-4. In Figure 6-4, some points on the graph of G and consequently K_1 and K_2 have lower values especially for $2.3 \leq a \leq 4.7$ (in), resulting in stepwise oscillations. These points are related to those interface elements which fail 'immediately' after the failure of the previous neighboring interface strut, resulting in a lower load value in the load-displacement diagram.

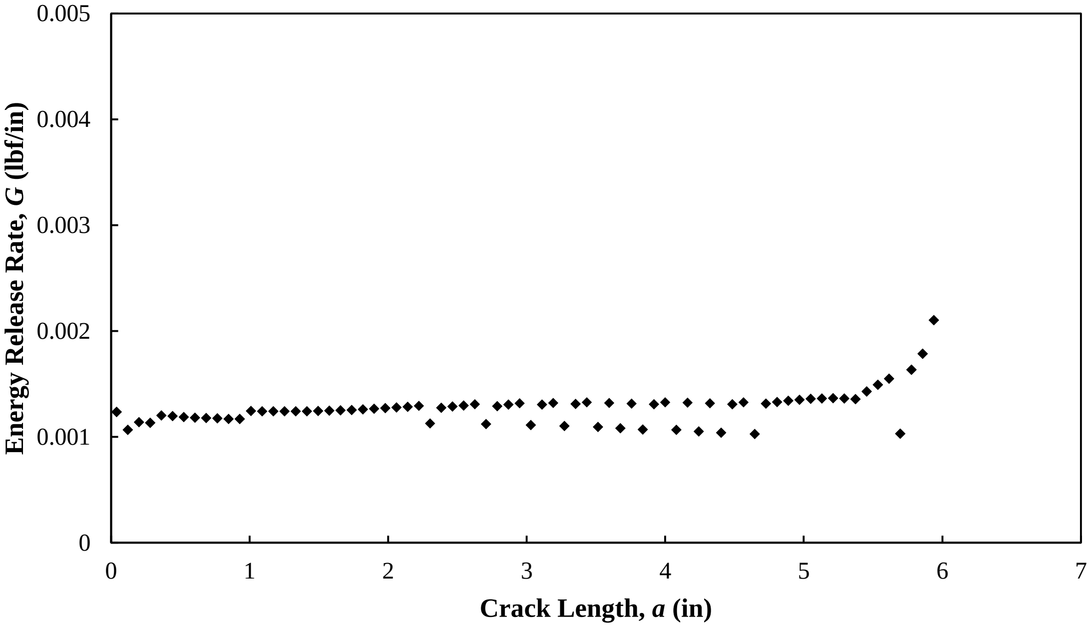

Figure 6-4 The energy release rate, G, with respect to crack length for the four-point bending simulation results from lattice analysis.

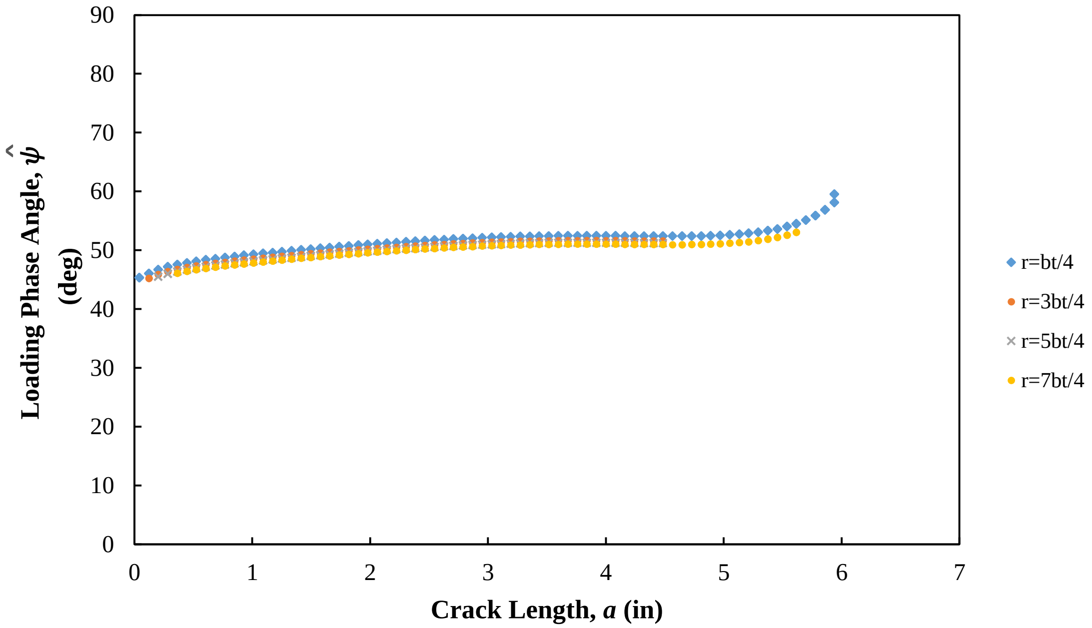

Figure 6-5 The loading phase angle, $\hat{\psi}$, of the four-point bending at different distances from the tip with respect to crack length.

As shown in Figure 6-5, the distribution of the phase angle, $\hat{\psi}$, varies between 45° and 55°, meaning that the fracture is a mixed mode, as $\hat{\psi} = 0^{\circ}$ and $\hat{\psi} = 90^{\circ}$ indicate pure mode 1 and pure mode 2, respectively. $\hat{\psi}$ tends to slightly go up for $a > 5\ (in)$ implying that the interface mode 2 failure is more prominent since the crack tip along the interface is approaching to the region in the proximity of the roller support. It should be mentioned that the deformations in the deformed mesh of Figure 6-2 have been magnified by a factor of 300. It is obvious that the interface struts at the center of the beam have smaller horizontal component of deformation than those which are close to the roller support. Figure 6-6 and Figure 6-7 also show the variations of stress intensity factors for mode 1 and mode 2. Consistent with the loading phase angle values, K_1 and K_2 represent that the interface struts at the center of the beam experience a mixed mode failure with almost the same contribution of mode 1 and 2 while the influence of mode 2 failure increases as the crack grows.

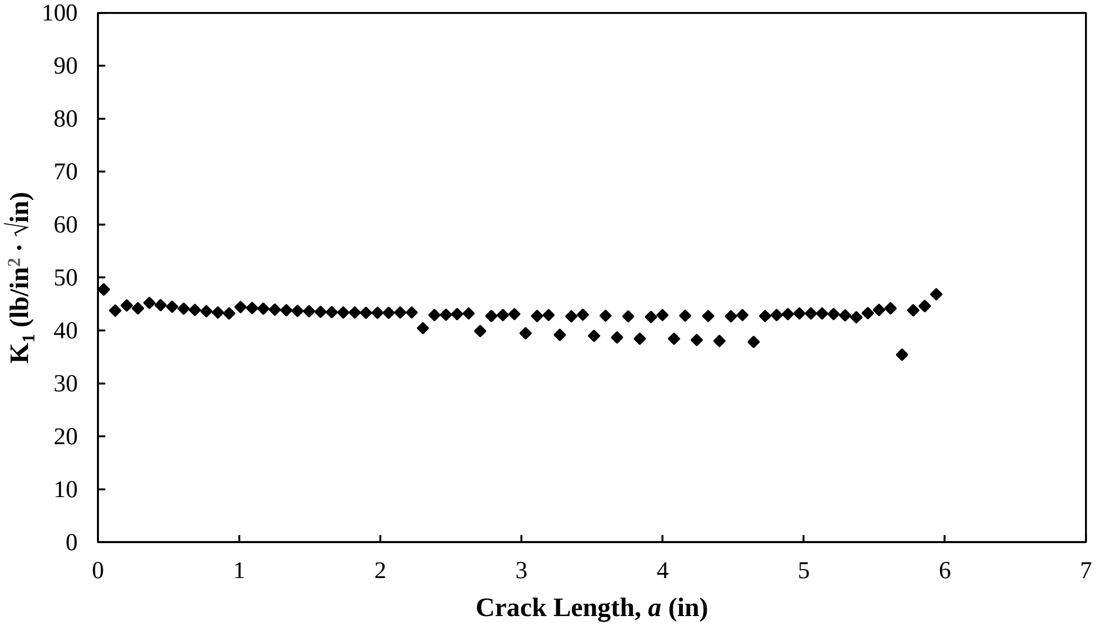

Figure 6-6 Mode 1 stress intensity factor for the four-point bending lattice simulation.

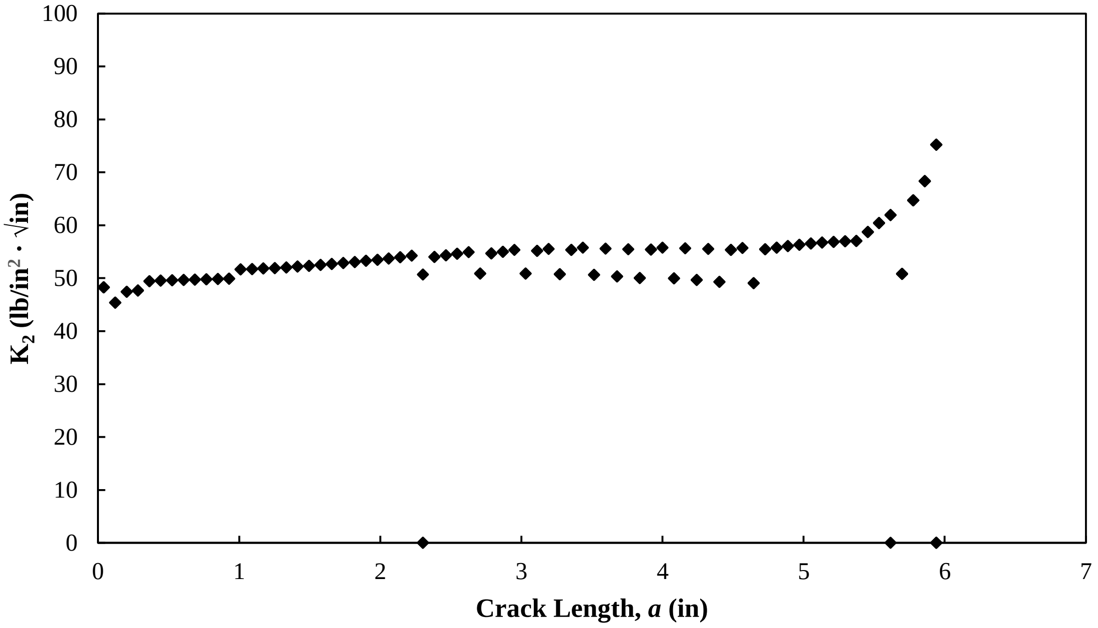

Figure 6-7 Mode 1 stress intensity factor for the four-point bending lattice simulation.

6.2 Tension Simulation

The global behavior of this simulation was discussed in Section 3.5.1 where the load-displacement curve of the regular triangular mesh was only evaluated. In this section, the fracture properties of the crack tip is considered. As mentioned before, the regular square mesh gives better results in terms of fracture quantities. Thus, similar to Section 6.1, a numerical lattice simulation was conducted on the tensile behavior of the brick-mortar interface. The boundary condition and configuration of the tensile simulation is shown in Figure 6-8 with a propagated crack at one interface. The fracture properties of this simulation are illustrated in Figure 6-9 to Figure 6-12. This analysis provides steady state values for the energy release rates of the interface as the crack propagates.

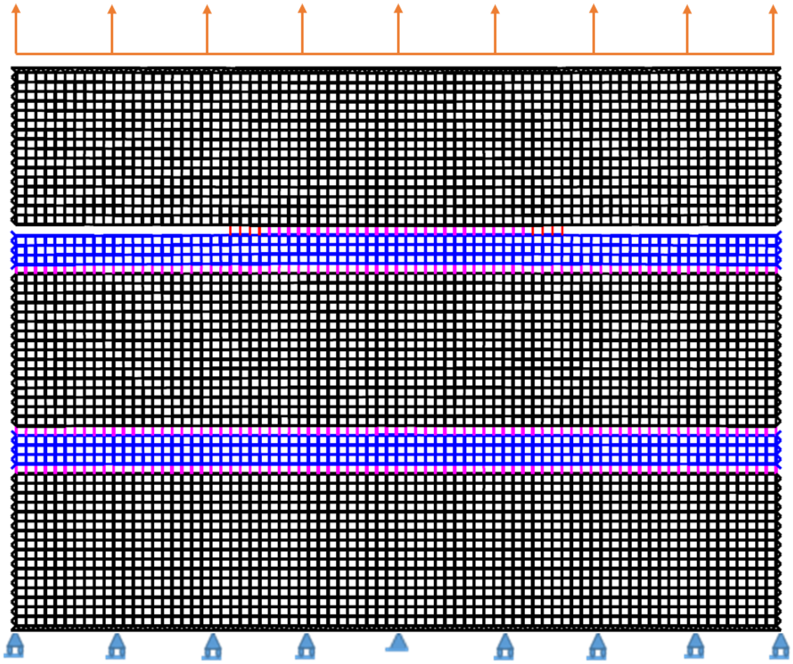

Figure 6-8 The lattice mesh and boundary conditions of a masonry configuration used in the lattice analysis of the direct tensile simulation. This figure belongs to an increment with a propagated crack during the analysis.

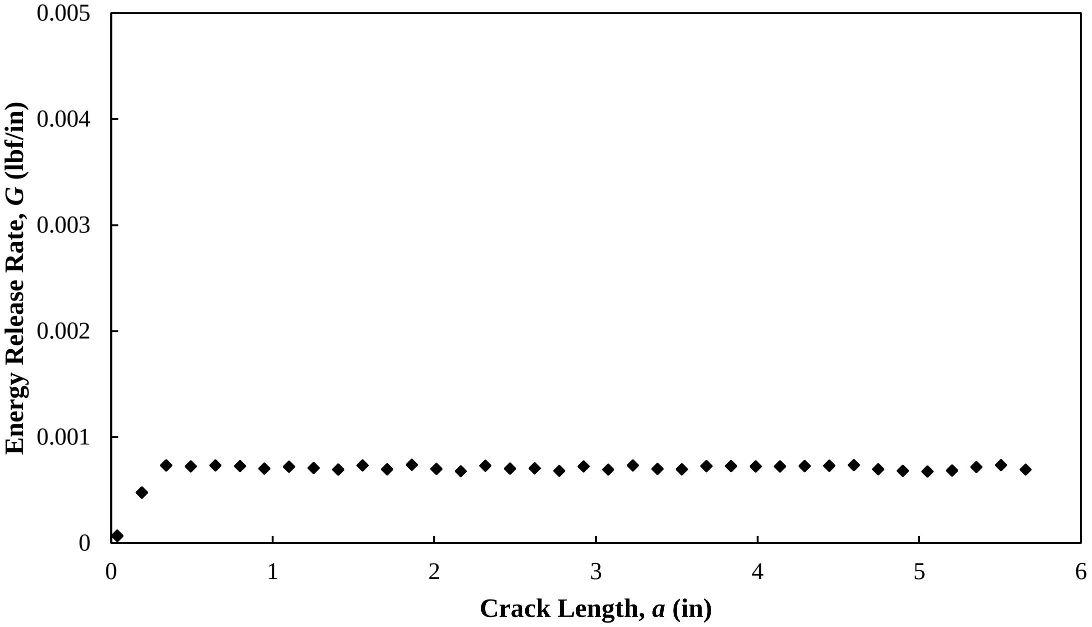

Figure 6-9 The energy release rate, G, with respect to crack length for the tension simulation results from lattice analysis.

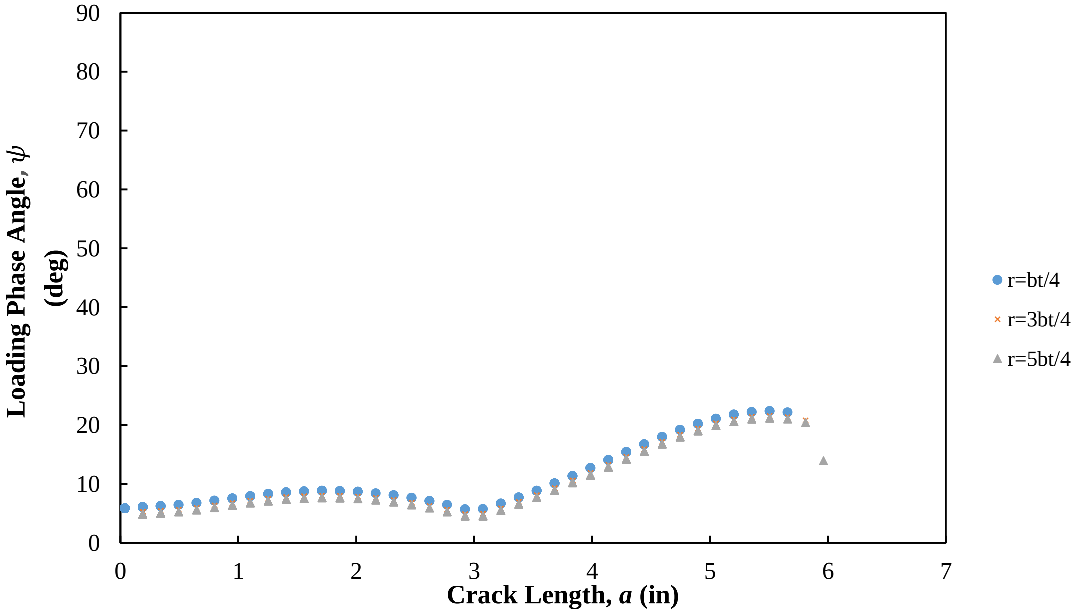

Figure 6-10 The loading phase angle, $\hat{\psi}$, of the tension simulation at different distances from the tip with respect to crack length.

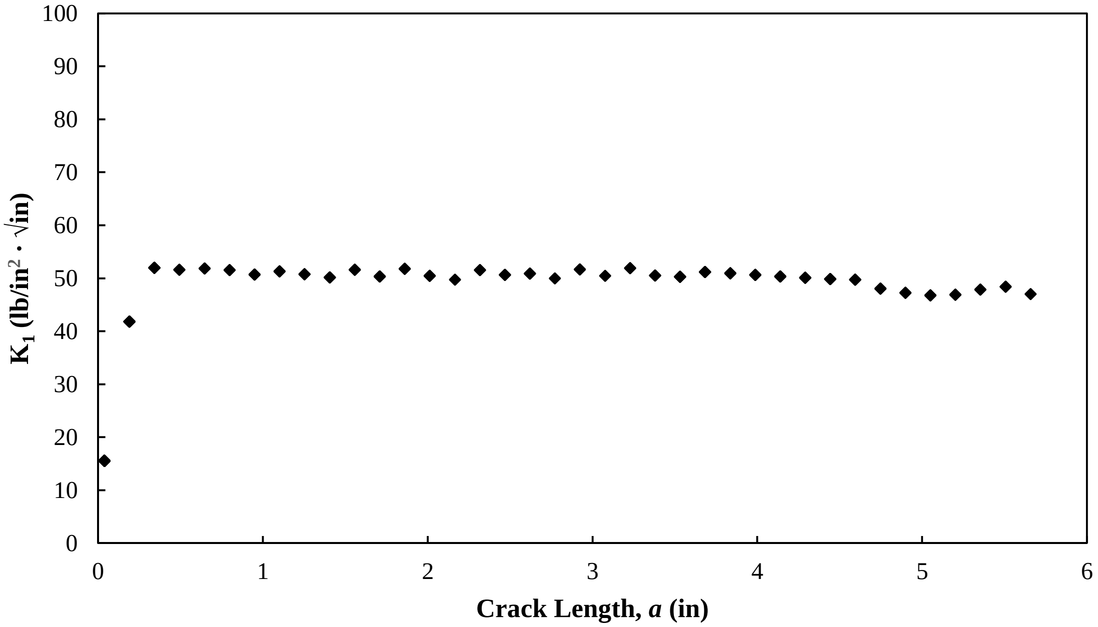

Figure 6-11 Mode 1 stress intensity factor for the tension lattice simulation.

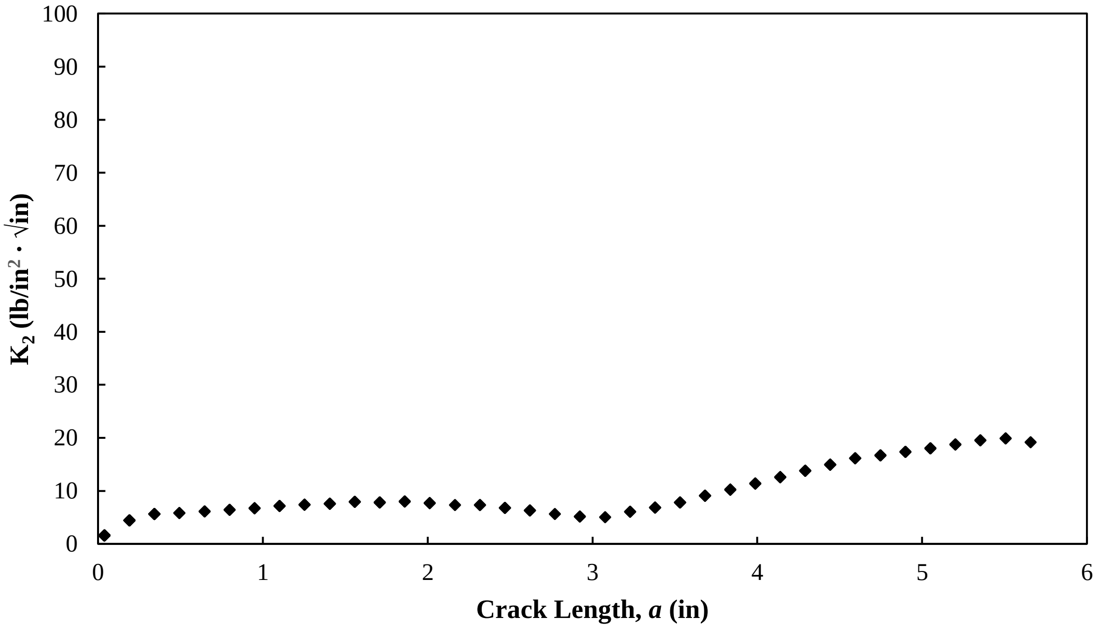

Figure 6-12 Mode 2 stress intensity factor for the tension lattice simulation.

The energy release rate is fairly constant as the tensile crack evolves through the interface, as shown in Figure 6-9. Comparing Figure 6-11 and Figure 6-12 indicates that the major contributing mode in the interface failure is mode 1, as expected. The loading phase angle, $\hat{\psi}$, is again fairly insensitive to the distance from the crack tip as exhibited in Figure 6-10. The values of $\hat{\psi}$ also confirms that the interface failure is dominated by the mode 1. The uniform constant values of G as crack length increases makes it possible to extract an average value of energy release rate or dissipated strain energy which could be employed in cohesive zone models which will be explained in Section 6.6.

6.3 Unconfined Triplet Simulation

The unconfined triplet test which is a double lap shear test in masonry studies was considered for the lattice simulations. Figure 6-13 shows the triplet boundary conditions with the propagated crack length of delamination from the lattice analysis.

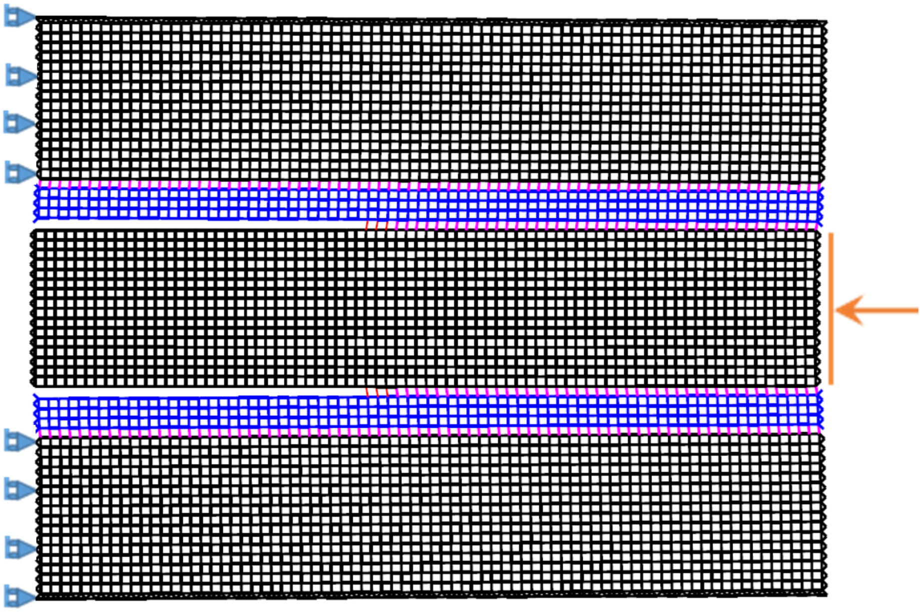

Figure 6-13 The lattice mesh and the boundary conditions of a triplet configuration used in the lattice analysis of the unconfined triplet simulation. This figure belongs to an increment with a propagated crack during the analysis.

Figure 6-14 to Figure 6-17 show the fracture results of the lattice configuration shown in Figure 6-13. Figure 6-14 illustrates the variation of G with respect to the crack length for one interface, which exhibits a constant steady-state trend. Again, each point on this graph is related to the failure of one strut at the cohesive zone. In Figure 6-15, the variation of $\widehat{\psi}$ at different distances from the crack tip, r, is shown, which is insensitive to this distance. This feature is promising in decomposing the energy release rate and the modulus of stress intensity factor into mode 1 and mode 2. Figure 6-16 and Figure 6-17 compare the stress intensity factors for mode 1 and 2, respectively. As shown, the unconfined triplet simulation indicates that this is not a pure shear process since there are some values on Figure 6-16 for mode 1 separation. However, the shear failure is dominant as compared to the tension.

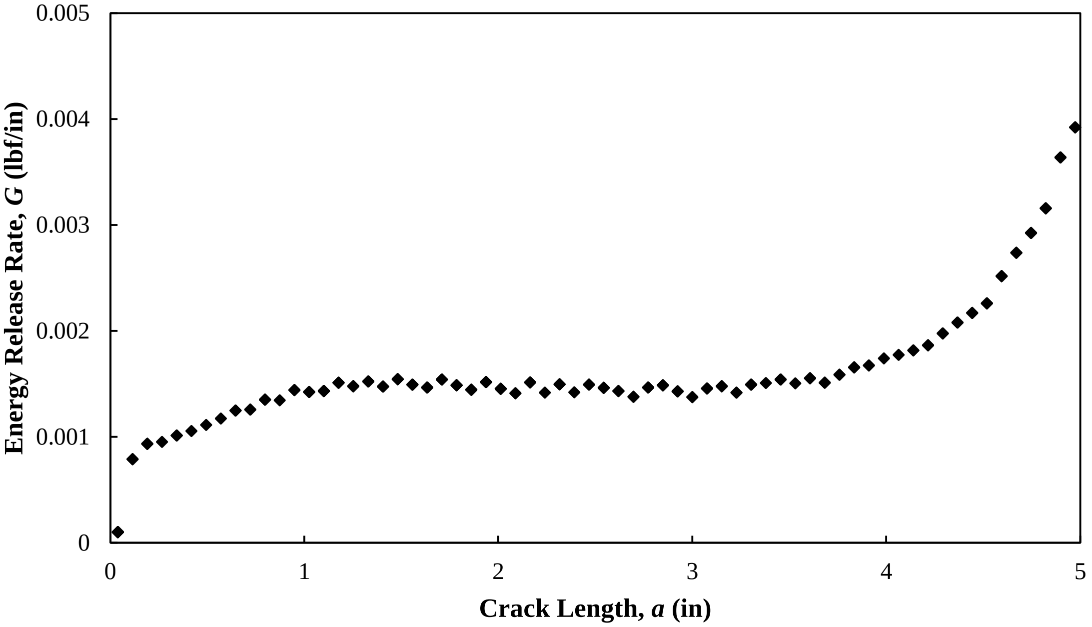

Figure 6-14 The energy release rate, G, with respect to crack length for the triplet simulation results from lattice analysis.

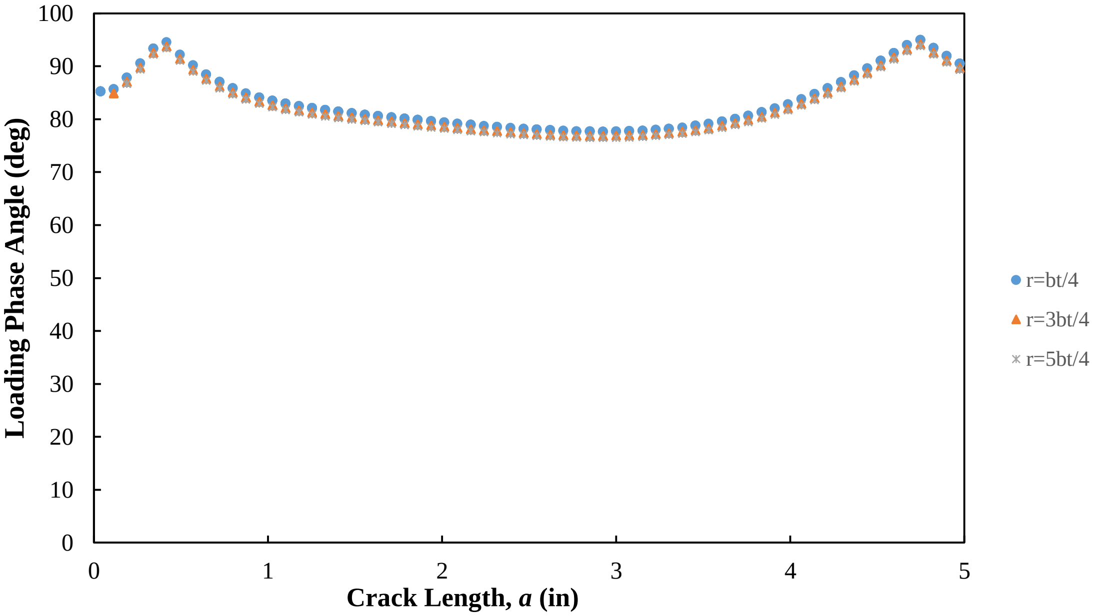

Figure 6-15 The loading phase angle, $\hat{\psi}$, of the tension simulation at different distances from the tip with respect to crack length.

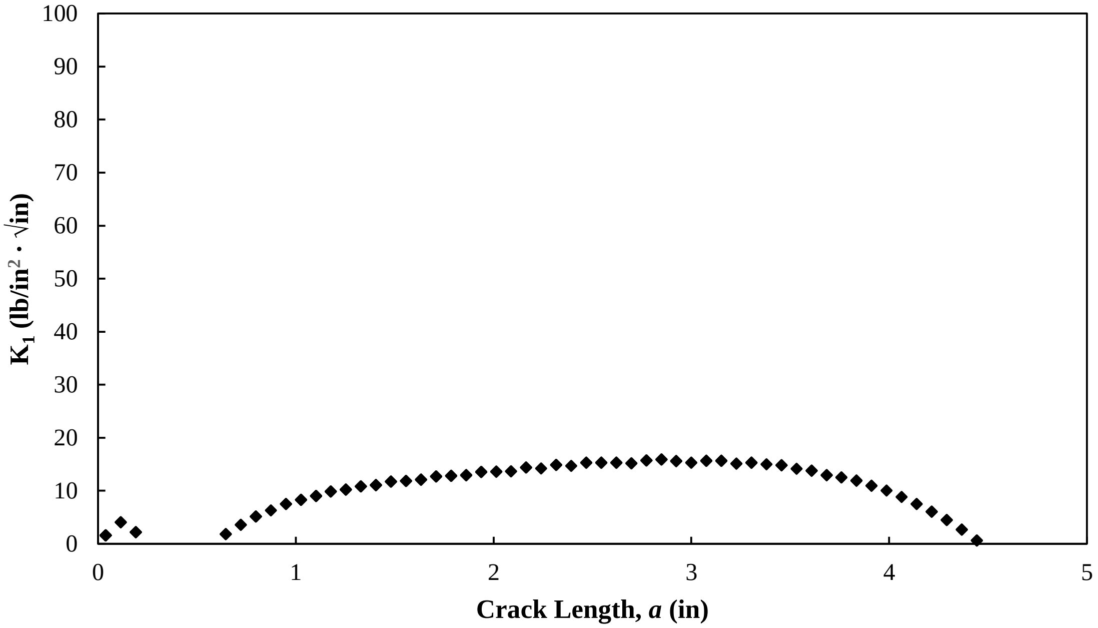

Figure 6-16 Mode 1 stress intensity factor for the triplet lattice simulation.

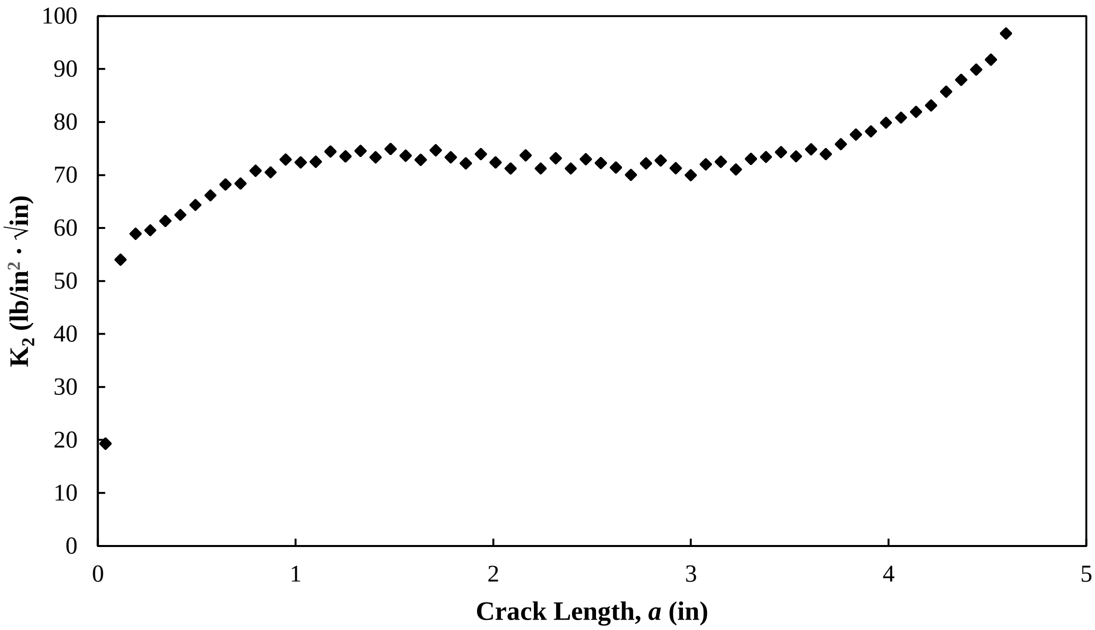

Figure 6-17 Mode 2 stress intensity factor for the triplet lattice simulation.

6.4 Mesh Sensitivity

In order to investigate the effect of mesh refinement on the fracture properties of the interface crack tip, two different meshes were analyzed for each of the three test configurations explained in Sections 6.1 to 6.3. Table 6-1 presents the total number of frame elements and equations for the fine and coarse meshes considered for the three simulation specimens. For the four-point bending mesh, the total number of elements in the fine mesh is about five times as great as the numbers in the coarse mesh while for the tension and triplet simulations this number is approximately four. Figure 6-2, Figure 6-8, and Figure 6-13 illustrate the fine meshes mentioned in Table 6-1 for the four-point bending, tension, and unconfined triplet simulations, respectively. The mesh sensitivity analysis was conducted for the four-point bending simulation for the fine and coarse mesh in Table 6-1. Figure 6-18 and Figure 6-19 illustrate the change in the energy release rate and the loading phase angle in terms of crack length.

Table 6-1 Mesh refinement properties of the three simulations conducted by the lattice

Simulation Configuration Type	**Fine Mesh**		**Coarse Mesh**	
	Nele[1]	**NEqns**[2]	**Nele**	**NEqns**
Four-Point Bending	12466	18419	2596	3773
Tension	9890	14730	2540	3760
Unconfined Triplet	9890	14775	2540	3781

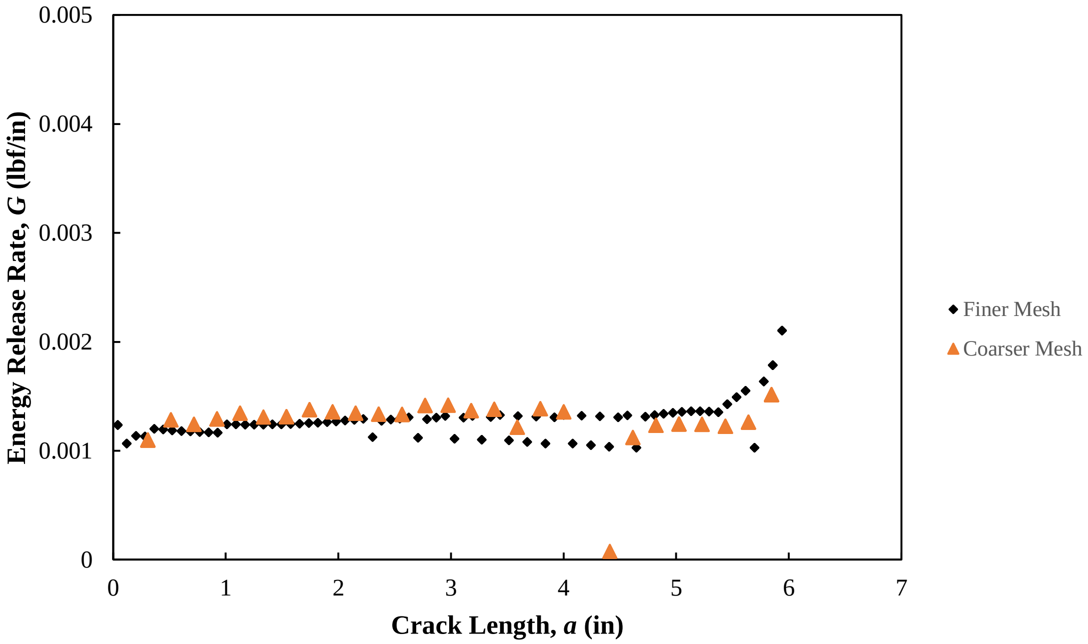

Figure 6-18 Variation of the energy release rate with respect to crack length for the fine and coarse mesh of the four-point bending simulation.

---

[1] Number of elements in the lattice mesh.
[2] Number of equations in the lattice mesh.

As shown in Figure 6-18, the mesh refinement has slight influence on the values of G as crack propagates while $\hat{\psi}$ experiences a small reduction from the coarser to the finer mesh for the pre-notched four-point bending beam. This difference increases with the growth of the crack length, a.

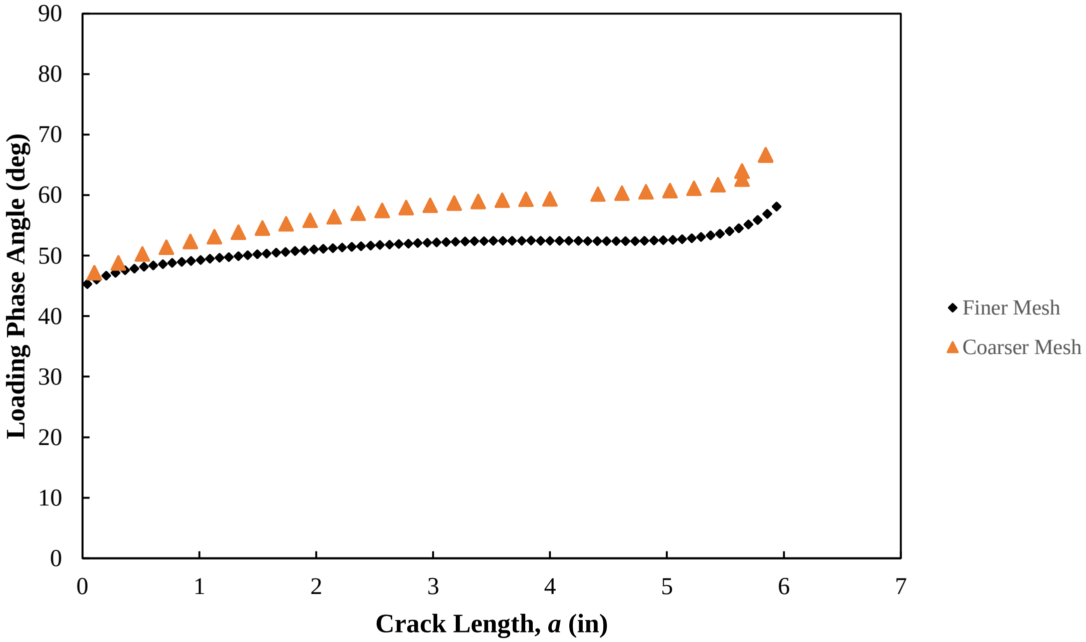

Figure 6-19 Variation of the loading phase angle, $\hat{\psi}$, with respect to crack length for the fine and coarse mesh of the four-point bending simulation.

The mesh sensitivity of the lattice simulation was also examined for the case of direct tension. Figure 6-20 compares the variation of the energy release rate of the fine mesh with that of the coarse mesh for the direct tension simulation. It is seen that the lattice results for G are insensitive to the mesh refinement for the tension specimen. The value of G is also steady constant during the crack evolution indicating a stable crack propagation for the brick-mortar interface. Furthermore, Figure 6-21 exhibits the variation of the loading phase angle, $\hat{\psi}$, for the fine and coarse mesh with the crack growth for the direct tension simulation. The refinement of the lattice mesh does not considerably affect the values of $\hat{\psi}$ which is a remarkable feature of the lattice model. There is an increase in $\hat{\psi}$ for $a > 3\ (in)$ which may be due to the deformation of the top brick in Figure 6-8, imposing larger horizontal displacements to the interface struts which is then translated into higher mode 2 failure.

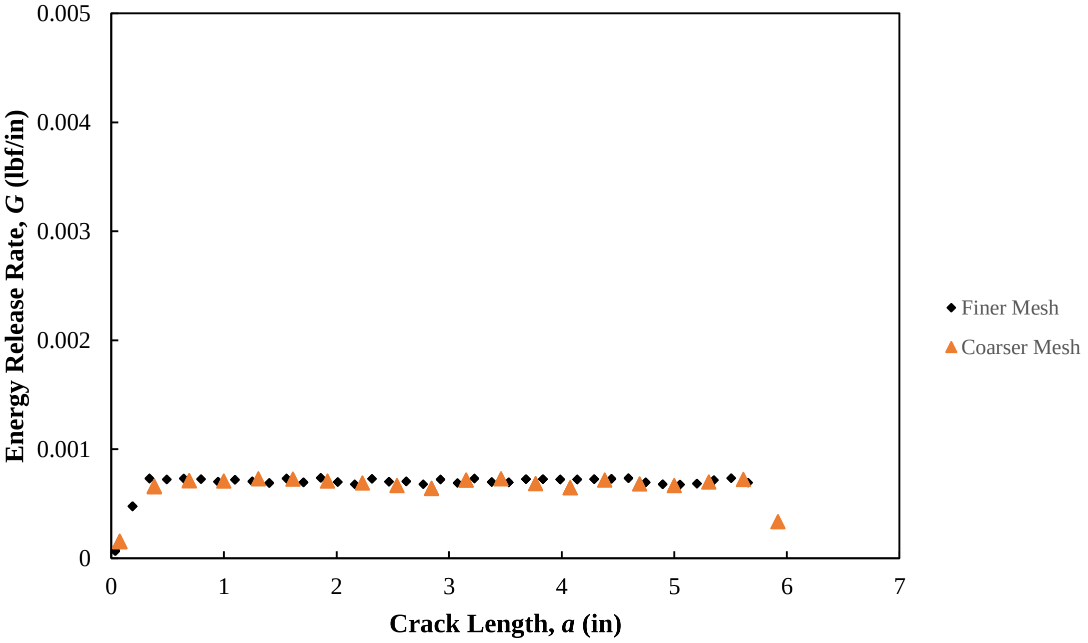

Figure 6-20 Variation of the energy release rate with respect to crack length for the fine and coarse mesh of the direct tension simulation.

Figure 6-22 and Figure 6-23 compare the fine mesh energy release rate and the loading phase angle with those of the coarse mesh for the unconfined triplet simulation. The values of energy release rate are fairly insensitive to the mesh refinement, while the loading phase angle of the fine mesh is slightly different from that of the coarse mesh. However, this small difference may be neglected. In sum, it may be concluded that the lattice model's interfacial fracture quantities are fairly insensitive to the mesh size which may be considered as a useful feature of the implemented lattice.

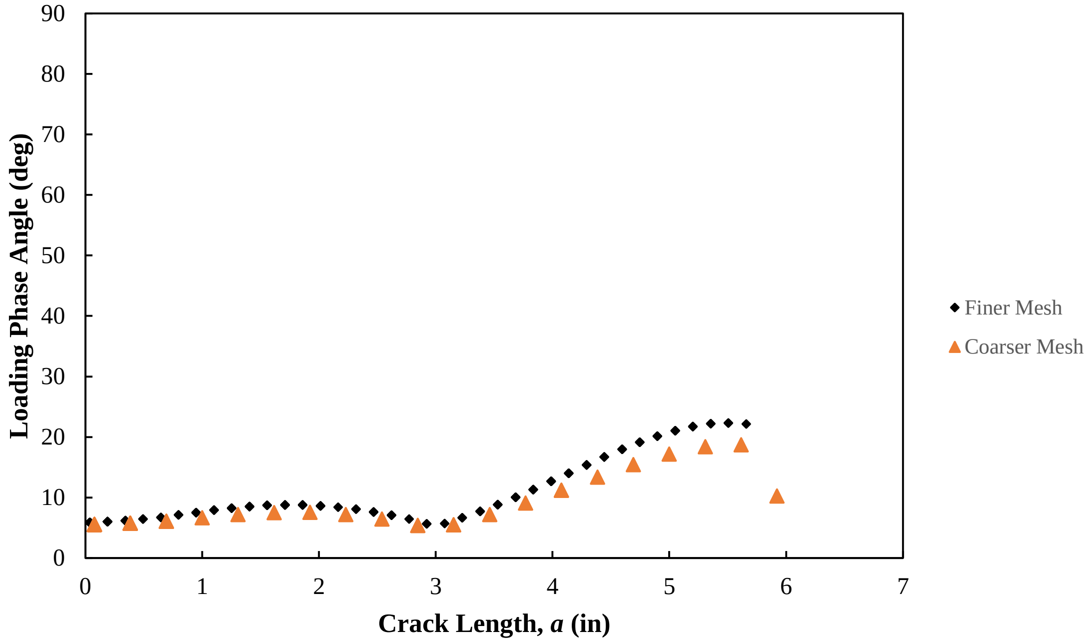

Figure 6-21 Variation of the loading phase angle, $\hat{\psi}$, with respect to crack length for the fine and coarse mesh of the direct tension simulation.

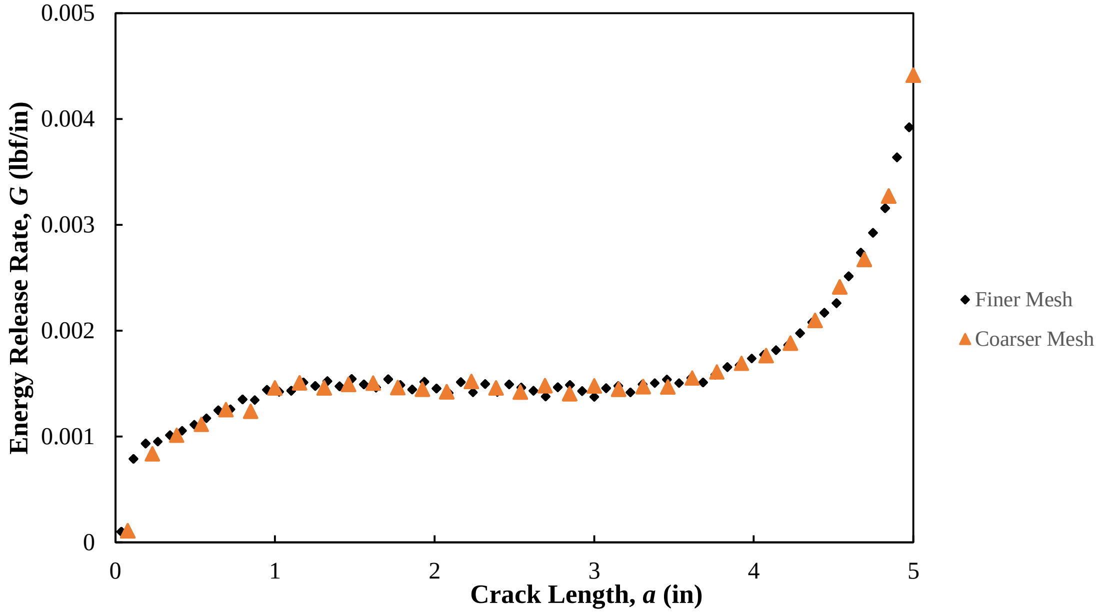

Figure 6-22 Variation of the energy release rate with respect to crack length for the fine and coarse mesh of the unconfined triplet simulation.

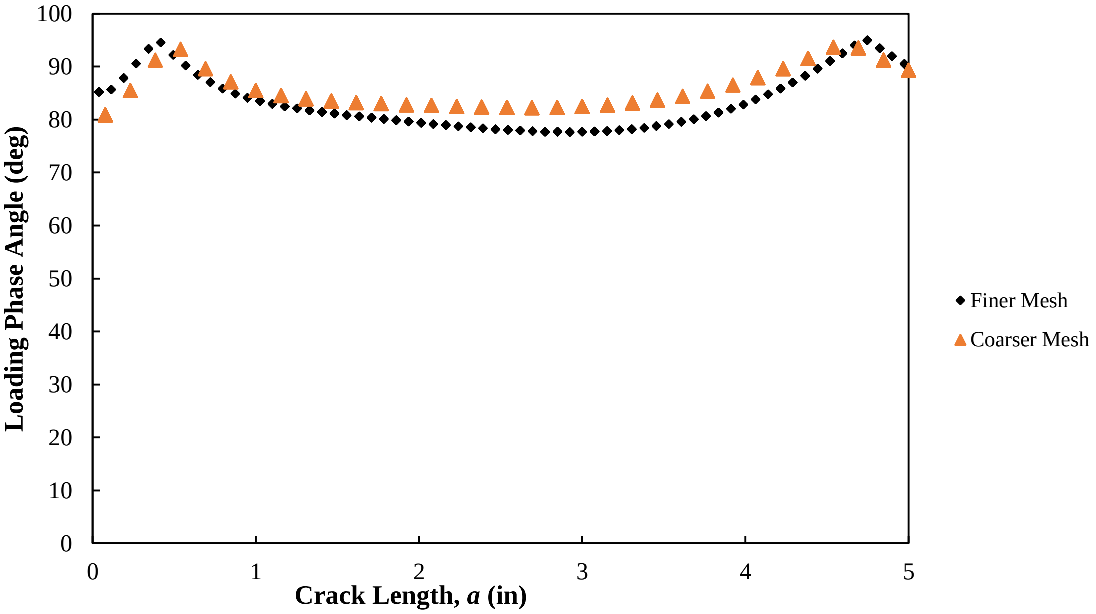

Figure 6-23 Variation of the loading phase angle, $\hat{\psi}$, with respect to crack length for the fine and coarse mesh of the unconfined triplet simulation.

6.5 Masonry Interface Toughness

As mentioned by Wang and Suo [65], defining a measurable and usable material property to parametrize fracture resistance of interfaces is the purpose of the *interfacial fracture mechanics*. This material property is called the interface *toughness* which needs to be extracted from mechanical testing raw data. Cao and Evans [66] performed experiments on glass/adhesive and aluminum/adhesive interfaces to measure the fracture resistance of their interfaces. Their experiments revealed that the critical strain energy release rate, toughness, increases with increase in phase angle, especially when the crack opening becomes small. Wang and Suo [65] developed a Brazil-nut sandwich specimen configuration with a crack on a substrate/interlayer interface to measure the interfacial fracture resistance at different loading phase angles, which can be controlled by the angle of diametral compression. Plexiglass/epoxy and metal/epoxy interfaces were examined and a rise in the interface toughness as the phase angle value increases was observed. Liechti and Chai ([67], [68]) also conducted a series of experiments focusing on the interface between epoxy and glasses. Their toughness curve had an increasing almost linear trend with respect to the phase angle for $0 < \hat{\psi} < 80^{\circ}$ with asymptotic values of toughness as $\hat{\psi} \rightarrow 90^{\circ}$. In all these bi-material interface studies, the interface toughness is a *function* of the relative amount of mode 2 to mode 1 acting on the interface, not just a single material parameter [32].

At a prescribed phase angle, $\hat{\psi}$, the maximum loading amplitude or the critical energy release rate, G, that an interface can sustain without decohesion is the toughness of that interface at $\widehat{\psi}$ which is expressed as [65]

$$G = \Gamma(\widehat{\psi}), \tag{6-1}$$

where G is the energy release rate as a force driving the interfacial crack propagation, and Γ is the interface toughness as a material resistance to the interfacial crack growth.

According to the Griffith energy balance, the equilibrium conditions of a solid of unit thickness with no net change in total energy for an incremental increase in the crack length ∂a may be expressed as [61]

$$\frac{\partial E_T}{\partial a} = \frac{\partial \Pi}{\partial a} + \frac{\partial \mathrm{W}_s}{\partial a} = 0 \tag{6-2}$$

or

$$-\frac{\partial \Pi}{\partial a} = \frac{\partial \mathrm{W}_s}{\partial a}, \tag{6-3}$$

where E_T is the total energy, Π is the total potential energy supplied by the internal strain energy and external forces, and W_s is the work required to create new surfaces. W_s depends on the *surface energy* (energy per unit area) of the material which is a material property. According to Griffith theory, the interface toughness, Γ, is actually a surface energy of the material equivalent to the right side of Equation (6-3). When the strain energy change which is due to an increment in crack length is sufficient to overcome the surface energy of material, the fracture occurs.

In the Griffith model, it is assumed that the work of fracture comes exclusively from the surface energy of the material which is valid for ideally brittle solids. In general, not only may the material resistance include the surface energy, but also it may involve plastic work, or shielding due to the initial roughness of the interface, or other types of energy dissipation associated with a propagating crack. The plastic or viscoelastic dissipation may be neglected in the quasi-brittle failure of the brick-mortar interface at micro-level analysis. In the lattice simulations of this study, the surface energy of the brick-mortar interface was considered as the only material resistance. The strength of interface struts against mode 1 and/or mode 2 deformations may be regarded as the surface energy of the interface material at the micro level.

It is possible to extract the interface toughness curve from the three categories of lattice simulations, i.e., the pre-notched four-point bending beam, the direct tension test, and the unconfined triplet simulation mentioned in Sections 6.1 to 6.3. Figure 6-24 illustrates the toughness curve for the masonry interface obtained by the lattice model. It indicates that the interface toughness is approximately a linear function for the interface behavior of the aforementioned simulations for $7.8^\circ \leq \hat{\psi} \leq 78.8^\circ$.

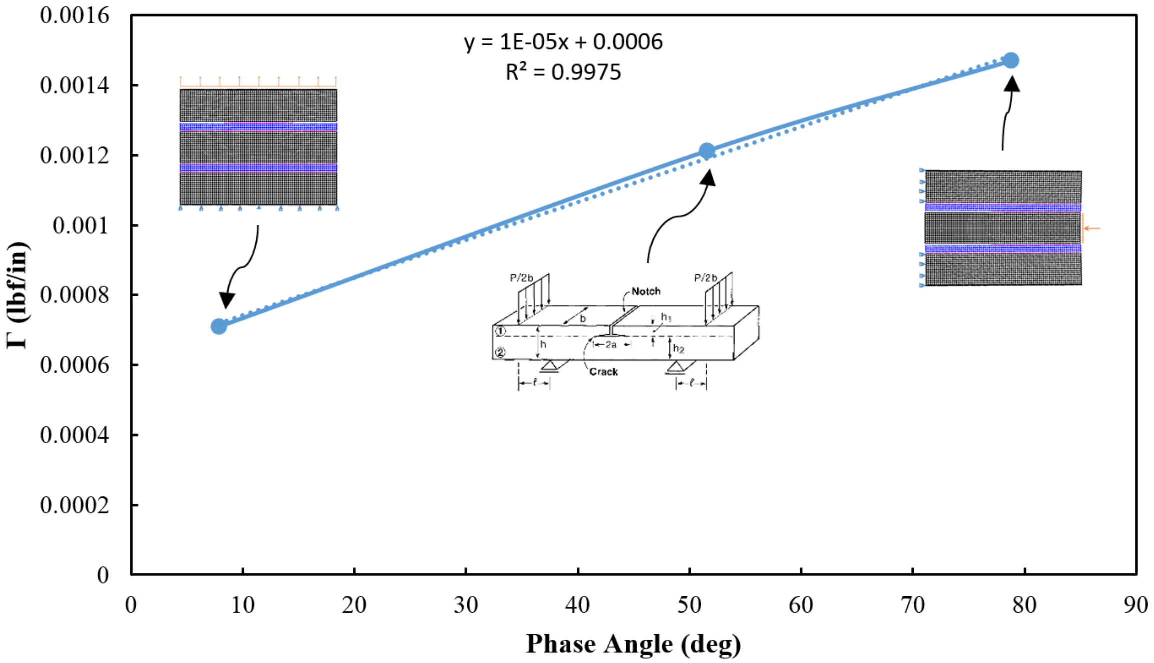

Figure 6-24 Interface toughness curve, $\Gamma(\hat{\psi})$, for a brick-mortar interface obtained from the three lattice simulations.

6.6 Fracture Energy of Cohesive Zone Models

As discussed in Section 4.1, the value of Dundur's parameter β for concrete and masonry is sufficiently small such that a zero β hypothesis can be assumed. For $\beta = 0$, the components of the energy release rate, G, can be related to the stress intensity factor for mode 1 and mode 2 as [32]

$$G_1 = \frac{{K_1}^2}{E_*}, \text{and } G_2 = \frac{{K_2}^2}{E_*}, \tag{6-4}$$

where $\mathrm{G} = G_1 + G_2$. G_1 and G_2 can be regarded as the work performed by normal and shear tractions on the interface moving through the crack surface displacements of mode 1 opening and mode 2 slip, respectively [32]. When $\beta \neq 0$, this decomposition does no longer exist. Figure 6-25 and Figure 6-26 show the variations of energy release rate for mode 1 and mode 2 for the lattice analysis of the four point bending in Figure 6-2. It can be seen that as the crack length increases, mode 2 slightly increases with crack extension, which is also evident in Figure 6-5 for the phase angle.

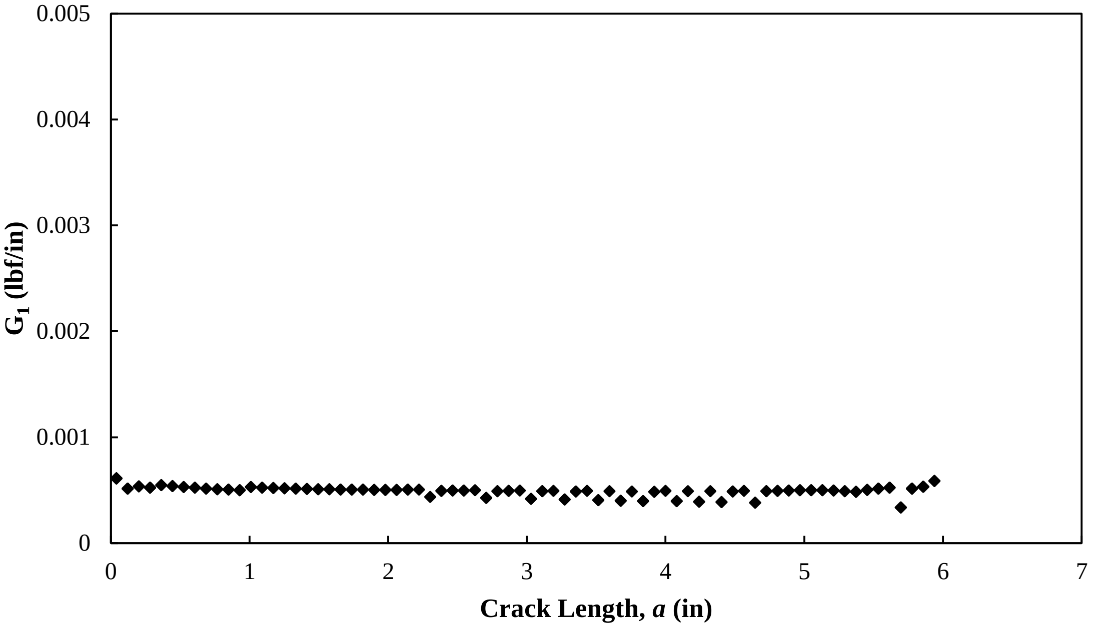

Figure 6-25 The mode 1 energy release rate for the lattice four-point bending beam.

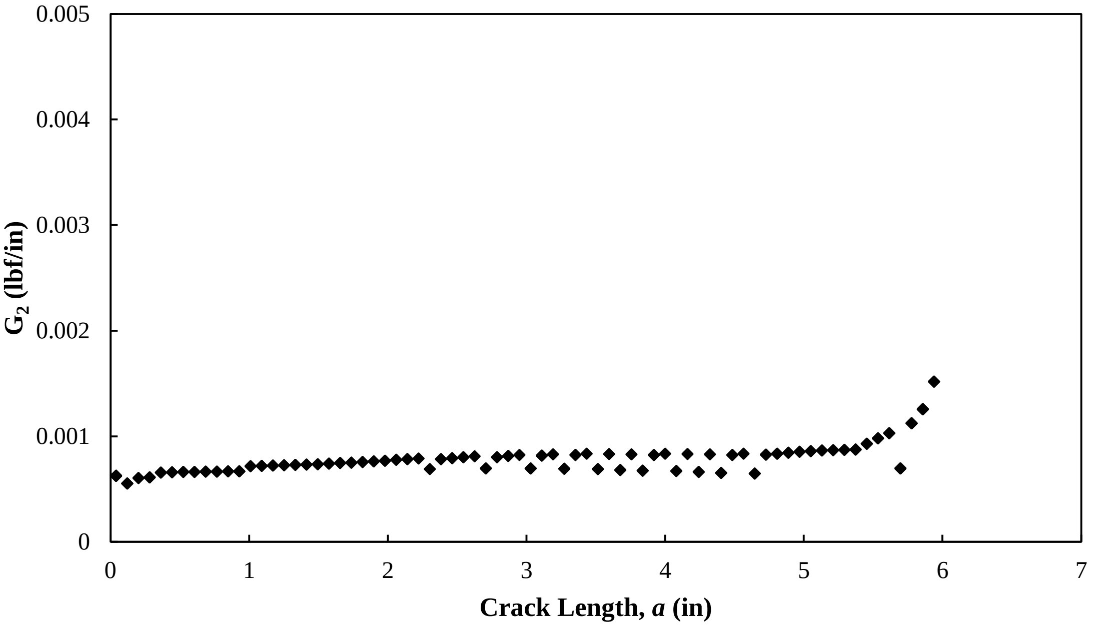

Figure 6-26 The mode 2 energy release rate for the lattice four-point bending beam.

Furthermore, Figure 6-27 to Figure 6-30 illustrate the variation of G_1 and G_2 in terms of crack length for the tension and triplet tests, respectively.

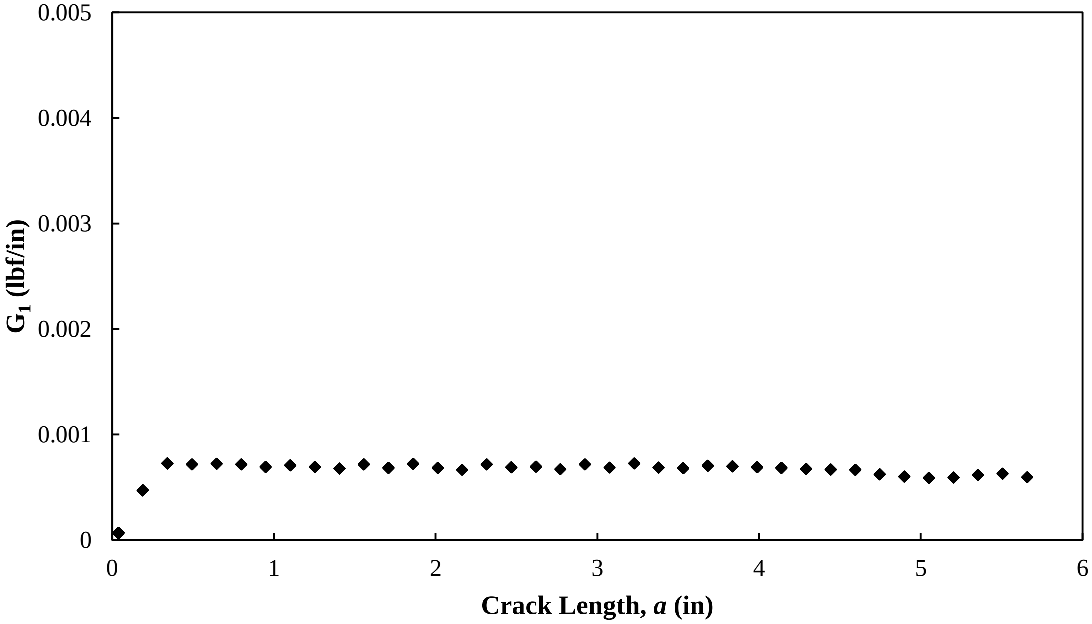

Figure 6-27 The mode 1 energy release rate for the lattice tension simulation.

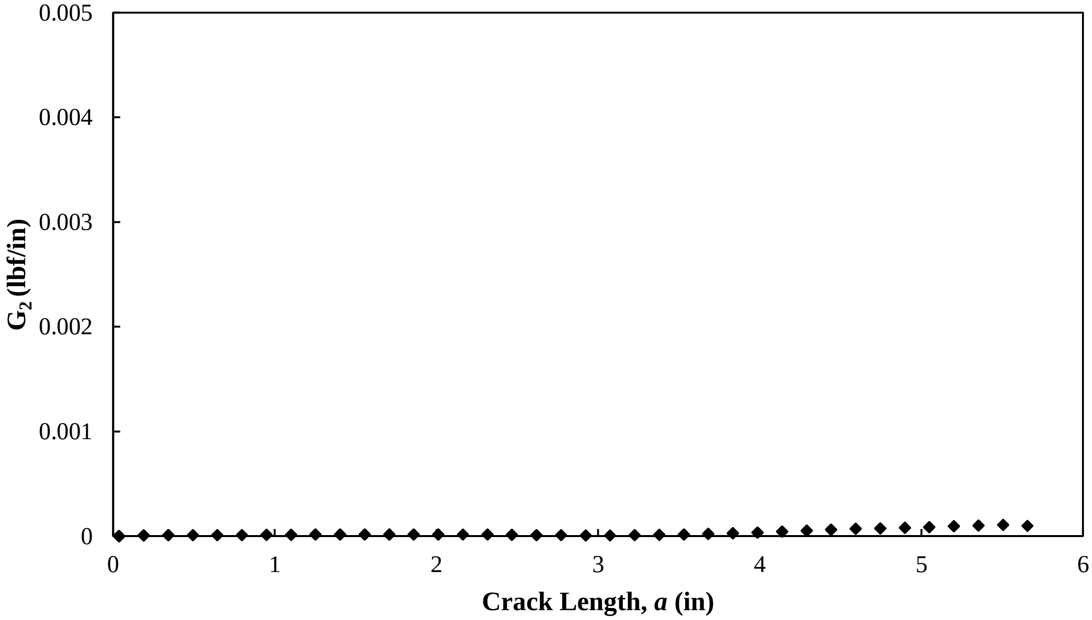

Figure 6-28 The mode 2 energy release rate for the lattice tension simulation.

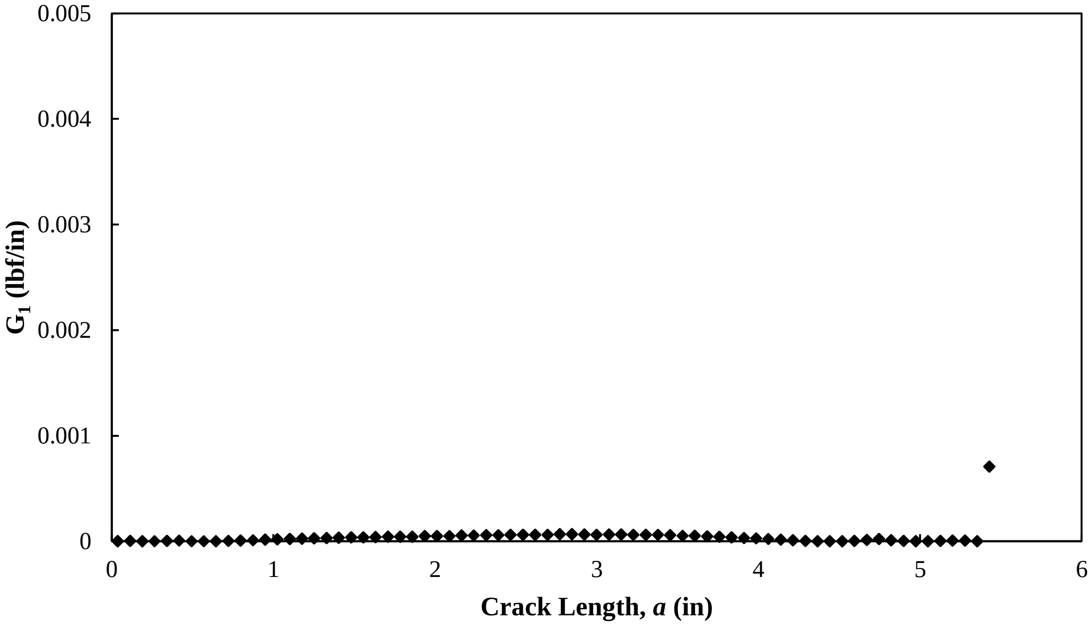

Figure 6-29 The mode 1 energy release rate for the lattice triplet simulation.

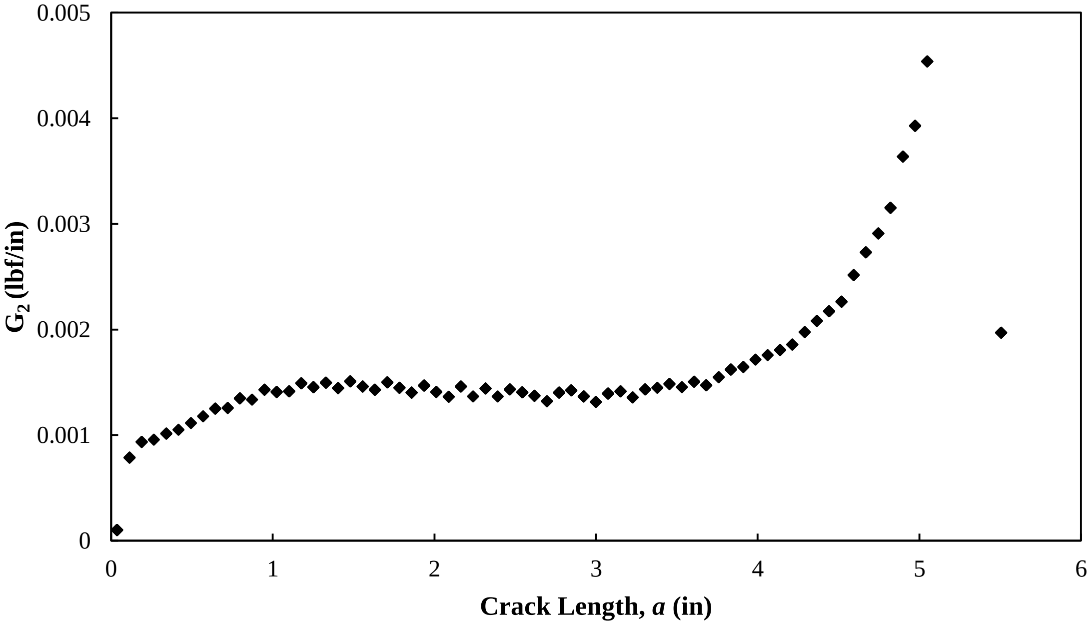

Figure 6-30 The mode 2 energy release rate for the lattice triplet simulation.

The values of G, G_1, and G_2, shown in the aforementioned figures, are the *critical* energy release rates when a crack extension happens on the lattice mesh (Figure 6-2 for instance). These critical values are equivalent to the area under the traction-separation curve of a cohesive zone interface model. The pink interface struts in Figure 6-2 fail one by one in an unzipping manner. If it is assumed that the cohesive zone, between the fully-damaged and undamaged part of the interface, always contains *one* interface strut at the micro-level, then each point in Figure 6-4, for example, which is due to the energy released by removing that single interface strut in the cohesive zone, is equivalent to the area beneath the traction-separation law after initiation of damage. Determining the parameters of a bilinear traction-separation law, which is the simplest cohesive zone model, is nontrivial and conducting an experimental program to measure them is very difficult, if not impossible. This is an interesting capability of the implemented micro-level lattice model, the simulation results of which can be used at a meso-level continuum traction-separation interface model. Constant steady-state variation of G in Figure 6-4 is a useful characteristic of the simulation in Figure 6-2 which can give a consistent result for the required fracture energy parameter of the traction-separation cohesive zone model.

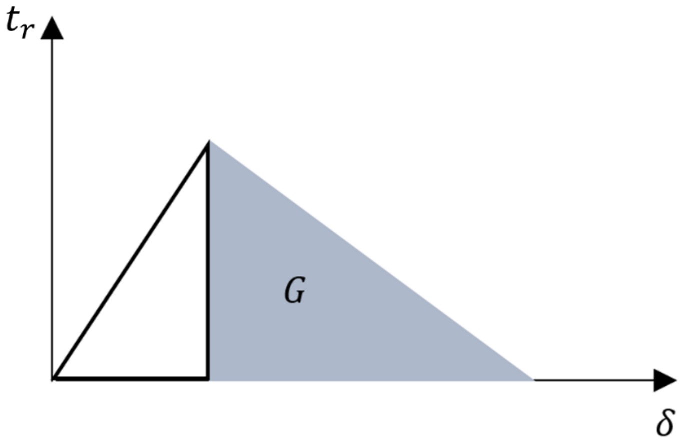

Figure 6-31 The critical energy release rate of a single interface strut used as the critical fracture energy of a continuum cohesive zone model in the traction-separation plane.

Figure 6-31 illustrates the critical energy release rate associated with the failure of a single interface strut in the lattice which can be used as the critical fracture energy for a continuum cohesive zone model. The shaded triangular area in the bilinear traction-separation law is equivalent to the G value obtained by the lattice model. The area of the left triangle, which belongs to the linear behavior of the cohesive zone, can directly be determined by the linear properties and the maximum traction value.

6.7 Homogenization of a Masonry Unit Cell: Uniaxial Tension Case

This section provides a brief explanation on how the lattice model might be employed in homogenizing a heterogeneous anisotropic masonry unit cell made of brick, mortar and their interface using energy equivalence concepts. The direct tension test was only considered here for the sake of simplicity. Other loading scenarios like shear and compression may also be included using the same approach presented in this section. The purpose is to obtain a post-peak scalar damage parameter of a homogenized isotropic finite element from the fracture energy results of a lattice masonry unit cell. Elastic properties of the homogenized finite element, i.e., equivalent Young's modulus and Poisson's ratio, can easily be obtained from the linear elastic behavior of the lattice unit cell in $\sigma_y - \varepsilon_y$ and $\sigma_y - \varepsilon_x$ planes, respectively. Figure 6-32 shows the lattice masonry unit cell under vertical direct tension.

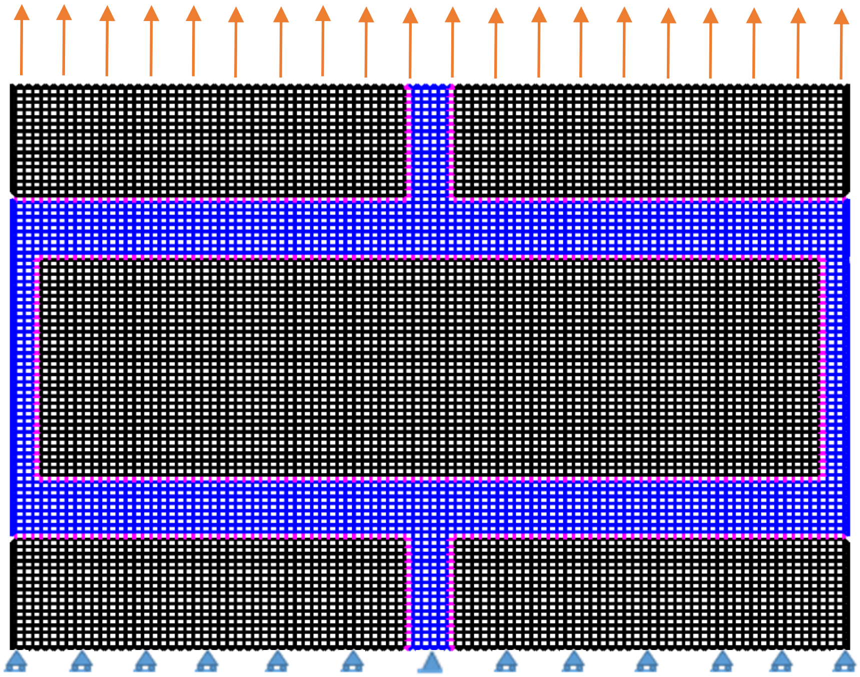

Figure 6-32 The lattice masonry unit cell in direct tension.

It is assumed that the total strain energy released in the lattice masonry unit cell, ∂U_{cell}, in direct tension as the crack propagates equals the total strain energy dissipated in the equivalent homogenized isotropic continuum finite element, ∂U_{cont}, under the same loading as

$$\partial U_{cell} = \partial U_{cont}. \tag{6-5}$$

According to Equation (5-6), the strain energy released or the change in the strain energy stored in a solid of *unit thickness* for a crack length growth of ∂a can be expressed as

$$\partial U = -\partial \Pi = G\partial a, \text{ or } \partial U_{inc} \cong \Delta U_{inc} = G_{inc} \times \Delta a_{inc}, \tag{6-6}$$

where subscript inc denotes the increment number in the lattice simulation, ΔU_{inc} is the strain energy dissipated for a crack length growth of Δa_{inc}, and G_{inc} is the energy release rate obtained from the lattice. For solids of thickness t, the value of ΔU_{inc} in (6-6) must be multiplied by t. It should be noted that for increments where there is no increase in the crack length, i.e., $\Delta a_{inc} = 0$, there is then no strain energy dissipation and $\Delta U_{inc} = 0$.

Since these dissipated energy values correspond to the crack propagation and the damage incurred in the masonry unit cell, a scalar damage parameter can be defined based on the dissipated strain energy and energy release rate values during the analysis. Let D_{INC} and ΔU_{total} be the scalar damage parameter at increment INC and the total dissipated strain energy for the all increments, respectively. D_{INC} may be expressed as

$$D_{INC} = \frac{\sum_{inc=1}^{INC} \Delta U_{inc}}{\Delta U_{total}} = \frac{\sum_{inc=1}^{INC} \Delta U_{inc}}{\sum_{inc=1}^{INC\_ult} \Delta U_{inc}}; 0 \leq D_{INC} \leq 1, \tag{6-7}$$

where INC_ult is the ultimate increment number when the analysis is terminated. The numerator of (6-7) is the accumulated strain energy released up to the increment INC.

Since the mesh and its boundary conditions in Figure 6-32 are all symmetric, it is possible to analyze one half of the mesh to reduce computational cost. Figure 6-33 illustrates the lattice mesh and boundary conditions of a one half symmetric masonry unit cell under direct tension. The mesh belongs to the last increment of the analysis when $D_{INC} = 1$. It is seen in Figure 6-33 that the failure mostly occurred through the interface struts with penetrations into the mortar joints in the last increments. Figure 6-34 and Figure 6-35 depict the load-displacement curve and the variation of G against crack length for this simulation. Data obtained from Figure 6-35 can be used to determine the scalar damage parameter, D_{INC}.

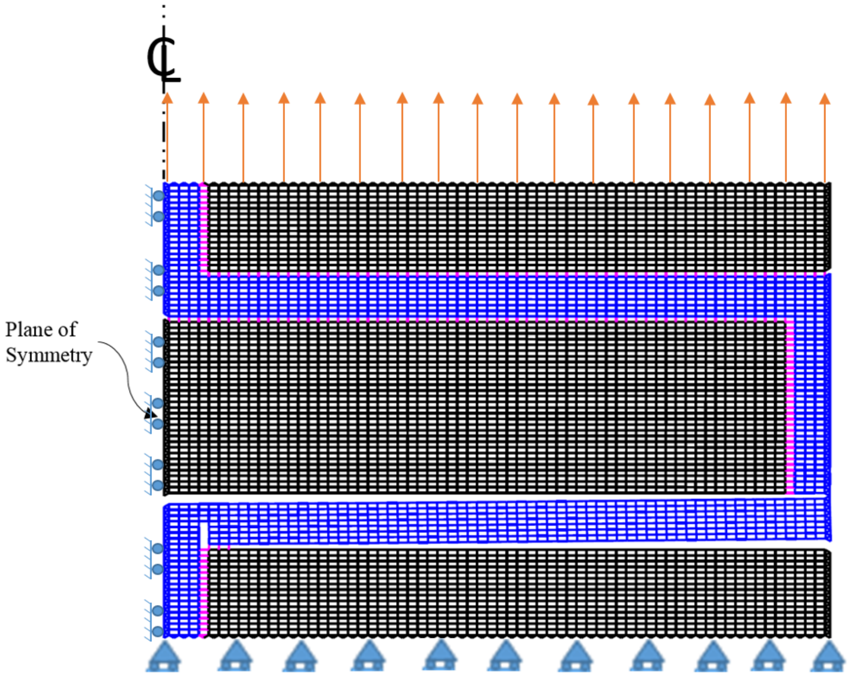

Figure 6-33 One half of the symmetric masonry unit cell mesh and its boundary conditions under direct tension at the last increment.

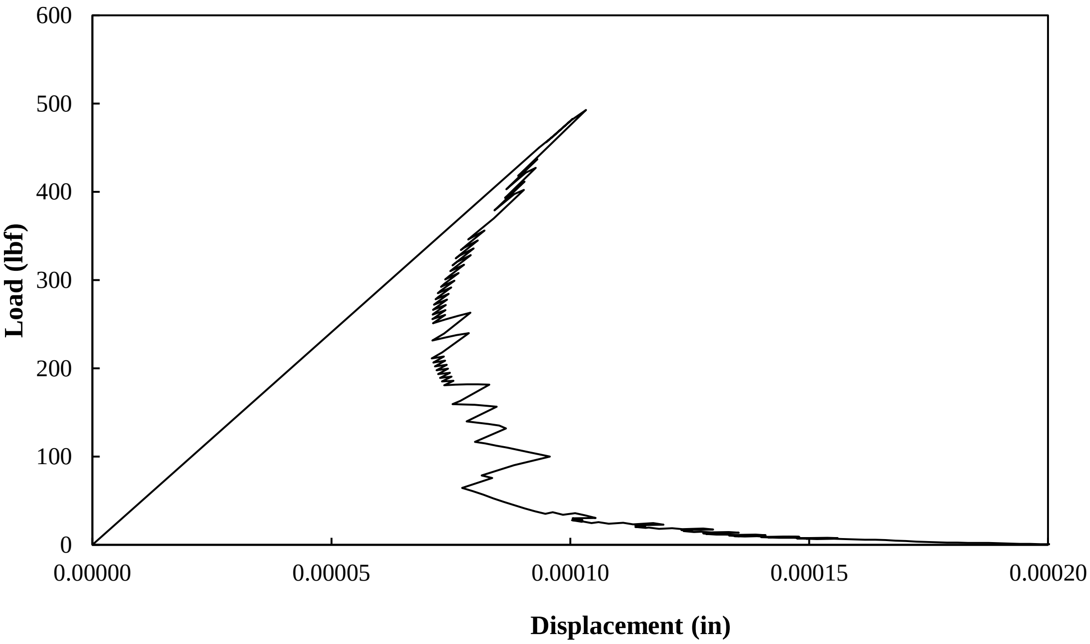

Figure 6-34 Load-displacement curve of the masonry unit cell in Figure 6-33.

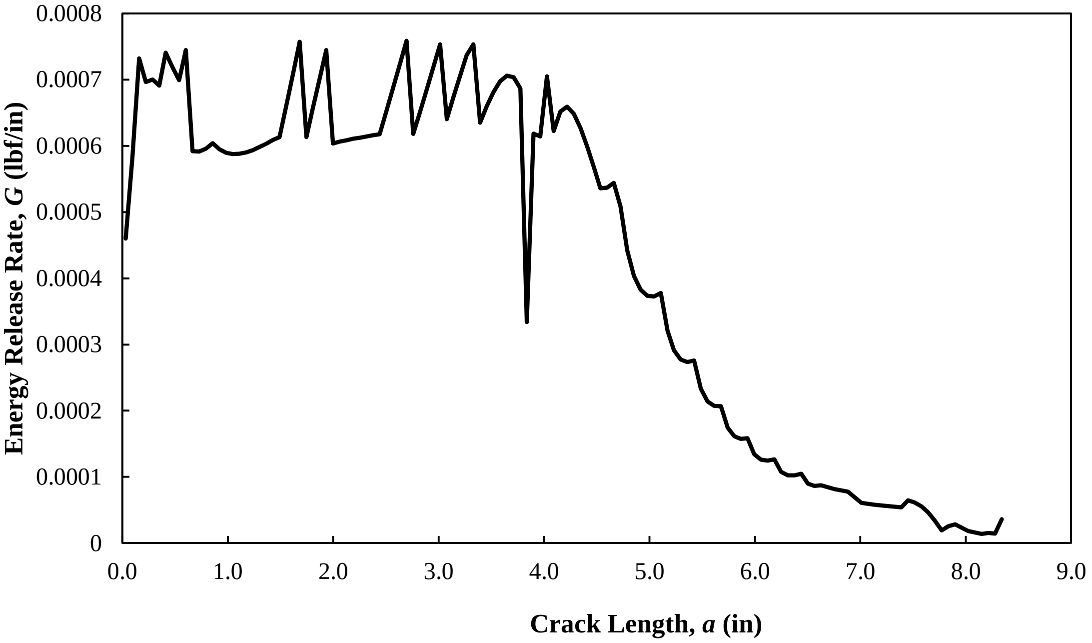

Figure 6-35 Variation of the energy release rate with respect to crack length for the masonry unit cell in Figure 6-33.

Using the fracture energy release rate values from Figure 6-35 and Equation (6-7), one can determine the scalar damage parameter, D_{INC}, of the unit cell in Figure 6-33. Figure 6-36 illustrates the variation of D_{INC} against the crack length propagation. D_{INC} firstly increases in a constant rate followed by a decreasing rate of change. The major linear part of the curve in Figure 6-36 corresponds to the unzipping failure of the lower interface struts in Figure 6-33. In other words, the masonry unit cell experiences more degradation and damage due to the complete failure of the lower interface where $D_{INC} = 0.703$ and the load level drops to about $100\ (lbf)$. Furthermore, Figure 6-37 shows the change of D_{INC} with respect to the average displacement of the top nodes in Figure 6-33 where the tension traction is applied. Considering the assumption in (6-5), it is possible to use the damage data in Figure 6-37 to model the nonlinear behavior of the homogenized isotropic continuum finite element, equivalent to the anisotropic masonry unit cell in Figure 6-32, under direct tension based on damage formulations.

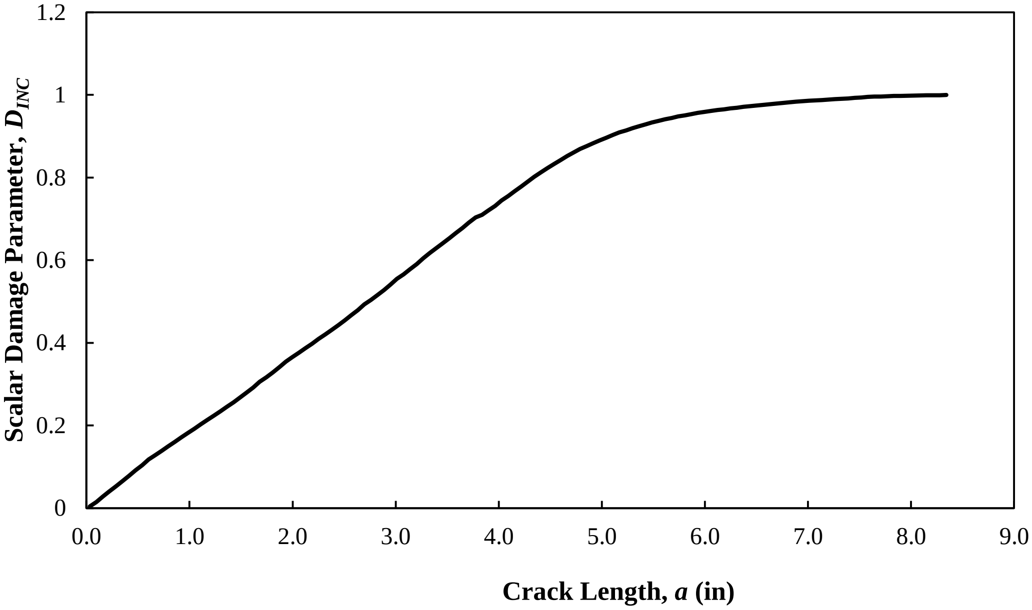

Figure 6-36 Variation of the scalar isotropic damage parameter with respect to crack length.

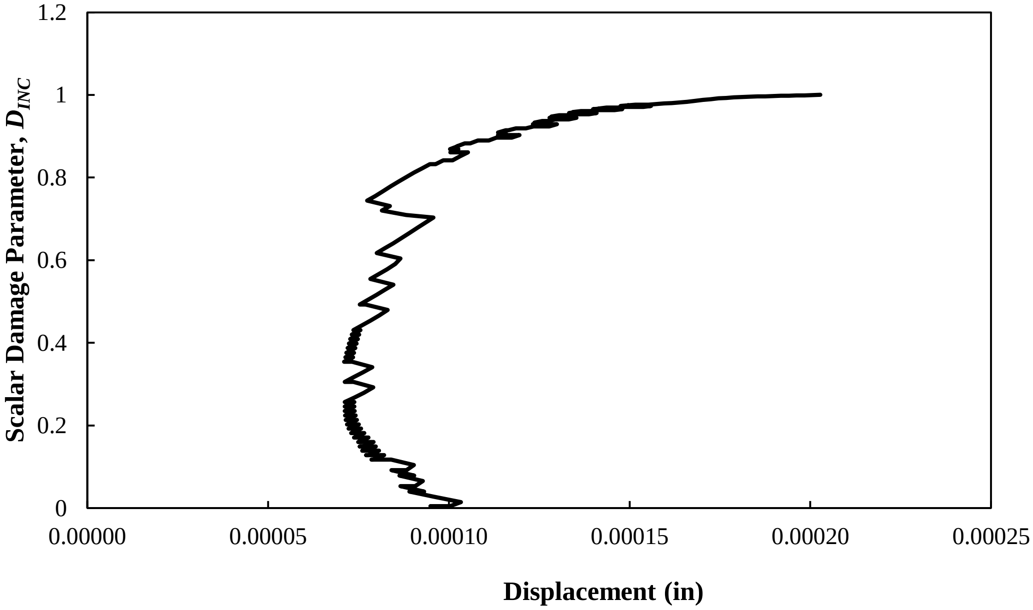

Figure 6-37 Variation of the scalar isotropic damage parameter with respect to the average displacement of the top nodes in Figure 6-33 where the tension traction is applied.

6.8 Summary

After validating the capability of the lattice in calculating the fracture energy release rate and stress intensity factors of some classic fracture problems in Chapter 5, some well-known test configurations in masonry context were simulated as explained in Sections 6.1 to 6.3. In all these simulations, a fairly uniform constant variation of energy release rate for an interval of crack length was observed, which could help determine a single value for the critical fracture energy dissipation on cohesive zone models. It was also seen that the value of loading phase angle, $\hat{\psi}$, is insensitive to the distance r from the crack tip which is a promising feature of the lattice indicating that decomposing the modulus of stress intensity factor, $|K|$ into mode 1 and 2 stress intensity factors, K_1 and K_2, is not sensitive to r or the mesh size. Moreover, the values of $\hat{\psi}$ with respect to the crack length for these simulations signify that the fracture failure of the interface in the four-point bending simulation is a mixed mode while it is predominantly mode 1 and mode 2 for the tension and triplet simulations, respectively.

In order to investigate the effect of mesh refinement on the fracture properties of the interface crack tip, two different meshes were analyzed for each of the three test configurations explained in Sections 6.1 to 6.3. The values of the energy release rate and loading phase angle were examined for these two different meshes. It was observed that the values of energy release rate and phase angle for the three simulations are fairly insensitive to the mesh size. This is more pronounced for the tension and triplet simulations which are specific test configurations for the masonry interface studies. Looking at the variations of G for the tension and triplet configurations, i.e., Figure 6-20 and Figure 6-22, one could conclude that the lattice results for predicting the fracture energy dissipated during the failure of interface struts are utterly mesh independent.

The implemented lattice can also predict the interfacial toughness of any bi-material interface which is actually the critical energy release rate values obtained from the change in the lattice stiffness matrix as expressed in Equation (5-6). In the lattice simulations of this study, the surface energy of the brick-mortar interface was considered as the only material resistance and other types of energy dissipation due to a crack growth like plastic work or shielding were neglected for the quasi-brittle failure of the brick-mortar interface. The interface toughness curve from the three types of lattice simulations was obtained from the basic strength material properties of the interface frame elements. The interface toughness is approximately a linear function for the interface behavior in direct tension, in four-point bending, and in double lap shear conditions for $7.8^{\circ} \leq \hat{\psi} \leq 78.8^{\circ}$.

In addition, the uniform variation of the energy release rate parameter makes it feasible to extract the critical dissipated energy values for the cohesive zone models. These critical values are equivalent to the area under the traction-separation curve of a cohesive zone interface model after damage initiation. If it is assumed that the cohesive zone, between the fully-damaged and undamaged part of the interface, always contains *one* interface strut, then each point in $G - a$ graph, which is due to the energy released by removing that single interface strut in the cohesive zone, is equivalent to the area beneath the traction-separation law after initiation of damage. This is an interesting capability of the implemented micro-level lattice model, the simulation results of which can be utilized at a meso-level continuum traction-separation interface model.

Furthermore, the fracture energy outputs of the lattice may be employed in homogenizing a heterogeneous anisotropic masonry unit cell made of brick, mortar and their interface using energy equivalence concepts. For simplicity, the direct tensile loading scenario was only regarded for this purpose. The post-peak scalar damage parameter of a homogenized isotropic finite element was determined from the fracture energy release rate values of a lattice masonry unit cell under tension. The scalar damage parameter at each increment was calculated from the accumulated dissipated strain energy values up to that increment divided by the total strain energy dissipated throughout the analysis. These damage data in terms of displacements could be used to model the nonlinear behavior of a homogenized isotropic continuum finite element which is equivalent to the anisotropic masonry unit cell under direct tension based on damage formulations.

Chapter 7 CONCLUDING REMARKS

In this thesis, an existing 2D lattice model was developed and implemented based on a strut-removal strategy to simulate the progressive crack evolution in a homogeneous or heterogeneous solid. This crack propagation capability was used to determine the interfacial fracture properties of any bi-material system, especially the brick-mortar, from the basic strength properties of interface struts. Some material level laboratory tests along with some numerical sensitivity analyses were conducted to determine those material properties needed for the lattice simulations.

The Voronoi diagram was used to discretize a continuum domain into polygons, or particles. Plane frame elements with three degrees of freedom at each node were chosen because of their capability to better capture the crack pattern in continuum domains than truss elements, and also due to their added computational stability. The strength properties of brick, mortar, and interface were then projected on top of the lattice struts based on their coordinates on the domain to simulate a three-phase boundary value problem. The simulation of fracture was performed with a 'linear elastic' analysis of the lattice under loading and removing one element at a time from the mesh which exceeds a certain failure criterion in tension, compression, and shear. Failure of brick and mortar were expressed in terms of a tension cut-off and compression-cap. Shear failure criteria were neglected for brick and mortar elements since the main focus of this study was to evaluate the brick-mortar interface fracture properties, and with the simulations conducted, their shear failure envelopes were not activated. The failure criterion for the brick-mortar interface was also determined based on a combination of experimental measurements and numerical parametric calculations. This failure function has a compressive cap which lets diagonal interface struts in a regular triangular lattice fail for triplet tests under high normal confinements.

Interfacial fracture mechanics is an important topic of research in applied mechanics over the past few decades since the interface of two materials in contact is the weakest part of composites like masonry along which failure usually occurs. Different elastic properties of abutting dissimilar materials introduce mismatches in the in-plane tensile modulus and bulk modulus across the interface, quantified by the α-, and β-parameters, respectively. The influence of Muskhelishvili's work in solving any problem in the plane theory of elasticity by finding two complex functions which satisfy boundary conditions of that problem was elaborated. In bi-material systems, the same Muskhelishvili's equations, which were developed for displacement and stress fields of a two dimensional homogeneous isotropic solid, were also employed in solving bi-material interface cracks. The effect of a nonzero β in solving interfacial crack problems was also discussed.

Furthermore, the concepts of interfacial fracture mechanics along with the implementation of the lattice model were used to determine the fracture properties of the brick-mortar interface. The implemented 2D lattice model simulates crack path evolution in the form of strong discontinuities at a homogeneous or heterogeneous solid. Unlike the pre-cracked approach of the virtual crack extension procedure or the complicated XFEM, the lattice's relative simple theory and implementation makes it a promising tool in solving crack problems in fracture mechanics. Three classic fracture mechanics problems were addressed to validate the lattice fracture results. The center cracked problem in a homogeneous domain, the single edge notch problem in a homogeneous solid, and the center interface cracked problem in a bi-material system were solved by the numerical lattice. The energy method was employed to obtain the energy release rate of the lattice mesh as the crack evolves. In this method, the energy released or dissipated during the crack growth is mainly determined by considering the change in the global stiffness matrix of the mesh with respect to crack length change. Comparison of the analytical results of the three benchmark problems with the numerical solutions of the lattice for those problems validates the capability of the lattice in predicting the energy release rate and stress intensity factor of crack problems in homogeneous and heterogeneous solids. In all three cases, the lattice gives better results once the dimensions of the mesh are large enough to assure that the stresses are remotely applied.

After validating the capability of the lattice in calculating the fracture energy release rate and stress intensity factors of some classic fracture problems, some well-known test configurations in masonry context were simulated. The concept of total potential energy of the lattice model was used to determine the energy release rate of an interface strut failure while the crack develops. Three types of lattice simulations were performed to obtain the energy release rate and fracture properties of brick-mortar interface. Each of these simulations exhibit different failure mode mixity. In the pre-notched bi-material four-point bending simulation, the interface experiences a mixed mode failure with almost the same contribution of mode 1 and mode 2, as indicated by the phase angle variations. As expected, the dominant interfacial failure mode in the unconfined triplet test is mode 2, while mode 1 has the major contribution in interface failure for the direct tension simulation. The values of G, G_1, and G_2 rendered by the lattice simulations are the critical energy release rates when a crack extension happens. These critical values are equivalent to the area under the traction-separation curve of a cohesive zone interface model after the damage initiates. Determining the parameters of a bilinear traction-separation law is nontrivial and it is very difficult to conduct an experimental program to measure them. The implemented micro-level lattice model is a promising tool to determine energy release quantities that can readily be used at a meso-level continuum traction-separation interface model. Knowing that the values of G are the critical ones, it is possible to determine the interface toughness curve based on these three types of simulations. The present approach can also be used to obtain the fracture energy for a variety of interfaces of other bi-materials, relating the discretized microstructure to the continuum meso-structure.

Finally, the fracture energy outputs of the lattice was employed in homogenizing a heterogeneous anisotropic masonry unit cell made of brick, mortar and their interface using energy equivalence concepts into a homogenized isotropic continuum finite element. For simplicity, the direct tensile loading scenario was only considered for this purpose. The post-peak scalar damage parameter of a homogenized isotropic finite element was determined from the fracture energy release rate values of a lattice masonry unit cell. An scalar damage parameter at each increment was calculated from the accumulated dissipated strain energy values up to that increment divided by the total strain energy dissipated during the completion of the analysis. These damage data in terms of displacements could be used to model the nonlinear behavior of a homogenized isotropic continuum finite element which is equivalent to the anisotropic masonry unit cell under direct tension based on damage formulations. The same methodology, used for the direct tensile loading, may be extended to other load scenarios like bi-axial tension, or compression, or shear to account for different failure modes.

The heterogeneous anisotropic masonry unit cell's homogenization technique mentioned above may be regarded as a bridge between the micro-scale lattice analysis and macro-scale masonry wall. The homogenized continuum finite element with the post peak damage data obtained from the lattice approach can be employed in a homogenized macro-scale masonry wall which has an equivalent Young's modulus and Poisson's ratio with the same damage data as the heterogeneous masonry unit cell. In this study, only the direct tension loading case was simulated while other loading scenarios like compression and shear in the form of bi-axial loading may be considered for the future work. This may give an orthotropic damage data for the homogenized continuum finite element to be used in the masonry wall under different loading cases. Furthermore, the lattice model can provide the displacements and rotation of all particles' nuclei or computational points. These kinematic data may be utilized in calculating the strain and stress distributions on the Voronoi representation of a given continuum, using the gradient of the global displacement vector. Having the strain and stress distributions obtained by the lattice model, one could compare the lattice results with or without rotational degrees of freedom with those of classic or micro-polar continuum mechanics to investigate how the rotations influence the numerical results of the lattice approach.

REFERENCES

[1] J. Khatib, Sustainability of Construction Materials, 1st ed. Woodhead Publishing, 2009.

[2] K. N. P. Steele, G. Cole, and G. Parke, “The Application of Life Cycle Assessment Technique in the Investigation of Brick Arch Highway Bridges.” 2002.

[3] L. Mabon, “Assessment , Strengthening and Preservation of Masonry Structures for Continued Use in Today’s Infrastructure,” in *International Association for Bridge and Structural Engineering Conference*, 2002.

[4] R. Goodman, R. Taylor, and L. Brekke, “A Model for the Mechanics of Jointed Rock,” in *Journal of the Soil Mechanics and Foundations Divisions, Proceedings of the American Society of Civil Engineers*, pp. 637–659, 1968.

[5] A. W. Page, “Finite Element Model for Masonry,” *J. Struct. Div.*, vol. 104, no. 8, pp. 1267–1285, 1978.

[6] H. R. Lotfi and P. B. Shing, “Interface Model Applied to Fracture of Masonry Structures,” *J. Struct. Eng.*, vol. 120, no. 1, pp. 63–80, 1994.

[7] P. B. Lourenço, “Computational Strategies for Masonry Structures,” Delft University Press, 1996.

[8] P. B. Lourenço and J. G. Rots, "Multisurface Interface Model for Analysis of Masonry Structures," *J. Eng. Mech.*, vol. 123, no. 7, pp. 660–668, 1997.

[9] I. Carol, C. M. López, and O. Roa, "Micromechanical Analysis of Quasi-brittle Materials Using Fracture-based Interface Elements," *Int. J. Numer. Methods Eng.*, vol. 52, no. 12, pp. 193–215, Sep. 2001.

[10] K. J. Willam, I. Rhee, and B. Shing, "Interface Damage Model for Thermomechanical Degradation of Heterogeneous Materials," *Comput. Methods Appl. Mech. Eng.*, vol. 193, no. 30–32, pp. 3327–3350, Jul. 2004.

[11] G. Alfano and E. Sacco, "Combining Interface Damage and Friction in a Cohesive-zone Model," *Int. J. Numer. Methods Eng.*, vol. 68, no. 5, pp. 542–582, Oct. 2006.

[12] A. Caballero, K. J. Willam, and I. Carol, "Consistent Tangent Formulation for 3D Interface Modeling of Cracking/Fracture in Quasi-brittle Materials," *Comput. Methods Appl. Mech. Eng.*, vol. 197, no. 33–40, pp. 2804–2822, Jun. 2008.

[13] E. Sacco and J. Toti, "Interface Elements for the Analysis of Masonry Structures," *Int. J. Comput. Methods Eng. Sci. Mech.*, vol. 11, no. 6, pp. 354–373, Nov. 2010.

[14] W. S. McNary and D. P. Abrams, "Mechanics of Masonry in Compression," *J. Struct. Eng.*, vol. 111, no. 4, pp. 857–870, 1985.

[15] C. Citto, S. I. Wo, K. J. Willam, and M. P. Schuller, “In-Place Evaluation of Masonry Shear Behavior Using Digital Image Analysis,” *ACI Mater. J.*, vol. 108, no. 4, pp. 413–422, 2011.

[16] C. S. Desai, M. M. Zaman, J. G. Lightner, and H. J. Siriwardane, “Thin-layer Element for Interfaces and Joints,” *Int. J. Numer. Anal. Methods Geomech.*, vol. 8, no. 1, pp. 19–43, 1984.

[17] J. G. Rots, Structural Masonry: An Experimental/Numerical Basis for Practical Design Rules (CUR Report 171) (CUR-reports), 1997.

[18] G. Giambanco, S. Rizzo, and R. Spallino, “Numerical Analysis of Masonry Structures via Interface Models,” *Comput. Methods Appl. Mech. Eng.*, vol. 190, no. 49–50, pp. 6493–6511, Oct. 2001.

[19] G. Giambanco and Z. Mroz, “The Interphase Model for the Analysis of Joints in Rock Masses and Masonry Structures,” *Meccanica*, vol. 36, pp. 111–130, 2001.

[20] L. Macorini and B. A. Izzuddin, “A Non-linear Interface Element for 3D Mesoscale Analysis of Brick-masonry Structures,” *Int. J. Numer. Meth. Engng*, vol. 85, pp. 1584–1608, 2011.

[21] N. I. Muskhelishvili, Some Basic Problems on the Mathematical Theory of Elasticity. Translated by J.R.M. Radok, Noordhoof, Groningen, The Netherlands, 1953.

[22] M. L. Williams, “The Stresses around a Fault or Crack in Dissimilar Media,” *Bull. Seismol. Soc. Am.*, vol. 49, no. 2, pp. 199–204, 1959.

[23] J. R. Rice and G. C. Sih, “Plane Problems of Cracks in Dissimilar Media,” *J. Appl. Mech.*, vol. 32, pp. 418–423, 1965.

[24] A. H. England, “A Crack between Dissimilar Media,” *J. Appl. Mech.*, vol. 32, pp. 400-402, June 1965.

[25] F. Erdogan, “Stress Distribution in Bonded Dissimilar Materials with Cracks,” *J. Appl. Mech.*, vol. 32, pp. 403-410, June 1965.

[26] J. R. Rice, “Elastic Fracture Mechanics Concepts for Interfacial Cracks,” *J. Appl. Mech.*, vol. 55, pp. 98-103, March 1988.

[27] D. M. Parks, “A Stiffness Derivative Finite Element Technique for Determination of Crack Tip Stress Intensity Factors,” *Int. J. Fract.*, vol. 10, no. 4, pp. 487–502, 1974.

[28] P. G. Charalambides, J. Lund, A. G. Evans, and R. M. McMeeking, “A Test Specimen for Determining the Fracture Resistance of Bimaterial Interfaces,” *J. Appl. Mech.*, vol. 56, pp. 77–82, March 1989.

[29] P. P. L. Matos, R. M. McMeeking, P. G. Charalambides, and M. D. Drory, “A Method for Calculating Stress Intensities in Bimaterial Fracture,” *Int. J. Fract.*, vol. 40, no. 2, pp. 235–254, 1989.

[30] D. M. Parks, “The Virtual Crack Extension Method for Nonlinear Material Behavior,” *Comput. Methods Appl. Mech. Eng.*, vol. 12, pp. 353–364, 1977.

[31] A. G. Evans, M. Rühle, B. J. Dalgleish, and P. G. Charalambides, “The Fracture Energy of Bimaterial Interfaces,” *Metall. Trans. A*, vol. 21, pp. 2419–2429, Sep. 1990.

[32] J. W. Hutchinson and Z. Suo, “Mixed Mode Cracking in Layered Materials,” *Adv. Appl. Mech.*, vol. 29, pp. 63-191, 1992.

[33] ARAMIS System, “ARAMIS User Manual-Software.” GOM GmbH, Braunschweig, Germany, 2011.

[34] ASTM, “Standard Test Method for Splitting Tensile Strength of Masonry Units. ASTM C 1006-84.” American Society for Testing and Materials, Philadelphia, PA, 2001.

[35] A. H. Mohammadipour, K. J. Willam, and A. Ayoub, “Experimental Studies of Brick and Mortar Composites Using Digital Image Analysis,” in *Proceedings of the 8th International Conference on Fracture Mechanics of Concrete and Concrete Structures, FraMCoS*, 2013, pp. 183–192.

[36] G. Sarangapani, B. V Reddy, and K. S. Jagadish, “Brick-Mortar Bond and Masonry Compressive Strength,” *J. Mater. Civ. Eng.*, vol. 17, no. 2, pp. 229–237, 2005.

[37] J. R. Riddington, A. H. Gambo, and G. J. Edgell, “An Assessment of the Influence of Unit Aspect Ratio on Bond Shear Strength Values Given by the Proposed CEN Triplet Test,” in *9th Int. Brick/Block Masonry Conference*, 1991, pp. 1321–1328.

[38] ASTM, “Standard Test Method for Compressive Strength of Masonry Prisms. ASTM C 1314 – 03b.” American Society for Testing and Materials, Philadelphia, PA, 2003.

[39] MATLAB, “MATLAB R20014a, Version 8.3.0.532.” The MathWorks, Inc., Natick, Massachusetts, United States, 2014.

[40] A. Hrennikoff, “Solution of Problems of Elasticity by the Framework Method,” *J. Appl. Mech.*, vol. 12, pp. 169–175, 1941.

[41] J. E. Bolander Jr and S. Saito, “Fracture Analyses Using Spring Networks with Random Geometry,” *Eng. Fract. Mech.*, vol. 61, pp. 569–591, 1998.

[42] A. Okabe, B. Boots, K. Sugihara, S. N. Chiu, and D. G. Kendall, Spatial Tessellations: Concepts and Applications of Voronoi Diagrams, 2nd ed. John Wiley & Sons, LTD, 2000.

[43] C. Moukarzel and H. J. Herrmann, “A Vectorizable Random Lattice,” *J. Stat. Phys.*, vol. 68, no. 5/6, pp. 911–923, 1992.

[44] J. van Mier, Concrete Fracture, A Multiscale Approach. CRC Press, 2013.

[45] E. Schlangen and E. J. Garboczi, “New Method for Simulating Fracture Using an Elastically Uniform Random Geometry Lattice,” *Int. J. Eng. Sci.*, vol. 34, no. 10, pp. 1131–1144, 1996.

[46] R. de Borst and H. B. Muehlhaus, “Continuum Models for Discontinuous Media,” in *Fracture Processes in Concrete, Rock and Ceramics. Proceedings of the International RILEM/ESIS Conference.*, 1991, pp. 601–618.

[47] P. A. Cundall and O. D. L. Strack, “A Discrete Numerical Model for Granular Assemblies,” *Géotechnique*, vol. 29, no. 1, pp. 47–65, 1979.

[48] E. Schlangen and J. van Mier, “Experimental and Numerical Analysis of Micromechanisms of Fracture of Cement-based Composites,” *Cem. Concr. Compos.*, vol. 14, no. 2, pp. 105–118, Jan. 1992.

[49] J. Dundurs, “Elastic Interaction of Dislocations with Inhomogeneities,” *Math. Theory Dislocations*, pp. 70–115, June 1969.

[50] O. Büyüköztürk and K. M. Lee, “Assessment of Interfacial Fracture Toughness in Concrete Composites,” *Cem. Concr. Compos.*, vol. 15, pp. 143–151, 1993.

[51] Z. Suo and J. W. Hutchinson, “Sandwich Test Specimens for Measuring Interface Crack Toughness,” *Materials Science and Engineering*, vol. A107. pp. 135–143, 1989.

[52] A. H. England, Complex Variable Methods in Elasticity. Mineola, New York: Dover Publications, Inc., 1971.

[53] D. R. J. Owen and A. J. Fawkes, Engineering Fracture Mechanics: Numerical Methods and Applications. Swansea, U.K.: Pineridge Press Ltd., 1983.

[54] F. Erdogan, "Stress Distribution in a Nonhomogeneous Elastic Plane With Cracks," *J. Appl. Mech.*, vol. 30, pp. 232-236, June 1963.

[55] G. C. Sih and J. R. Rice, "The Bending of Plates of Dissimilar Materials with Cracks," *J. Appl. Mech.*, vol. 31, pp. 477-482, Sep. 1964.

[56] G. R. Irwin, "Analysis of Stresses and Strains Near the End of a Crack Traversing a Plate," *J. Appl. Mech.*, vol. 24, pp. 361–364, 1957.

[57] T. Belytschko and T. Black, "Elastic Crack Growth in Finite Elements with Minimal Remeshing," *Int. J. Numer. Meth. Engng.*, vol. 45, pp. 601–620, 1999.

[58] N. Moes, J. Dolbow, and T. Belytschko, "A Finite Element Method for Crack Growth without Remeshing," *Int. J Numer Meth Eng*, vol. 46, pp. 131–150, 1999.

[59] C. Daux, N. Moes, J. Dolbow, N. Sukumar, and T. Belytschko, "Arbitrary Branched and Intersecting Cracks with the Extended Finite Element Method," *Int J Numer Meth Eng*, vol. 48, pp. 1741–1760, 2000.

[60] O. C. Zienkiewicz, R. Taylor, and J. Zhu, The Finite Element Method: Its Basis and Fundamentals, 6th ed. Elsevier Butterworth-Heinemann, 2005.

[61] T. Anderson, Fracture Mechanics: Fundamentals and Applications, 3rd ed. Taylor & Francis, 2005.

[62] H. Tada, P. C. Paris, and G. R. Irwin, The Stress Analysis of Cracks Handbook, 3rd ed. New York: ASME Press, 2000.

[63] W. T. Koiter, Note on the Stress Intensity Factor for Sheet Strips with Cracks under Tensile Loads, Delft, The Netherlands, 1965.

[64] J. W. Hutchinson, M. E. Mear, and J. R. Rice, “Crack Paralleling an Interface between Dissimilar Materials,” *J. Appl. Mech.*, vol. 54, pp. 828–832, Dec. 1987.

[65] J. S. Wang and Z. Suo, “Experimental Determination of Interfacial Toughness Curves Using Brazil-nut-sandwiches,” *Acta Metall. Mater.*, vol. 38, no. 7, pp. 1279–1290, 1990.

[66] H. C. Cao and A. G. Evans, “An Experimental Study of the Fracture Resistance of Bimaterial Interfaces,” *Mech. Mater.*, vol. 7, pp. 295–304, 1989.

[67] K. M. Liechti and Y. S. Chai, “Asymmetric Shielding in Interfacial Fracture under In-Plane Shear,” *J. Appl. Mech.*, vol. 59, pp. 295-304, June 1992.

[68] K. M. Liechti and Y. S. Chai, “Biaxial Loading Experiments for Determining Interfacial Fracture Toughness,” *J. Appl. Mech.*, vol. 58, pp. 680-687, Sep. 1991.